TECHNISCHE UNIVERSITÄT MÜNCHEN
Lehrstuhl für Baumechanik

Model Reduction Methods in Room Acoustical Simulation at Low Frequencies

Jovana Sremčević Witzig

Vollständiger Abdruck der von der Fakultät für Bauingenieur- und Vermessungswesen der Technischen Universität München zur Erlangung des akademischen Grades eines

Doktor-Ingenieurs

genehmigten Dissertation.

Vorsitzender: Univ.-Prof. Dr.-Ing. habil. F. Duddeck

Prüfer der Dissertation:

1. Univ.-Prof. Dr.-Ing. habil. G. H. Müller
2. Univ.-Prof. Dr. rer. nat. habil. P. Rentrop
3. Associate Prof. I. Kovačić, Ph.D.
   University of Novi Sad/ Serbien

Die Dissertation wurde am 18.10.2011 bei der Technischen Universität München eingereicht und durch die Fakultät für Bauingenieur- und Vermessungswesen am 27.01.2012 angenommen.

Kurzfassung

In dieser Arbeit wird zur Reduktion des Rechenaufwands für raumakustische Simulationen im niedrigen Frequenzbereich ein Modellreduktionsverfahren verwendet. Die Methode basiert auf der sogenannten Component Mode Synthesis. Das akustische System wird in Substrukturen aufgeteilt, auf deren Ebene Analysen durchgeführt werden. In diesem angenäherten Modell des Gesamtsystems werden die Substrukturen durch Component-Modes repräsentiert. Die Anzahl zusammengesetzter Moden, die für das Approximieren des akustischen Systems notwendig ist, wird durch die Einführung von "Modal Constraint Modes" oder "Modal Attachment Modes" reduziert. Diese beschreiben das Verschiebungsmuster an der Schnittstelle zwischen den Substrukturen. Die Anwendung der Methode wird, sowohl am Beispiel des akustischen Fluids für die Kopplung von zwei und mehr Substrukturen, als auch für Fluid-Struktur-Probleme, in zwei- und dreidimensionalen Simulationen gezeigt.

Abstract

In this thesis the calculation effort in room acoustical simulations at Low Frequencies is reduced with the help of a model reduction method. The applied model reduction is based on the method of component mode synthesis. The acoustical system is divided into substructures and analyses are performed on the substructure level. In the approximated model of the whole system the substructures are represented with component modes. The necessary number of component modes for the approximation of the acoustic system is reduced by introducing *Modal* constraint modes or *Modal* attachment modes. The modal constraint and attachment modes describe the displacement pattern at the interface between the substructures. This method is applied for coupling of two and more fluid substructures and for Fluid-Structure Interaction problems in 2- and 3-dimensions.

Acknowledgments

This thesis I wrote during the last three and a half years that I have spent at the Lehrstuhl für Baumechanik of the Technische Universität München as a scholarship holder of the International Graduate School of Science and Engineering (IGSSE).

First of all, I would like to thank to Prof. Gerhard Müller for his scientific support and encouragement. Our fruitful discussions combined with his warm way of facing problems have been a big reinforcement of my motivation.

Furthermore, I thank to Prof. Peter Rentrop for the very interesting conversations during our IGSSE team meetings. Also I appreciate that Prof. Ivana Kovacic is willing to be the third supervisor of my thesis and to travel to Germany for my examination.

Special thanks go to my IGSSE team members Martin Buchschmid and Martina Pospiech. Together we have experienced all the different phases of research work filled with excitements, disappointments, exchanging ideas, facing unforeseen problems and always motivating each other when needed. Their support was very important for me.

In addition I would like to thank all my colleagues from the Lehrstuhl für Baumechanik for the comfortable and friendly work atmosphere as well as for their cooperation.

I also thank the company Müller-BBM and especially Mr. Elmar Schröder for the chance of applying my theoretical knowledge about room acoustics in practice during my three months lasting internship.

I would like to thank IGSSE which gave my much more than just financial support. The numerous seminars, language courses and social events further completed my education and also helped me to feel comfortable in a foreign country.

The biggest gratitude goes to my family, especially to my parents, who have always believed in me, encouraged me and supported my decisions.

At the end I would like to thank my husband Rainer who has always been by my side and helped me to deal with stressful situations by bringing a smile on my face.

Munich, October 2011 Jovana Sremčević Witzig

Contents

List of Abbreviations

BEM	Boundary Element Method
CMS	Component Mode Synthesis
DOF	Degrees of Freedom
FEM	Finite Element Method
FFT	Fast Fourier Transformation
FSI	Fluid-Structure Interaction
FT	Fourier Transformation
IFT	Inverse Fourier Transformation
IRF	Impulse Response Function
ITM	Integral Transform Method
LTI	Linear Time-Invariant
MCM Approach	Model Constraint Modes Approach
MLS	Maximum Length Sequence
SEA	Statistical Energy Analysis
SFEM	Spectral Finite Element Method
TF	Transfer Function
TPM	Theory of Porous Media

List of Symbols

Subscripts and Superscripts

0	reference value
a	attachment modes
b	boundary DOFs
c	constraint modes
CB	related to the Craig-Bampton method
e	related to an element in numerical methods
f	fluid
i	internal DOFs
MT	related to the modal truncation
n	normal modes
r	rigid-body DOFs
s	structure
sf	coupling elements for FSI problems
x, y, z	related to the Cartesian coordinates
$\mathbf{K}_{ib}^{s}$	matrix of dimensions $i \times b$ describing component s

Symbols

Latin Letters

a	acceleration
$\mathbf{B}$	matrix which contains derivatives of the shape functions
c	wave velocity
D	bending stiffness
E	Young's modulus of elasticity

f	frequency
$\mathbf{f}$	vector of external loading
$\mathbf{F}$	load
g	generalized coordinates
G	shear modulus
h	plate thickness
H	transfer function
I_y	moment of inertia
$\mathbf{J}$	Jacobian matrix
k	wave number
$\mathbf{K}$	stiffness matrix
l	polynomial degree
$\mathbf{M}$	mass matrix
M_z	bending moment around z-axis
n	normal on the FS interface
N	shape function
p	pressure
Q_y	transversal force in y-direction
$\mathbf{S}$	coupling matrix
S_{pp}	Auto power spectrum
S_{pu}	Cross power spectrum
$\mathbf{t}$	Vector of boundary conditions
T	kinetic energy
$\mathbf{T}_{CB}$	transformation matrix
u	displacement
U	potential energy
v	velocity
W	work
Z	impedance
Z_0	characteristic acoustic impedance

Greek Letters

α	absorption coefficient
ϵ	normal strain
ϕ	nodal rotations

Φ	displacement pattern applied for determinating the modal attachment modes
Φ_{pp}	Auto correlation function
Φ_{pu}	Cross correlation function
γ	shear strain
Γ^e	element boundary
Λ	squared eigenvalue
ν	Poisson coefficient
ρ	density
σ	normal stress
τ	shear stress
ω	circular frequency
Ω	circular frequency of the load
Ω^e	element domain
ξ, η	natural coordinates
δW	virtual work
Ψ	modes

Mathematical Symbols

$\circ\!\!-\!\!\bullet$	Fourier transformation
Re	real part of a complex number
Im	imaginary part of a complex number
i	imaginary number
$\frac{\partial(\ )}{\partial\theta}$	partial derivative with respect to the variable θ
$(\ )'$	derivative with respect to the coordinate x
$\dot{(\ )}$	derivative with respect to time
$(\ )^T$	transposed Matrix
$(\ )^{-1}$	inverse Matrix
$\det(\ )$	determinant of a Matrix
$\mathbf{I}$	identity matrix
∇	Nabla operator
Δ	gradient

1 Introduction

1.1 Motivation and State of the Art

In everyday engineering practice the problem of predicting the vibrational behavior of acoustical systems often occurs. Knowing the physical behavior of the systems is a prerequisite for providing a noise control and acoustic design.

Noise protection is very important for good working conditions in air enclosures like industrial work spaces, big office rooms or machinery rooms. Also people need to be protected from disturbing, vibration induced noise in their living surrounding as well as in all means of transport (air, rail and road vehicles). The idea of providing the acoustical comfort of people encouraged many researchers to work on the prediction of a sound field in an enclosed acoustic volume, [Cremer and Heckl 2010] [Fahy 2005], [Fahy and Gardonio 2007]. The prediction of the sound field is influenced by all the elements of the acoustical system and by their interaction. Therefore the system needs to be observed as a whole.

Numerous methods are used in vibroacoustics for prediction of vibrations and induced sound fields. The choice of the appropriate method is influenced by the characteristics of the system and the frequency range of interest, see figure 1.1. Analytical method provide an exact solution but their application is limited on simple systems. In the low frequency range the system can often be presented as a multibody oscillator. For higher frequency ranges and for more complex systems numerical and statistical methods have been developed. White color in figure 1.1 marks the transition zones between methods in which different hybrid approaches are possible (e.g. combination of numerical and statistical methods, or analytical and numerical methods).

It should be mentioned that the division on the low and high frequency range depends on the size of the system. Low frequency range usually considers the frequency band in which the influences of single resonances can easily be distinguished. For example, on the left-hand side of the figure 1.2 a room which has the volume of 25 m^3 is shown. The room is limited by a steel plate. At the steel plate a harmonic load F is applied. On the right-hand side

of the figure, the measured transfer functions between the load and sound pressure in 18 different points are given. The transfer functions differ significantly in the higher frequency range. These differences can be explained with the different contributions of single modes which have eigenfrequencies that are close to each other.

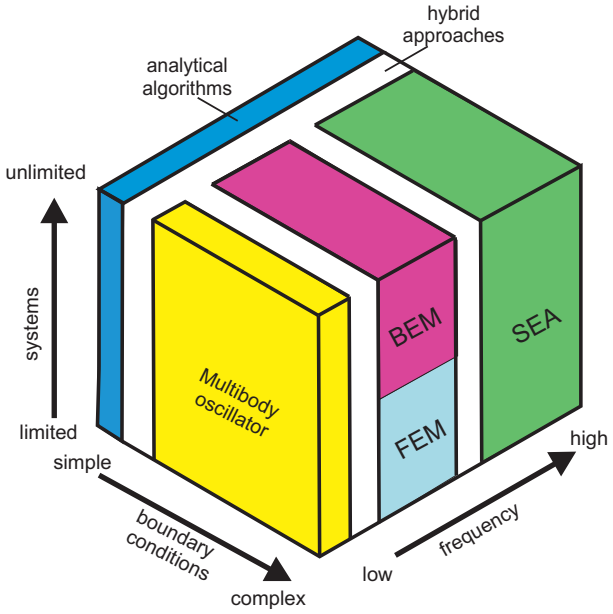

Figure 1.1: Methods used for vibroacoustical simulations, depending on the characteristics of the system and the frequency range, [Müller 2010]

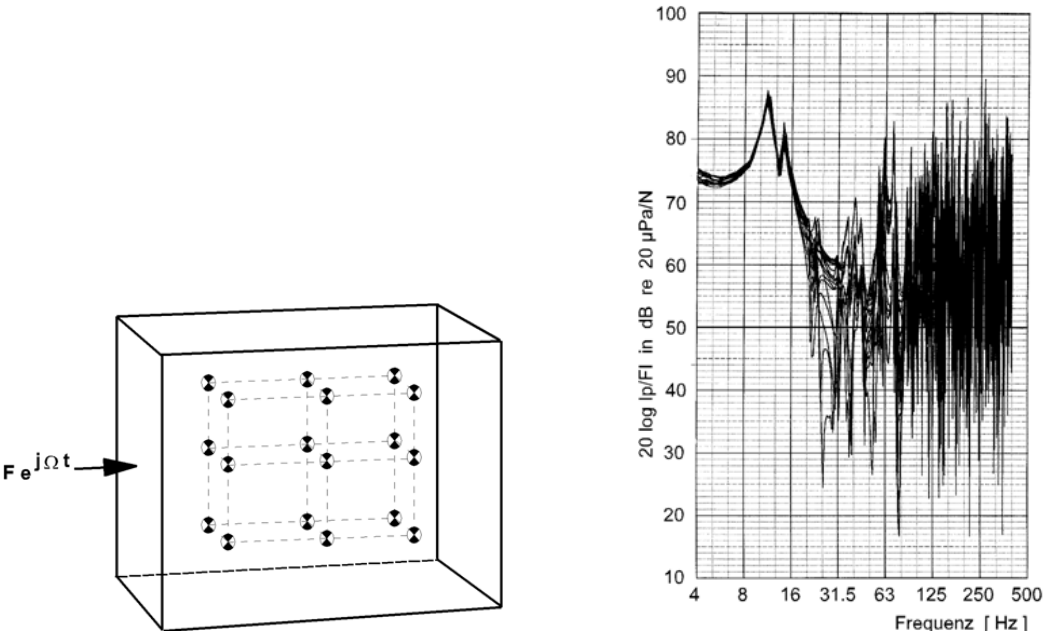

Figure 1.2: Measured transfer functions in vibroacoustics, [Müller 2010]

In the low frequency range (for vehicles and buildings - under 200 Hz) the prediction of the sound field in acoustic enclosures usually can be supported by means of the Finite Element Method (FEM). The application of this numerical method in acoustical problems is described in [Harari 2006] and [Thompson 2006]. In these methods the system is divided into a finite number of elements and the equation of motion of the system is solved for the degrees of freedom of the elements. Numerical methods like FEM or the Boundary Element Method (BEM) are convenient for detailed description of complex geometries and provide results with a spatial resolution of the sound field. They allow the calculation of the deterministic response of the system for deterministic load and defined model parameters. For higher frequencies, the reliability of this method might be significantly reduced due to discretization and also by the influence of small parameter variances, [Babuška et al 1997b] [Babuška et al 1997a]. Numerical models for higher frequencies require a very fine discretization which leads to extensive calculations.

In the high frequency range energy methods like the Statistical Energy Analysis are usually used, [Lyon and DeJong 1995] and [Keane and Price 1997]. This method is based on averaging over frequency bands, points of excitation and points of observation. Due to the averaging the assessment of influences of some changes on the sound field requires additional approaches, e.g. the effects produced by the change of the position of the absorber inside the cavity. Moreover, the resolution of the spatial distribution of the sound field and the possibility for a detailed description of the boundary conditions is reduced. The fluctuations in the frequency range, see figure 1.2, are smeared. For an appropriate application of the Statistical Energy Analysis the existence of a high modal density and a sufficient modal overlap is necessary. However, for lower frequencies the response of the system is predominated by individual, well separated resonances. In order to model the coupling of structural vibrations with the sound field inside of an acoustic cavity hybrid approaches that combine the SEA with FEM have been created, [Shorter and Langley 2005] [Langley 2008].

In this work the FEM is used for room acoustical simulations. Numerous model reduction methods have been developed over the years in order to reduce the calculation effort in numerical methods, [Schilders et al 2008]. The model reduction method that is developed in this work presents a modified version of the Craig-Bampton method, [Craig and Bampton 1968] [Craig 1981] [Craig 1995].

The Craig-Bampton method is a type of the Component Mode Synthesis (CMS) and has been developed from the Hurty's method, [Hurty 1967] [Collins et al 1972]. The basic idea of these methods is, in the first step, to divide the structure into a set of substructures. Afterwards, the analysis is performed on the substructure level. The substructures are represented with

generalized coordinates in the approximated model of the full system. The transformation from the degrees of freedom (DOFs) of a substructure to the generalized coordinates is done by using the component modes (Ritz vectors). Through the development of the CMS different types of the component modes were used, [Shyu et al 1997] [Jezequel 1985] [Goldman 1969]. A detailed overview of the development of the CMS and related works will be given in section 4.2. The Craig-Bampton method is very effective in reduction of the calculation time, especially when the influence of the modification of the system is investigated.

An idea for reducing the number of attachment modes necessary for the representation of a substructure was introduced in [Chan 2006]. The attachment modes are not anymore depending on the number of interface DOFs but on the frequency range of interest. In this thesis the method that uses modal attachment modes for solving complex fluid geometries and Fluid-Structure Interaction (FSI) problems is developed.

The FSI problems describe the coupling of the vibrating structures and the acoustic volume. The coupling method is described in [Bhattacharyya and Premkumar 2003] and [Wandinger 1994].

1.2 Layout of the Thesis

This thesis presents a model order reduction method based on the Craig-Bampton method. A modified version of the Craig-Bampton method is used for dividing an acoustic cavity into substructures. The solid structures at the boundaries of the fluid or inside of the fluid are treated as separate substructures.

Chapter 2 introduces the basic elements that can be found in an acoustic enclosure: the fluid, the vibrating structures and the absorbers. The chapter begins with the derivation of the wave equation in the fluid. In the following, the types of waves that can appear in solid structures are described. Also, the principles of the fluid-structure interaction and sound radiation are explained. At the end of this chapter the basic types of absorbers and the values that characterize them are given.

Numerical methods used for solving the equations of motion of the fluid and of the solid structure are given in Chapter 3. The first part of this chapter introduces the h-version of the FEM and the second part of the chapter describes the hp-version of the FEM. The choice of the shape functions and the determination of the element matrices for the fluid, structure and coupling FSI elements are explained. The FEM and the SFEM are used to calculate the normal and the attachment modes of the substructures.

At the beginning of Chapter 4 the historical development of the Component Mode Synthesis method is presented. Upon this the Craig-Bampton method is described in detail. Next, the idea for reducing the necessary number of attachment modes is introduced and its advantages are proven through several numerical examples. Afterwards, the determination of the steady-state solution with the help of the modal analysis is given. At the end of this chapter the application and the advantages of the modified Craig-Bampton method in FSI problems are shown.

Chapter 5 describes the acoustical measurements which were performed in the scope of this work in order to verify some simulation results. The chapter starts with the description of the correlation measurement technique which is used for determination of the Impulse Response Functions (IRF) and Transfer Functions (TF). Afterwards, the advantages and disadvantages of the different signal types are given. Finally, the measurements of absorption coefficients, impedances and pressure distribution are described and the results are compared with the simulations.

The conclusion of the presented work and the ideas for the future work are given in chapter 6.

2 Background

2.1 Representation of Sound Pressure in Time and Frequency Domain

A signal can be equivalently described in the time and in the frequency domain. The relation between the description of a signal in the time domain and in the frequency domain is given by the Fourier-series and the Fourier-integrals [Brigham 1997] [Müller 2010].

A signal which is repeated after a time period T is a periodic signal, see figure 2.1. The fundamental frequency of the periodic function f_0 is the reciprocal value of the time period: $f_0 = \frac{1}{T}$.

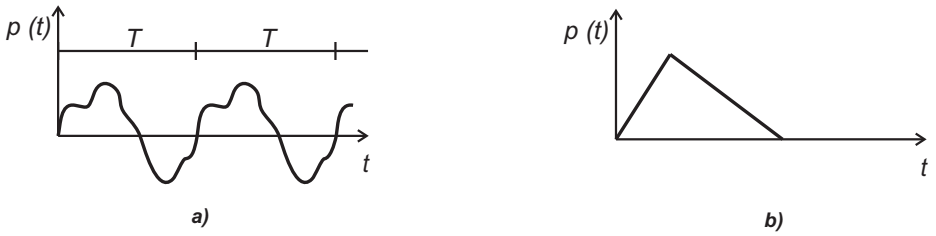

Figure 2.1: a) Periodic function, b) Transient function

The signal in the time domain can be given as a linear superposition of pressure oscillations with different time periods. With the help of Fourier-series, a periodical function $p(t)$ is described as follows:

$$p(t) = \sum_{r=1,2,\ldots} p_r e^{i(r2\pi f_0)t} \tag{2.1}$$

where p_r are complex Fourier-coefficients which are determined by minimizing the difference between the original function $p(t)$ and the Fourier-series and i is the imaginary number.

When the load is transient it can be considered to be periodic with the period $T \to \infty$ and in this case Fourier-series is substituted with a Fourier-integral.

$$p(t) = \int_{-\infty}^{+\infty} p(f) e^{i(2\pi f)t} dt \tag{2.2}$$

The spectral function of the signal is denoted with $p(f)$.

In this thesis the acoustical systems will be analyzed in the frequency domain. They are assumed to be linear, time-invariant (LTI) systems. For such a system the calculation of the response on an input signal is typically more numerically expensive in the time domain than in the frequency domain.

In the time domain the response is obtained as a convolution of the impulse response function of the system and the input signal, while in the frequency domain the steady state response is determined by multiplying the system's transfer function with the Fourier transformed of the input signal. In computer processing it is simpler and faster to perform the multiplication.

When the impulse response function (IRF) of the system is sought, a calculation in the frequency domain will not be time-saving. The Fourier transformed impulse signal is a constant spectrum for the frequencies from $-\infty$ to $+\infty$. Hence it is necessary to make an approximation of the impulse in order to obtain a reasonable number of frequencies for which the transfer function should be determined. In order to determine the IRF from the transfer function it is necessary to perform the inverse Fourier transformation (IFT), see figure 2.2.

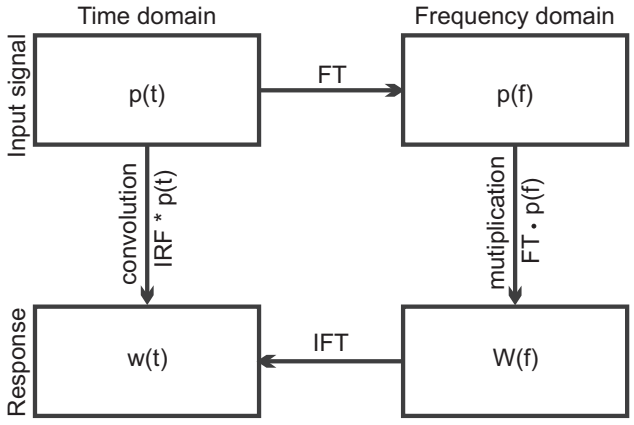

Figure 2.2: Calculation of the response of the system in the time and the frequency domain

However, the analysis of the system in the frequency domain in this work is reasonable since

the primary goal of the work is to determine the resonant frequencies of the acoustical system and solving the partial differential equations is simpler in the frequency domain, therefore it is not necessary to perform the IFT.

For the determination of the transfer function in the frequency domain the response of the system on the harmonic signal is analyzed. The response is harmonic and has the same frequency as the input signal, if only the steady-state part of the solution needs to be determined.

2.2 Sound in Enclosures

The acoustic behavior of an enclosure is influenced by the properties of all the individual elements of that acoustic system and also by their dynamic interaction. One acoustic system consists of various structural elements that contain or are surrounded by a fluid.

The basic difference between the acoustic behavior of a fluid in an enclosure and a fluid in an unbounded domain is the existence of the eigenmodes and their eigenvalues in an enclosure while in unbounded domain sound waves can propagate without interruption. The eigenmodes appear due to the interference of the intersecting waves.

The existence of the eigenmodes results in the fact that the response of the fluid on the vibration of the structures that are surrounding it or that are placed inside of the fluid is strongly frequency dependent [Fahy and Gardonio 2007]. Depending on the impedances of the adjoining structures a coupled model can be necessary. Thus, the interaction of the fluid and the structures needs to be modeled.

This thesis considers an acoustic system that consists of a fluid, vibrating structures and absorbers. In the following chapters the basic equations that describe the behavior of the components of the system and their interaction will be given.

2.2.1 The fluid

The basic difference between fluids and solids is the fact that the fluids cannot resist the shear force. Their common property is that they both resist the change of a volume. This property of the fluid allows the phenomenon of sound in fluids, [Fahy 2005].

The derivation of the wave equation

The wave equation describes a wave-like motion in solids, liquids, gas and electromagnetic waves.

The sound propagation in air is also described by the wave equation. The propagation of the air-borne sound is non-dispersive.

For the simplicity of the derivation and better understanding of the parameters that describe a wave motion, the wave propagation in 1-dimensional space will be observed. Afterwards, the wave equation in 3-dimensional space will be derived.

The 1-dimensional problem can be imagined as the air that fills out a long tube with a very small cross-section A, see figure 2.3 a). The pressure distribution over a cross-section is constant for each position x inside of the tube. The air can move only in the direction of the tube.

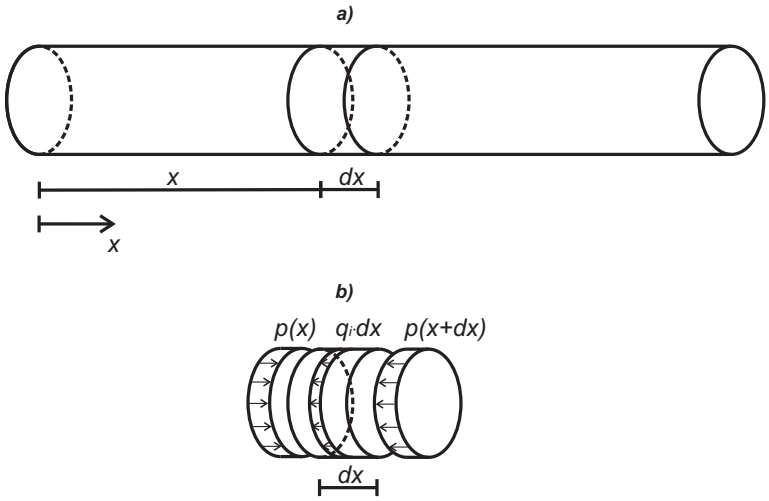

Figure 2.3: a) 1-dimensional fluid b) Forces acting on infinitesimally small part of the fluid, compare to [Müller 2010]

When the air inside of the tube is moving an inertia force is appearing. The inertia force $q_i(x,t)$ can be determined with the help of D'Alembert's principle:

$$q_i(x,t) = -\rho_f \cdot a_x(x,t) \tag{2.3}$$

where $a_x(x,t)$ marks the acceleration of the air and ρ_f is the density of the air.

The acceleration of the fluid is defined as:

$$a_x(x,t) = \frac{\partial^2 u_x(x,t)}{\partial t^2} = \frac{\partial v_x(x,t)}{\partial t}. \tag{2.4}$$

In (2.4) $v_x(x,t)$ marks the velocity of the fluid and $u_x(x,t)$ stands for displacements in longitudinal x-direction.

The pressure in the fluid is proportional to the strain in fluid ϵ:

$$p(x,t) = -\epsilon_x(x,t) \cdot E. \tag{2.5}$$

E stands for the Young's modulus of elasticity of the fluid. The strain in the fluid is defined as a change of length of the fluid:

$$\epsilon_x(x,t) = \frac{\partial u_x(x,t)}{\partial x}. \tag{2.6}$$

Taking into account equations (2.3)-(2.6) and by writing the the equilibrium of forces that are acting on the infinitesimally small part of the fluid (see figure 2.3 b) the following equations are obtained:

$$\frac{\partial^2 u_x(x,t)}{\partial x^2} - \frac{\rho_f}{E} \cdot \frac{\partial^2 u_x(x,t)}{\partial t^2} = 0 \tag{2.7}$$

$$\frac{\partial^2 p(x,t)}{\partial x^2} - \frac{\rho_f}{E} \cdot \frac{\partial^2 p(x,t)}{\partial t^2} = 0. \tag{2.8}$$

When the derivative with respect to time t is marked with $\cdot$ and the derivative with respect to the space x is marked with $'$ the equations (2.7) and (2.8) can be rewritten as:

$$\begin{aligned} u'' - \tfrac{\rho_f}{E}\ddot{u} &= 0 \\ p'' - \tfrac{\rho_f}{E}\ddot{p} &= 0 \end{aligned} \tag{2.9}$$

The wave velocity in fluid c_f is defined as:

$$c_f = \sqrt{\frac{E}{\rho_f}}. \tag{2.10}$$

After equation (2.10) is introduced in (2.9), the wave equation for the plane wave obtains its well-known form:

$$\begin{aligned} u'' - \tfrac{1}{c_f^2}\ddot{u} &= 0 \\ p'' - \tfrac{1}{c_f^2}\ddot{p} &= 0. \end{aligned} \tag{2.11}$$

A more detailed derivation of the 1d wave equation is presented in A.1.

For the derivation of the 3-dimensional wave equation figure 2.4 will be observed. The figure shows an infinitesimally small part of a 3d fluid on which the pressure and the inertia forces are acting.

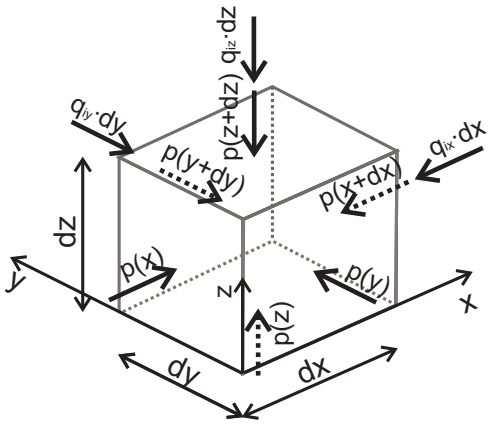

Figure 2.4: Infinitesimally small part of a 3d fluid on which the pressure and the inertia forces are acting

The inertia force for that occurs due to the motion of a 3d fluid is:

$$q_{ix} = -\rho_f \frac{\partial^2 u_x(x,y,z,t)}{\partial t^2} \qquad q_{iy} = -\rho_f \frac{\partial^2 u_y(x,y,z,t)}{\partial t^2} \qquad q_{iz} = -\rho_f \frac{\partial^2 u_z(x,y,z,t)}{\partial t^2} \quad . \tag{2.12}$$

After writing the equilibrium of forces for the infinitesimally small part of the fluid in cartesian coordinates shown in figure 2.4 we obtain:

$$\frac{\partial p}{\partial x} = -\rho_f \frac{\partial^2 u_x(x,y,z,t)}{\partial t^2} \qquad \frac{\partial p}{\partial y} = -\rho_f \frac{\partial^2 u_y(x,y,z,t)}{\partial t^2} \qquad \frac{\partial p}{\partial z} = -\rho_f \frac{\partial^2 u_z(x,y,z,t)}{\partial t^2} \quad . \tag{2.13}$$

By using the gradient notation these three equations can be connected into one vector equation, [Cremer and Müller 1976]:

$$\nabla p = -\rho_f \frac{\partial^2 \mathbf{u}}{\partial t^2}. \tag{2.14}$$

Equivalently like in equations (2.5) and (2.6) pressure in a 3d fluid can be described as a function of the change of volume:

$$p = -\left(\frac{\partial u_x}{\partial x} + \frac{\partial u_y}{\partial y} + \frac{\partial u_z}{\partial z}\right) \cdot E, \tag{2.15}$$

which can be also written is vector notation as:

$$div\mathbf{u} = -\frac{1}{E} p. \tag{2.16}$$

After applying the divergence operation on the equation (2.14) we obtain:

$$div\nabla p = -\rho_f div\frac{\partial^2 \mathbf{u}}{\partial t^2}. \tag{2.17}$$

Because the time and space derivatives are independent equation (2.17) can also be written as [Cremer and Müller 1976]:

$$div\nabla p = -\rho_f \frac{\partial^2}{\partial t^2}\left(div\mathbf{u}\right). \tag{2.18}$$

Now equation (2.16) can be introduced into (2.18) and finally the wave equation for a 3d fluid is obtained:

$$\Delta p = \frac{1}{c_f^2}\ddot{p}. \tag{2.19}$$

With Δ the Laplace operator is marked and c_f denotes the wave velocity in the fluid.

The same can be written in extended form:

$$\frac{\partial^2 p}{\partial x^2} + \frac{\partial^2 p}{\partial y^2} + \frac{\partial^2 p}{\partial z^2} = \frac{1}{c_f^2}\cdot\frac{\partial^2 p}{\partial t^2}. \tag{2.20}$$

The wave equation can also be written in spherical (2.21) and cylindrical coordinates (2.22).

$$\frac{1}{R^2}\frac{\partial}{\partial R}\left(R^2\frac{\partial p}{\partial R}\right) + \frac{1}{R^2 sin\vartheta}\frac{\partial}{\partial R}\left(sin\vartheta\frac{\partial p}{\partial \vartheta}\right) + \frac{1}{R^2 sin^2\vartheta}\left(\frac{\partial^2 p}{\partial \varphi^2}\right) = \frac{1}{c_f^2}\cdot\frac{\partial^2 p}{\partial t^2} \tag{2.21}$$

$$\text{with} \qquad R = \sqrt{x^2+y^2+z^2}.$$

Spherical coordinates are sketched in figure 2.5.

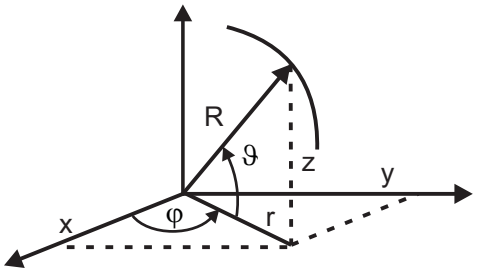

Figure 2.5: Spherical coordinates

In cylindrical coordinates the wave equation becomes:

$$\frac{1}{R}\frac{\partial}{\partial R}\left(R\frac{\partial p}{\partial R}\right)+\frac{1}{R^2}\frac{\partial^2 p}{\partial \varphi^2}+\frac{\partial^2 p}{\partial x^2}=\frac{1}{c_f^2}\cdot\frac{\partial^2 p}{\partial t^2} \tag{2.22}$$

$$\text{with} \qquad R=\sqrt{y^2+z^2}.$$

Cylindrical coordinates are shown in figure 2.6.

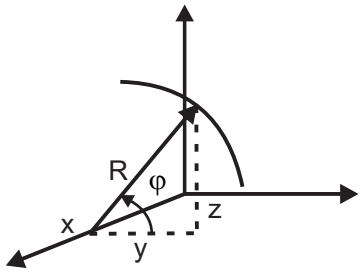

Figure 2.6: Cylindrical coordinates

The wave equation can be transformed into the frequency domain which results in the Helmholtz equation for the pressure $p(x, y, z)$ in the frequency domain:

$$\Delta p=-\frac{\omega^2}{c_f^2}p. \tag{2.23}$$

Here the derivative theorem

$$\frac{d^n}{dt^n}f(t)\ \circ\!\!-\!\!\bullet\ (2\pi i f)^n F(f) \tag{2.24}$$

is applied. In equation (2.23) ω marks the circular frequency ($\omega = 2\pi f$). The Fourier transformation is marked with $\circ\!\!-\!\!\bullet$ and $F(f)$ is Fourier transformation of the function $f(t)$.

Selected Analytical Solutions of the Helmholtz equation

The following analytical solutions of the Helmholtz equations give an insight into the waves that can occure. A general solution of the wave equation can be formed out of superposition of these waves and it is not connected with any specific sound source.

- Plane waves:

$$p(x,y,z,t) = Ae^{i(k_x x+k_y y+k_z z\pm\omega t)} = Ae^{i(\mathbf{kx}\pm\omega t)}$$
$$\text{with} \quad \mathbf{k} = \begin{bmatrix} k_x \\ k_y \\ k_z \end{bmatrix} \quad \text{and} \quad \mathbf{x} = \begin{bmatrix} x & y & z \end{bmatrix} \tag{2.25}$$

  In a 1-dimensional fluid plane waves are defined as:

$$p(x,y,z,t) = Ae^{i(k_x x\pm\omega t)} = f_1(k_x x+\omega t) + f_2(k_x x-\omega t) = f_1(x_+) + f_2(x_-) \tag{2.26}$$

  The function $f_1(x_+)$ represents the wave that is traveling in the negative x direction and the function $f_1(x_-)$ represents the wave that is traveling in the positive x direction. When the wave is propagating in an infinitely long tube only one of the functions exists.

- A spherical wave is propagating in all directions from a point source. The distance from the source is marked with r.

$$p(r,t) = \frac{A}{r}e^{i(kr-\omega t)} \tag{2.27}$$

- A cylindrical wave is generated by a line source with constant values along the coordinate x. The distance from the source is marked with r.

$$p(r,t) = \frac{A}{\sqrt{r}}e^{i(kr-\omega t)} \tag{2.28}$$

2.2.2 Vibrating Structures

Vibrating structures are parts of acoustic systems. They can be found at the boundaries of the fluid as well as inside. The vibrating structures can behave as a sound source or a sound absorber. The absorbing behavior of the vibrating structures will be explained in section 2.2.3.

Vibrating structures behave as absorbers when they vibrate due to the incident sound. They influence the sound field inside of the enclosure by their vibration.Their behavior is typically described by their reflecting and absorbing characteristics.

The structure can behave as a sound source, e.g. if an external force is applied on the structure. Then the structure excites the fluid with its movement and sound is radiated.

Waves in Structures

Displacements and stresses in a homogeneous, isotropic and linearly-elastic material are described with the Lamé equation A.2.7. A way for solving this equation using Helmholtz decomposition is shown in A.2.2. Through this solution it is shown that in an unbounded 3d continuum, unlike fluid, two types of waves can appear - compressional and shear waves.

However in this work beam- or plate-like structures are observed and an approach for solving the Lamé equation that differs from Helmholtz approach can be applied. This approach is used because for the analysis of thin structures certain simplifications can be applied.

For deriving the equation of motion for a thin beam the Euler-Bernoulli beam theory is used. This theory is valid for linearly elastic, isotropic material. It is assumed that the cross-section of the beam remains plane and perpendicular to the deformed axis of the beam, which means that the shear deformation can be neglected, [Graff 1991]. These assumptions are usually fulfilled in long, thin beams when the hight of the beam is 8-10 times smaller than the wave length of the bending wave. When the wave length gets shorter, higher beam theories need to be applied.

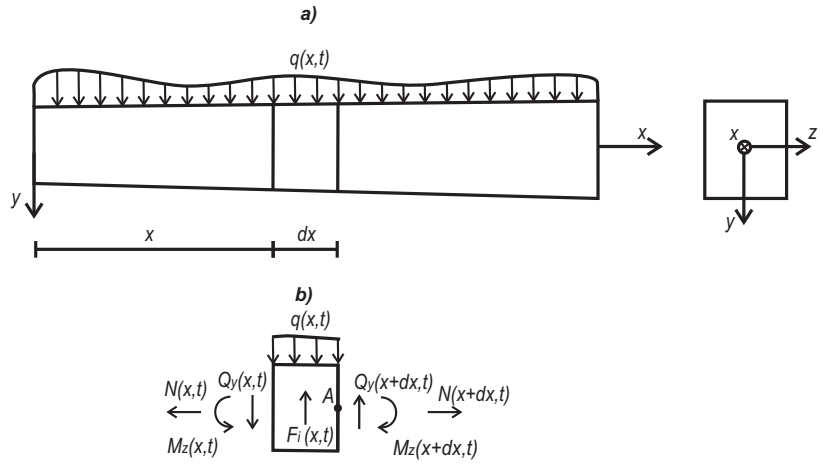

Figure 2.7: a) A solid beam exposed to a distributed, transverse load $q(x,t)$ b) Equilibrium of an infinitesimal part of the beam

Figure 2.7 a) shows a beam which is loaded by a continuously distributed transverse load $q(x,t)$.

It is assumed that the distributed transverse load causes only transverse displacement and curvature of the cross-section, [Timoshenko 1953] [Bauchau and Craig 2009]. Considering

this assumption as well as the assumptions of the Euler-Bernoulli theory the displacement field becomes:

$$\begin{aligned} u_x(x,y,z) &= -y\frac{du_y(x)}{dx} \\ u_y(x,y,z) &= u_y(x) \\ u_z(x,y,z) &= 0. \end{aligned} \tag{2.29}$$

Figure 2.7 b) presents the equilibrium of an infinitesimally small part of that beam. M_z marks the bending moment around the z-axis, Q_y is the transversal force and q_i is the inertia force. The inertia force equals: $q_i = m\frac{\partial^2 u_y}{\partial t^2}$, where m marks the mass of the solid element.

According to linearized theory the following definitions of normal and shear strains $(\epsilon_x, \epsilon_y, \gamma_{xy})$ are obtained:

$$\begin{aligned} \epsilon_x &= \frac{\partial u_x}{\partial x} \\ \epsilon_y &= \frac{\partial u_y}{\partial y} \\ \gamma_{xy}(x,y,z) &= \frac{\partial u_x}{\partial y} + \frac{\partial u_y}{\partial x}. \end{aligned} \tag{2.30}$$

From Hooke's law the normal stress in x direction σ_x can be calculated:

$$\sigma_x = E \cdot \epsilon_x = E \cdot \frac{\partial u_x}{\partial x} = E \cdot y \cdot \frac{\partial^2 u_y}{\partial x^2}. \tag{2.31}$$

Now the bending moment around the axis z can be calculated:

$$M_z = \int_A \sigma_x \cdot y \cdot dA = \int_A E \cdot y^2 \cdot \frac{\partial^2 u_y}{\partial x^2} dA = EI_z \frac{\partial^2 u_y}{\partial x^2} \tag{2.32}$$

with

$$I_z = \int_A y^2 dA. \tag{2.33}$$

The equilibrium of the vertical forces that are acting on the part of the beam shown in figure 2.7 b) gives the following expression:

$$-\frac{\partial Q_y}{\partial x} - m\frac{\partial^2 u_y}{\partial t^2} + q(x,t) = 0. \tag{2.34}$$

From the equilibrium of the bending moments around the point marked with A and after neglecting the small terms of higher order we become:

$$\frac{\partial M_z}{\partial x} + Q_y(x,t) = 0. \tag{2.35}$$

By combining equations (2.32), (2.34) and (2.35) the equation of motion of the beam is

received, [Timoshenko 1953]:

$$EI\frac{\partial^4 u_y}{\partial x^4} + m\frac{\partial^2 u_y}{\partial t^2} = q(x,t). \tag{2.36}$$

In case of free vibrations equation (2.36) becomes:

$$EI\frac{\partial^4 u_y}{\partial x^4} + m\frac{\partial^2 u_y}{\partial t^2} = 0. \tag{2.37}$$

For the bending wave equation we will assume the solution of the form:

$$u_y = Ae^{i(kx-\omega t)}. \tag{2.38}$$

This solution can now be introduced in equation (2.37) and we obtain:

$$EIk^4 - m\omega^2 = 0. \tag{2.39}$$

The bending wave number k can now be calculated from:

$$k^4 = \frac{\omega^2 m}{EI}. \tag{2.40}$$

It can be seen that this equation has eight solutions, so finally the solution of the equation (2.37) is:

$$\begin{aligned} u_y = \quad & \left(A^+e^{-ik_b x} + B^+e^{-k_b x} + C^+e^{+ik_b x} + D^+e^{+k_b x}\right) \quad e^{i\omega t} \quad + \\ & \left(A^-e^{+ik_b x} + B^-e^{+k_b x} + C^-e^{-ik_b x} + D^-e^{-k_b x}\right) \quad e^{-i\omega t} \end{aligned} \tag{2.41}$$

with

$$k_b = \sqrt{\omega}\sqrt[4]{\frac{m}{EI}}. \tag{2.42}$$

A, B, C and D mark complex constants ($^+$ and $^-$ values mark the complex conjugate pair). The first component of in equation (2.41) marks the wave propagating in positive x-direction, the second component is the near field in positive x-direction, and the third and the forth component mark the propagating and near field wave in negative x-direction. The near field effects can typically be neglected at the certain distance from the edge. Finally the speed of the bending wave c_b can be determined:

$$c_b = \lambda f = \frac{2\pi}{k_b} f = \frac{\omega}{k_b} = \sqrt{\omega}\sqrt[4]{\frac{EI}{m}} \tag{2.43}$$

As it can be seen the speed of the bending wave is frequency dependent, or in other words: The bending waves are dispersive. In equation (2.43) ω marks the frequency of the bending

wave.

According to Kirchhoff-Love theory of plates (classical plate theory) the partial differential equation of a thin plate that is positioned in $x - y$ plane is given by:

$$D\left(\frac{\partial^4 u_z}{\partial x^4} + 2\frac{\partial^4 u_z}{\partial x^2 \partial y^2} + \frac{\partial^4 u_z}{\partial y^4}\right) + m\frac{\partial^2 u_z}{\partial t^2} = 0. \tag{2.44}$$

D marks the bending stiffness.

$$D = \frac{Eh^3}{12(1-\nu^2)} \tag{2.45}$$

In (2.45) h stands for the thickness of the plate. It is assumed that: $u_z << h$ and that the wave length of the bending waves is much larger than h. Similar to (2.38) can again assume the solution of the equation (2.44) in the following form:

$$u_z = Ae^{i(k_x x + k_y y + \omega t)} \tag{2.46}$$

After introducing this solution into eqaution (2.44) we recieve the following expression:

$$D(k_x^2 + k_y^2)^2 - m\omega^2 = 0. \tag{2.47}$$

Similar to equation (2.41), the solution of this equation gives the propagating and near field waves in positive and in negative x and y direction. Figure 2.8 shows a bending wave that is propagating in positive x and y direction. This wave represents one of the possible solutions of equation (2.47). If the plate is infinitely long the the bending wave in the plate with wave lengths λ_x and λ_y corresponds to the bending wave in a beam with the wave length $\frac{1}{\lambda_w^2} = \frac{1}{\lambda_x^2} + \frac{1}{\lambda_y^2}$. The beam is perpendicular to the wave front.

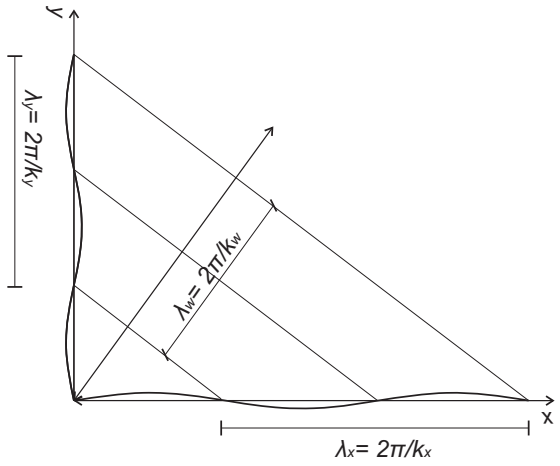

Figure 2.8: Bending waves in the plate

The Fluid-Structure Interaction

The formulation of the fluid-structure interaction problem depends on the variables that are used for describing the vibration pattern of the fluid and of the structure. In the structure the variable is generally the displacement while in the fluid several formulations are possible. In [Wandinger 1994] different formulations of the fluid are divided into two groups: simple and redundant formulations. A formulation is simple if one scalar field is used to describe the fluid while redundant formulations use more functions than necessary to describe the fluid. Variables in simple formulations can be: the pressure, the displacement potential or the velocity potential. In redundant formulations a displacement field or a combination of the pressure and the displacement potential is used.

Many authors, including [Wang and Bathe 1997], [Bao et al 2001] and [Wang 2008] used redundant formulations. These formulations are self-adjoint and therefore no additional interface conditions need to be applied. However, it is known that in these formulations spurious non-zero frequency circulation modes appear. In order to avoid this effect, additional constraints need to be introduced. Moreover, like the name redundant already shows, the number of variables that is used is larger than necessary (e.g. if the displacement formulation is used the number of unknowns in the fluid is three times bigger compared to the pressure formulation) which requires large memory capacity of computers.

In order to reduce the number of variables, in this work a pressure description of the fluid is chosen. In this formulation the fluid-structure formulation problem requires the coupled system that consists of the elastic equation of the structure, the fluid equation and the interface conditions that will bring asymmetric terms in the system mass and stiffness matrices. When the system matrices are asymmetric the computational time is longer, however, these negative effects can be diminished by using a method for acceleration of the computation which is presented in chapter 4.5.

The influence of the structure on the fluid can be included into the fluid equation of motion (2.19) in two manners. Firstly, it can be introduced as a boundary condition in which case the equation of motion will be homogeneous if no additional load is acting on the fluid. Secondly, it can be represented as forces that are acting on an unbounded fluid domain, [Fahy 2005]. In this dissertation the vibrating structures will be introduced as a boundary condition.

When the fluid is surrounded with rigid walls the boundary condition for the wave equation (2.19) is:

$$\frac{\partial p}{\partial n} = 0 \tag{2.48}$$

Where n marks the normal on the fluid boundary.

If instead of a rigid wall, a vibrating structure is limiting fluid the change of volume in the direction perpendicular to the interface is proportional to the accelerations of the structure (law of inertia):

$$\frac{\partial p}{\partial n} = -\rho_f \cdot \ddot{u}_n \tag{2.49}$$

$\ddot{u}_n$ marks the component of the fluid acceleration in direction normal to the common interface. This acceleration is caused by the movement of the structure and therefore $\ddot{u}_n = \ddot{u}_s$, where $\ddot{u}_s$ stands for the acceleration of the structure.

The fluid pressure that is acting on the interface is applied as a force on the structure. This load is acting over the whole interface between the fluid and the structure. This interface is usually referred to as the *wet* interface [Bhattacharyya and Premkumar 2003]. So the equation of motion e.g. of a 1-dimensional beam-like structure becomes:

$$EI\frac{\partial^4 u_y}{\partial x^4} + m\frac{\partial^2 u_y}{\partial t^2} = pb. \tag{2.50}$$

Here b marks the width of the wet surface.

The numerical solution for now described fluid-structure interaction problem will be given in chapter 3.

Sound radiation to an infinite domain

Now the radiated sound pressure from an infinite plate placed in the $x - y$ plane at the position $z = 0$ will be determined. The plate's oscillation pattern can be described via a Fourier approach. One element of the Fourier approach is given by:

$$v^s(x, y, t) = v_0 e^{-ik_{sx}x} e^{-ik_{sy}y} e^{-i\Omega t} \tag{2.51}$$

where the v^s marks the velocity of the plate, k_{sx} and k_{sy} are the wave numbers in the plate in x and y direction. Now the expected solution of the wave equation is:

$$p(x, y, z, t) = p_0 e^{-ik_{sx}x} e^{-ik_{sx}y} e^{-ik_z z} e^{-i\Omega t} \tag{2.52}$$

We now just observe the radiated wave which is propagating in the positive z direction. In equation (2.52)k_z mark the wave numbers in fluid in z direction for the frequency Ω.

After introducing the solution (2.52) in (2.20) the wave equation receives the following form, [Cremer et al 2005]:

$$\left(k_{sx}^2 + k_{sy}^2 + k_z^2 - \frac{\Omega^2}{c_f^2}\right) p(x,y,t) = 0, \tag{2.53}$$

where c_f mark the speed of sound in the fluid.

This equation is always fulfilled if:

$$k_{sx}^2 + k_{sy}^2 + k_z^2 - \frac{\Omega^2}{c_f^2} = 0. \tag{2.54}$$

From (2.54) the wave number in z-direction k_z equals:

$$k_z^2 = \frac{\Omega^2}{c_f^2} - k_{sx}^2 - k_{sy}^2. \tag{2.55}$$

The ratio $\frac{\Omega^2}{c_f^2}$ can also be marked with k and it defines the total wave number in the fluid:

$$k^2 = k_{sx}^2 + k_{sy}^2 + k_z^2. \tag{2.56}$$

When the fluid borders an oscillating plate at the position $z = 0$ the velocity of the fluid in z direction v_z^f at the boundary needs to equal the velocity of the plate v^s, [Cremer and Heckl 2010]:

$$v_z^f(z = 0, x, y) = v^s(x, y). \tag{2.57}$$

From the law of inertia the velocity of the fluid can be determined:

$$\mathbf{v}^f = \frac{1}{i\Omega\rho_f}\nabla(p). \tag{2.58}$$

Therefore, the velocity in y direction is defined as:

$$v_z^f(x,y,z,t) = \frac{p_0 k_z}{\Omega\rho_f} e^{-ik_{sx}x} e^{-ik_{sy}y} e^{-ik_z z} e^{i\Omega t}. \tag{2.59}$$

After introducing expressions (2.51) and (2.59) into boundary condition (2.57) at the position $z = 0$, the amplitude of the radiated pressure in the fluid is resulting in:

$$p_0 = \frac{\Omega\rho_f}{k_z} v_0 = \rho_f c_f \frac{k}{k_z} v_0. \tag{2.60}$$

Now this pressure amplitude can be introduced in the solution of the wave equation (2.52) and the sound pressure radiated from an oscillating plate is:

$$p(x,y,z,t) = \frac{\rho_f c_f v_0}{\sqrt{1-\frac{k_{sx}^2+k_{sy}^2}{k^2}}} e^{-ik_{sx}x} e^{-ik_{sy}y} e^{-i\sqrt{k^2-k_{sx}^2-k_{sy}^2}z} e^{i\Omega t}. \tag{2.61}$$

The ratio of the wave numbers in the plate and in the fluid $\frac{k_{sx}^2+k_{sy}^2}{k^2}$ determines the radiation of the sound of a plate. If $k_{sx}^2 + k_{sy}^2 > k$ the value $\sqrt{1-\frac{k_{sx}^2+k_{sy}^2}{k^2}}$ is imaginary and the sound field is declining exponentially with the distance z from the plate. The sound field is given by:

$$p(x,y,z,t) = \frac{\rho_f c_f v_0}{i\sqrt{\left|1-\frac{k_{sx}^2+k_{sy}^2}{k^2}\right|}} e^{-ik_{sx}x} e^{-ik_{sy}y} e^{-\sqrt{\left|k^2-k_{sx}^2-k_{sy}^2\right|}z} e^{i\Omega t}. \tag{2.62}$$

In this case the vibration of the plate causes only local or near field disturbances in the adjacent fluid. The particles of the fluid show elliptical motion and no power is radiated, see figure 2.9 left.

Figure 2.9 illustrates the effect of the vibrating structure on the fluid. With k_s the wave number in the vibrating plate is marked ($k_s^2 = k_{sx}^2 + k_{sy}^2$).

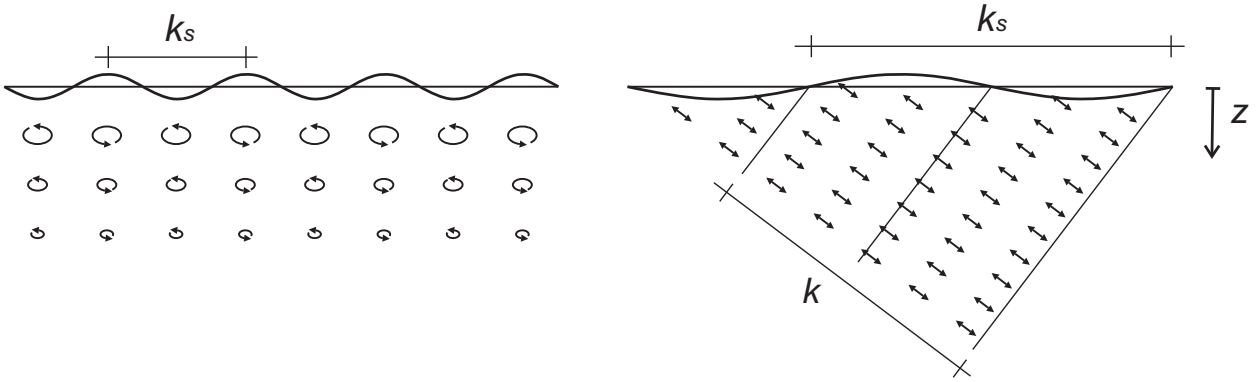

Figure 2.9: Schematic representation of the radiation of the sound from a vibrating structure, [Müller 2010]

When $k_{sx}^2 + k_{sy}^2 < k$ the value $\sqrt{1-\frac{k_{sx}^2+k_{sy}^2}{k^2}}$ is real and the plate emits the progressive waves and the radiation of the plate has far field effects. The radiated sound pressure waves are:

$$p(x,y,z,t) = \frac{\rho_f c_f v_0}{\sqrt{1-\frac{k_{sx}^2+k_{sy}^2}{k^2}}} e^{-ik_{sx}x} e^{-ik_{sy}y} e^{-i\sqrt{k^2-k_{sx}^2-k_{sy}^2}z} e^{i\Omega t}. \tag{2.63}$$

These waves are shown on the right side of figure 2.9.

The limiting frequency that separates the near field and far field radiation of the plate is the frequency for which the speed of sound in fluid equals the speed of bending waves in the plate $c_f = c_b$, see equation (2.43). This frequency is called the coincidence frequency f_c and it is calculated from:

$$f_c = \frac{1}{2\pi} \frac{c_f^2}{\sqrt{\frac{EI}{m}}}. \tag{2.64}$$

where E, I and m mark the Young's modulus, the inertia and the mass of the plate.

Figure 2.10 shows the coincidence frequency as a border between near and far field radiation of an infinite plate. It can be seen that for the frequencies lower than the coincidence frequency the speed of bending waves is smaller then the speed of sound, hence, the vibration of the plate will cause only near field disturbances in the fluid.

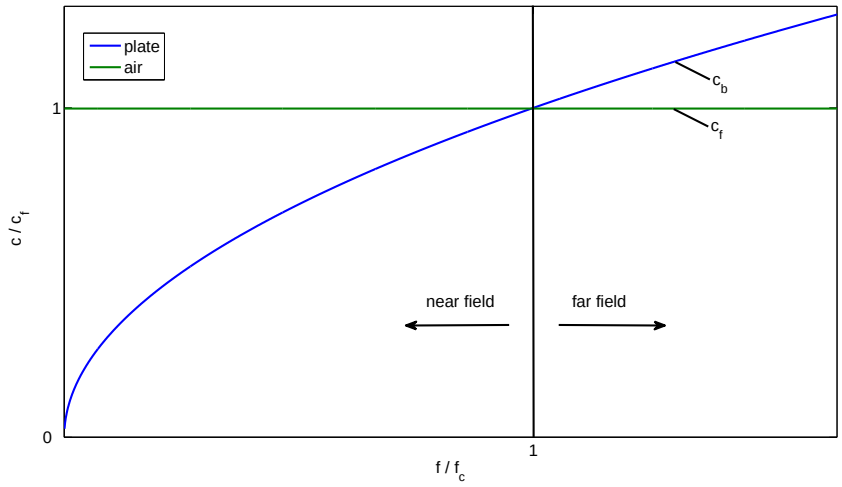

Figure 2.10: Coincidence frequency as a border between near and far field radiation of an infinite plate

The radiation of a structure that has a finite dimensions can also be analysed with respect to the ratio of the wave number in the structure and in the fluid. Figure 2.11 shows the oscillation of a plate in the spatial x-domain and in the wave number domain. In case when an infinitely long plate is oscillating in the sinusoidal form, in the wave number domain the oscillations of the plate is described with two Dirac-functions of the amplitude $\frac{v_0}{2}$ at the position $\pm k_b$, where the $k_b = \frac{\Omega}{c_b}$ marks the wave number in the plate for the frequency Ω and the speed of the bending wave c_b, see figure 2.11 d).

When the structure has finite dimensions the oscillation pattern can be obtained by multiplying the infinite sinus function of the equivalent beam with a window function that starts at $-\frac{A}{2}$ and ends at $\frac{A}{2}$ in the spatial x-domain, where A corresponds to the area of the plate (see figure 2.11 b)). A sinus cardinalis function in the transformed domain corresponds to a window function in the original domain and the multiplication is substituted with the convolution.

After the convolution of the two Dirac functions, figure 2.11 d), and the sinus cardinalis function, figure 2.11 e), the description of the oscillation of a finite plate in the wavenumber domain is received, see figure 2.11 f).

The gray rectangle in figures 2.11 d) and f) marks the range of the wave numbers that are relevant for the radiation (values for which the structure radiation has far field effects), [Müller et al 2006].

In figure 2.11 f) it can be seen that even when $k_b > k$ there will still be wave lengths that radiate sound. However, the intensity of the radiated sound will be increased significantly when $k_b < k$.

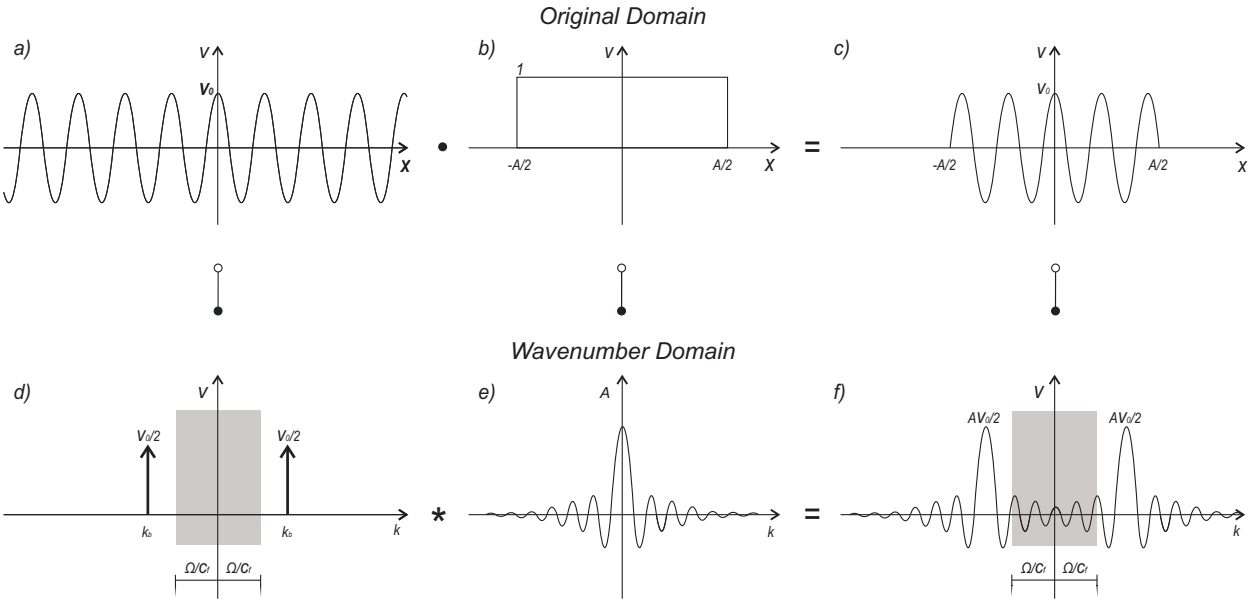

Figure 2.11: Representation of the velocity of the plate for the frequency Ω in the spatial x-domain and in the wave number domain, [Müller et al 2006]

2.2.3 Absorbers

In 2.2.1 and 2.2.2 it has been described how the sound waves are traveling through fluids and elastic structures. It has also been mentioned that vibrating structures can absorb the part of the acoustic energy of the sound wave. In this chapter the absorption phenomenon and the most commonly used absorbers in room acoustics will be described.

When a sound wave arrives at the boundary of the fluid the related energy will only be partly reflected while the other part will be transmitted or absorbed. Figure 2.12 shows how an incident wave with the energy E_i is after the contact with the boundary reflected E_r, transmitted E_t and absorbed E_a.

The absorption coefficient α is described as the ratio between the not reflected energy and the incident energy:

$$\alpha = \frac{E_t + E_a}{E_i} = \frac{E_i - E_r}{E_i} = 1 - r. \tag{2.65}$$

The reflection coefficient is marked with r.

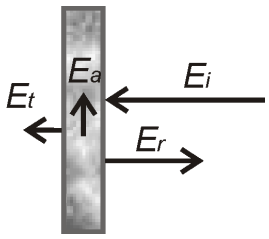

Figure 2.12: Incident wave E_i is after the contact with the boundary reflected E_r, transmitted E_t and absorbed E_a

The most commonly used absorbers in room acoustics can be divided into passive absorbers, plate and Helmholtz resonators [Fuchs 2007]. These three types of absorbers are sketched in figure 2.13. Number 1 in the figure marks the porous material, number 2 stands for the air cushion, the plate and the reflective wall are denoted with numbers 3 and 4, respectively. The thickness of the porous material is marked with d_p and the thickness of the air cushion is d_a.

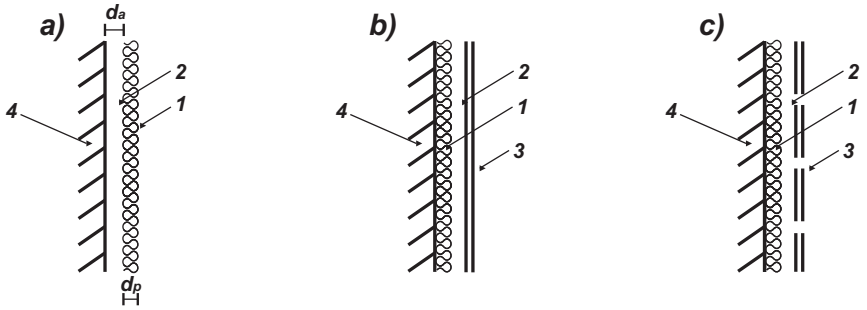

Figure 2.13: a) Passive absorber, b)Plate resonator and c) Helmholtz resonator

Passive absorber

Passive absorbers are built from porous or fibrous materials such as foams, textiles, mineral wool or cotton wool. When a sound wave enters the absorber it causes vibration of the fibrous or open-pored structured material. These vibrations cause friction inside of the material which reduces the kinetic energy of the sound wave. Consequently the effect of the porous absorber is higher if the sound velocity is also higher, [Fuchs 2007], [Buchschmid and Müller 2008].

At the position of a totally reflective wall the sound pressure of the sound wave has its maximum while the sound velocity equals zero. The sound velocity has its maximum at the position that is one quarter of the wave length distanced from the wall. Therefore, the absorber needs to be either thick enough in order to absorb the sound waves at limiting low frequency effectively or it can be placed at a certain distance d_a from the reflective wall like it is shown in figure 2.13 a).

Plate and Helmholtz resonators

At the resonant frequency of Plate and Helmholtz resonators the energy is absorbed due to their resonant vibrations.

Plate resonators are typically low frequent absorbers. Depending on the ratio between frequency of excitation and coincidence frequency they can be modeled as a mass-spring system or a plate. They consist of a plate that is placed in front of an air cushion. The cushion can be filled with a porous material like it is shown in figure 2.13 b). The resonant frequencies of such a system depend on the boundary conditions and mass of the plate as well as from the the depth of the cushion and the material that it is filled with. By adjusting this parameters

it is possible to obtain the desired resonant frequencies of the absorber, [Fuchs 2007], [Ford and McCormick 1969].

The sound waves excite the plate and the sound energy of the wave is dissipated by the damping inside of the plate or by the porous layer.

By using perforated plates Helmholtz resonators are obtained, see figure 2.13 c). When the sound wave arrives to the resonator the air inside of the perforations starts oscillating and it behaves as an inert mass and it is added to the mass of the plate. The air cushion behind the resonator acts like a spring. The mass of the air inside of the slots and holes of the absorber should not be small compared to the mass of the air moved by the incident wave [Fuchs 2007]. The area-related mass of the air moved by a wave can be determined from: $m''_a = \frac{\rho_0 \lambda}{2\pi}$, with ρ_0 marking the density of the air and λ the wave length.

The bandwidth of the Helmholtz resonators can be increased the same way like for plate resonators by filling the cavity behind the resonator with a porous layer but it can also be increased by changing the flow resistance by adding a fleece material in front or behind the holes and slots.

The perforations can be created in such a way that the absorber obtains several eigenvalues that lie close to each other. This way the Helmholtz resonators can become the broadband absorbers.

Modeling of absorbing boundary conditions

In order to include absorbers in the model of an acoustic enclosure it is necessary to model a boundary condition for a fluid that is at the same time able to reflect and to absorb the sound waves. The degree to which the sound waves are absorbed and reflected can be described by the acoustic impedance.

The acoustic impedance is defined as the ratio between the complex amplitude of the harmonic pressure and the associated particle velocity or the volume velocity through a surface, [Fahy 2005].

One possible solution of the wave equation is given in 2.25. For a specific case in which the waves are perpendicular on the surface of the absorber, the pressure distribution over the absorber area is constant and $k_x = k_y = 0$. Hence, when a harmonic loading with the

amplitude p_0 and frequency Ω is acting on the fluid the pressure waves are defined as:

$$p(z,t) = (\underbrace{p_0 e^{-ik_z z}}_{p_i} + \underbrace{r p_0 e^{ik_z z}}_{p_r}) e^{i\Omega t}. \tag{2.66}$$

The incident wave is marked with p_i and p_r is the reflected wave. The ratio between the amplitudes of the reflected and the incident wave is the reflection coefficient r. The wave number is marked with k.

With the help of the law of inertia the sound velocity can be determined:

$$v(z,t) = \frac{i}{\Omega\rho}\frac{\partial p(z,t)}{\partial z} = \frac{p_0}{\rho c}(\underbrace{e^{-ikz}}_{p_r} - \underbrace{r e^{ikz}}_{p_i}) e^{i\Omega t}. \tag{2.67}$$

Now the impedance becomes:

$$Z = \frac{p}{v} = \rho c \frac{1+r}{1-r}. \tag{2.68}$$

When the impedance is known the absorption and the reflection coefficient can be determined from:

$$r = \frac{\frac{Z}{\rho c} - 1}{\frac{Z}{\rho c} + 1} \qquad \alpha = 1 - |r|^2 = \frac{4Re\left(\frac{Z}{\rho c}\right)}{\left[Re\left(\frac{Z}{\rho c}\right) + 1\right]^2 + \left[Im\left(\frac{Z}{\rho c}\right)\right]^2}. \tag{2.69}$$

From the absorption coefficient it can be seen that at the totally reflecting boundary ($\alpha = 0$) the real part of the impedance vanishes, while at the totally absorbing boundary ($\alpha = 1$) the imaginary part of the impedance equals zero.

The product ρc is called the characteristic acoustic impedance and it is marked with Z_0. It is a material property and depends on the material density ρ and the speed of the longitudinal wave c. For air at the temperature of 0°C $\rho = 1.29\frac{kg}{m^3}$, $c = 331\frac{m}{s}$, the characteristic acoustic impedance $Z_0 = 428\frac{Ns}{m^3}$.

However, typically the angle between the absorber cross-section and the sound wave differs from 90° and the the sound pressure and sound velocity at the absorber surface will not be constant and therefore the impedance will also depend on the wave numbers in x and y direction, [Buchschmid and Müller 2008].

For the calculation of wave number dependent impedances of absorbers the porous foam has to be modeled. A method in which the system of coupled partial differential equations is transformed in the wave number-frequency domain in order to directly determine the

impedances that are depending on the angle of the incident waves, is described in detail in [Buchschmid 2011].

The measurement of impedances in the impedance tube is described in chapter 5. In order to obtain the wave number dependent impedance through measurements it is necessary to vary angles of the incident waves [Fuchs 2007].

In this work the influence of the absorber on the fluid is described over the normal specific acoustic impedance. The normal specific acoustic impedance Z_n, also known as boundary impedance, is defined as the ratio between the complex amplitude of surface pressure and the component of particle velocity normal to the surface and directed to the surface.

$$Z_n = \frac{p}{v_n} \tag{2.70}$$

The component of the velocity normal to the interface is marked with v_n.

The impedances of the absorbing structures that are included in the numerical model can either be measured or calculated.

3 Numerical Methods

In chapter 2 the differential equations of the fluid and the radiating structures are given. These equations can be solved either analytically or numerically. Both methods are searching for a solution that will satisfy the differential equation and fulfill the boundary conditions. An analytic solution exists only for simple geometries and boundary conditions. For more realistic systems that consist of more elements and have complex boundary conditions the adequate numerical methods need to be applied.

3.1 Finite Element Method

First numerical methods appeared at the beginning of the 20th century. The methods have been developed through years and they led to the creation of the Finite Element Method (FEM). The FEM is a numerical method that is determining an approximate solution of partial differential equations and integral equations.

In the FEM the problem domain is represented of a finite number of interconnected subdomains. The division of the domain into subdomains is known as discretization.

[Hughes 2000] states that the main components of the FEM are: the variational statement of the problem and the approximate solution of that variational equation. The approximate solution is found by using the finite element functions. It consists of pre-defined shape functions and coefficients that need to be determined. The shape functions are defined for each subdomain and they are approximating the solution within the element. The subdomains are connected by imposing the condition of the continuity of the displacements. The equilibrium of the system is obtained through the application of the Galerkin method of weighted residuals.

In this chapter a short overview of the FEM is given. More detailed descriptions of the method can be found in [Hughes 2000], [Rao 1982], [Zienkiewicz et al 2006a], [Zienkiewicz and Taylor 2006], [Zienkiewicz et al 2006b] and [Wüchner 2007]. The implementation of the

FEM in MATLAB is described for instance in [Pozrikidis 2005], [Kwon and Bang 2000] and [Kattan 2007].

3.1.1 The FEM Procedure

In [Zienkiewicz et al 2006a], [Kwon and Bang 2000] and [Rabold 2010] the basic steps in the FEM calculations are defined as follows:

- The FE Analysis starts with **the building of the model**. In this part of the analysis the geometry and materials are defined and usually some assumptions and idealization (e.g. the material can be assumed to be homogeneous and isotropic) are applied. Also, in the building of the model the discretization of the domain is performed. The model is divided into non overlapping elements. The response of each element is described through a finite number of degrees of freedom. When choosing the type of the element another idealization can be made. Even though all the structures are in reality 3-dimensional, it can often happen that the behavior or dimensions in 1 or 2 dimensions are dominant in comparison to other dimensions and therefore the structure can be modeled over 1- and 2- dimensional beam, plate and shell elements, [Rabold 2010]. The accuracy of the solution depends on the choice of the elements and on the used discretization. The accuracy of the solution can be improved by refining the mesh or by using the form functions of higher polynomial degree.

- Degrees of freedom for each node of the element need to be defined and an form function that describes the possible deformation should be chosen. **The element mass and stiffness matrices are assembled** using the weak formulation.

$$\mathbf{K}^e = \int_{\Omega^e} \nabla \mathbf{N}^T k \nabla \mathbf{N} d\Omega^e \qquad \mathbf{M}^e = \int_{\Omega^e} \mathbf{N}^T m \mathbf{N} d\Omega^e \qquad \text{with} \qquad \Omega = \bigcup_{n_{el}}^{e=1} \Omega^e \tag{3.1}$$

  The element mass and stiffness matrices are marked with $\mathbf{M}^e$ and $\mathbf{K}^e$, $\mathbf{N}$ marks the matrix that contains element shape functions, Ω is the domain of the element and system mass and stiffness characteristics are denoted with m and k.

- **The mass and stiffness matrices of the whole structure are assembled** with the help of the direct stiffness method. Since the characteristics of each element have been described in terms of its state variables (e.g. pressure, velocity, displacement) at certain discrete nodes along its edges, the assembly of element matrices into a global

matrix is based on the fact that the displacement of a node shared by two elements must be equal when considered as a part of both elements.

$$\mathbf{K} = \mathcal{A}_{e=1}^{n_{el}} \mathbf{K}^e \qquad \mathbf{M} = \mathcal{A}_{e=1}^{n_{el}} \mathbf{M}^e \tag{3.2}$$

$\mathcal{A}$ denotes the assembly operator which is giving the connection between elements local degrees and freedom and the global degrees of freedom [Hughes 2000].

- **Applying the boundary conditions** such as supports or applied loads and displacements. There are three basic categories of boundary conditions. Dirichlet boundary conditions are directly defining the state variable and they are introduced on the left-hand side of the equation of motion, e.g. (2.36). Neumann boundary conditions are defining the force variable and they are introduced on the right-hand side. The third type of boundary conditions - Robin boundary conditions, define the relation between the force and the state variable.

- **Solving the system of equations for different types of loads F.** In linear static analysis the system of equations can be solved directly. For dynamic analysis the solution can be sought in time or in frequency domain. In time domain analysis as in the non-linear problems the step-by-step method needs to be applied. In frequency domain it is necessary to find the solution for each frequency of interest.

$$\left(\mathbf{K} - \omega_n^2 \mathbf{M}\right) \mathbf{u} = \mathbf{F} \tag{3.3}$$

- Optionally **the homogeneous system of equations can be solved.** Determinating the systems eigenvalues ω_n and eigenmodes $\mathbf{\Psi}_n$.

$$\left(\mathbf{K} - \omega_n^2 \mathbf{M}\right) \mathbf{\Psi}_n = 0 \tag{3.4}$$

  This way determined eigenmodes Ψ_n can be used for performing the modal analysis on a reduced FE model like it will be shown in chapter 4.

- In **the post-processing phase** the stresses and strains on the element level are determined.

- The final step includes the **interpretation and the control of the results**.

3.1.2 The Fluid Finite Elements

As it is stated in 2.2.2 the chosen variable for the fluid in this work is pressure, therefore the Helmholtz equation will be observed in the form in which it is given in (2.23).

The shape functions in the fluid

In the scope of the FEM the pressure in the fluid is described as:

$$p = \sum_{i=1}^{n} p_i N_i = p_1 N_1(x, y, z) + p_2 N_2(x, y, z) + ... + p_n N_n(x, y, z) \tag{3.5}$$

In equation (3.5) N_i mark the shape functions and p_i the corresponding coefficients. The number n equals the number of degrees of freedom of the element.

The exactness of the FEM solution can be increased by refinement of the FE mesh (h-version of the FEM) or by increasing the polynomial degree of the shape functions (p-version of the FEM). Also a combination of these two methods, hp-FEM is possible.

In h-version the shape functions usually have a low polynomial degree l. When $l > 1$ the additional nodes are introduced between the end nodes of the elements. The shape functions have the value 1 in one node and value 0 in all the other nodes. In p-version the shape functions have higher polynomial degree and they are for example built from highly orthogonal Legendre Polynomials. Another characteristic of the p-version is that the set of shape functions of a higher polynomial degree contains the shape functions of the lower polynomial degree.

Figure 3.1 shows the examples of the shape functions of a 1-dimensional element for h- and p-version FEM for polynomial degree $l = 1, 2, 3$.

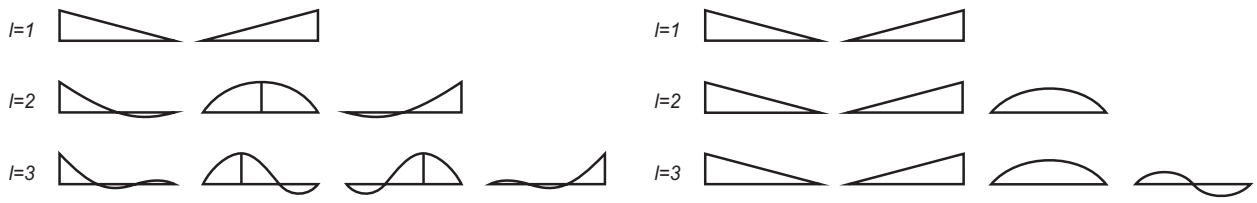

Figure 3.1: Examples for the shape functions for 1-dimensional element: h-version FEM(left) and p-version FEM (right), [Düster 2001]

Exemplarily, [Rank et al 2003] and [Dey et al 2006] have shown the advantages of the p- and hp-version of FEM, however, due to the simpler implementation, initially in this work the h-version of FEM has been used for the model reduction method that is described in chapter 4. Afterwards, some calculation examples have been performed using the Spectral Finite Element Method. This method will be described in section 3.2.

In order to guarantee that the approximate solution will converge to the exact solution with the refinement of the mesh the shape functions need to fulfill the following conditions [Hughes 2000]:

- Smoothness on element interior Ω^e,
- Continuity of primary variables of adjoint elements at the boundary Γ^e,
- Completeness.

The first two conditions are influenced by the theory that elements should represent, e.g. if the derivatives in the stiffness matrix are of order m the C^m continuity on Ω^e and the C^{m-1} continuity on Γ^e.

The third condition requires that the element shape function is able to exactly represent an arbitrary polynomial. Completeness is a property of the whole set of the shape functions for one element and not just the property of an individual shape function [Wüchner 2007].

Figure 3.2 shows a 1d fluid element of the length L and its shape functions of polynomial degree p=1. The nodes of the element are marked with i and j. The shape functions need to provide only C^0-continuity over the element boundaries because the highest derivative of the pressure in the weak formulation of the Helmholtz equation is the first derivative. The derivation of the weak formulation is given in the subsection: **The Fluid Element Matrices**.

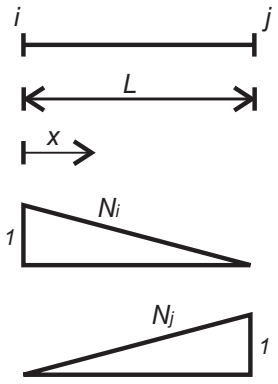

Figure 3.2: 1d fluid element with linear shape functions

The shape functions are:

$$N_i = 1 - \frac{x}{L} = 1 - \xi \qquad \text{and} \qquad N_j = \frac{x}{L} = \xi. \tag{3.6}$$

In equation (3.6) the ratio $\xi = \frac{x}{L}$ is the dimensionless (or natural) coordinate.

Isoparametric Representation

The concept of the isoparametric representation will now be explained on the example of the shape functions for 2d fluid elements.

An element of a simple geometry in parameter space (ξ, η) is chosen, see figure 3.3 (left). All the shape functions are formulated in this parameter space. Afterwards, the mapping between the parameter space and the real space is defined. Finally, the main idea of the isoparametric representation is to choose the same shape functions for interpolation of the physical quantities and geometry.

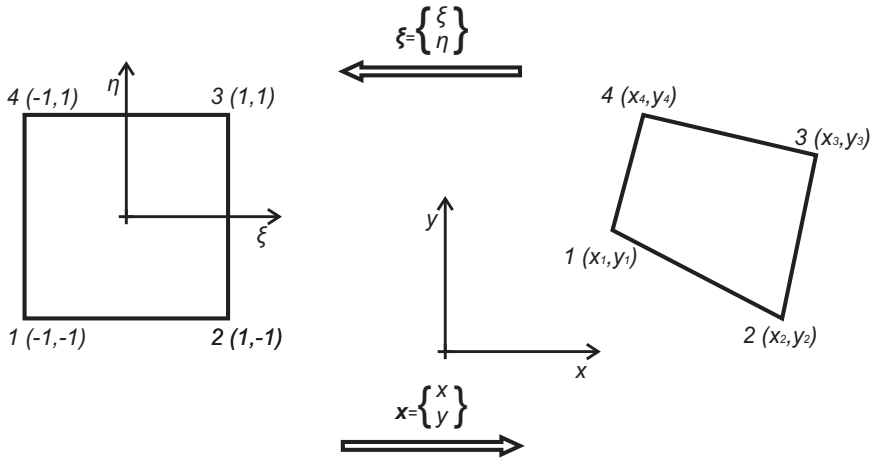

Figure 3.3: Quadrilateral domain and original coordinate system [Hughes 2000]

With help of the shape functions the mapping between the coordinates in the parameter space $\xi = \begin{Bmatrix} \xi \\ \eta \end{Bmatrix}$ and the coordinates in the real space $\mathbf{x} = \begin{Bmatrix} x \\ y \end{Bmatrix}$ is realized:

$$\begin{aligned} x(\xi, \eta) &= \sum_{a=1}^{4} N_a(\xi, \eta) x_a^e \\ y(\xi, \eta) &= \sum_{a=1}^{4} N_a(\xi, \eta) y_a^e \end{aligned} \tag{3.7}$$

The shape functions N_a are determined by supposing the bilinear expansions, [Hughes 2000]:

$$\begin{aligned} x(\xi,\eta) &= \alpha_0 + \alpha_1\xi + \alpha_2\eta + \alpha_3\xi\eta \\ y(\xi,\eta) &= \beta_0 + \beta_1\xi + \beta_2\eta + \beta_3\xi\eta \end{aligned} \tag{3.8}$$

The coefficients α and β are determined from the conditions:

$$\begin{aligned} x(\xi_a,\eta_a) &= x_a^e \\ y(\xi_a,\eta_a) &= y_a^e, \end{aligned} \tag{3.9}$$

for $a = 1, 2, 3, 4$. The shape functions are:

$$\begin{aligned} N_1^e &= \tfrac{1}{4}(1-\xi)(1-\eta), \\ N_2^e &= \tfrac{1}{4}(1+\xi)(1-\eta), \\ N_3^e &= \tfrac{1}{4}(1+\xi)(1+\eta), \\ N_4^e &= \tfrac{1}{4}(1-\xi)(1+\eta). \end{aligned} \tag{3.10}$$

An example of a bilinear shape function N_a for the node a is shown in figure 3.4. This shape is not a linear polynomial but it varies linearly along the edges of the quadrilateral element.

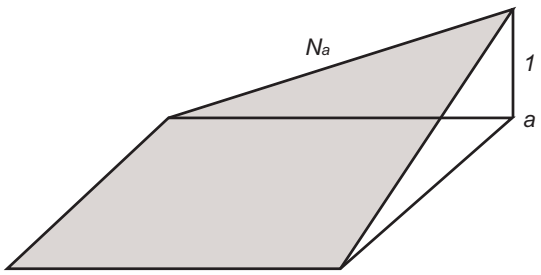

Figure 3.4: Bilinear shape function

In order to assure completeness the condition:

$$\sum_{a=1}^{4} N_a^e(\xi,\eta) = 1 \tag{3.11}$$

needs to be checked:

$$\begin{aligned} \sum_{a=1}^{4} N_a^e(\xi,\eta) &= \tfrac{1}{4}(1-\xi)(1-\eta) + \tfrac{1}{4}(1+\xi)(1-\eta) \\ &+ \tfrac{1}{4}(1+\xi)(1+\eta) + \tfrac{1}{4}(1-\xi)(1+\eta) \quad = 1. \end{aligned} \tag{3.12}$$

Consequently, the pressure in the 2d fluid is determined by using the same shape functions for each element:

$$p(\xi,\eta) = \sum_{a=1}^{4} N_a(\xi,\eta) p_a^e. \tag{3.13}$$

For numerical representation of the 2d fluid triangular elements can also be used. For 3d simulations hexahedral and tetrahedral elements will be used. The shape functions can be determined using the same procedure see equations (3.8) - (3.10).

The fluid element matrices

In the following, the weak formulation of the Helmholtz equation will be derived. Afterwards, the discretization of the problem will be performed and the expressions for the element matrices will be obtained.

The request for calculating the second derivative in the Helmholtz equation (2.23) will be weakened with help of the following integral over the problem domain Ω:

$$\int_{\Omega} \left(\Delta p w + \frac{\omega^2}{c_f^2} p w \right) d\Omega = 0, \tag{3.14}$$

where w is an arbitrary weighting function.

When the equation (3.14) is integrated by parts the weak formulation of the Helmholtz equation is obtained:

$$\int_{\Omega} \left(\frac{\omega^2}{c_f^2} w p - \nabla w \nabla p \right) d\Omega + \int_{\Gamma} w t d\Gamma = 0. \tag{3.15}$$

In equation (3.15) Γ marks the boundary of the domain Ω and t is a projection of the pressure gradient on the normal vector of the boundary.

The weak formulations in mechanics are also known as virtual work or virtual displacement principles.

The approximated solution in a domain of a single element Ω_e becomes:

$$\int_{\Omega_e} \left(\frac{\omega^2}{c_f^2} w^e p^e - \nabla w^e \nabla p^e \right) d\Omega + \int_{\Gamma^e} w^e t d\Gamma = 0. \tag{3.16}$$

When:

$$\begin{array}{rcll} p^e & = & \mathbf{Np} & \mathbf{N} = [N_1, N_2, ..., N_n] \qquad \mathbf{p} = [p_1, p_2, ..., p_n] \\ w^e & = & \mathbf{Nw} & \mathbf{w} = [w_1, w_2, ..., w_n] \end{array} \tag{3.17}$$

where $\mathbf{w}^e$ marks arbitrary constants, we obtain:

$$\int\limits_{\Omega^e} \left(\frac{\omega^2}{c_f^2} \mathbf{N}^T \mathbf{N} \mathbf{p} - \nabla \mathbf{N}^T \nabla \mathbf{N} \mathbf{p} \right) d\Omega + \int\limits_{\Gamma^e} \mathbf{N} t d\Gamma = 0. \tag{3.18}$$

From equation (3.18) we yield in the matrix vector formulation written as:

$$\left[\mathbf{K}^e - \omega^2 \mathbf{M}^e \right] \mathbf{p} = \mathbf{F}^e \tag{3.19}$$

were $\mathbf{K}^e$ and $\mathbf{M}^e$ stand for elements stiffness and mass matrix while $\mathbf{F}^e$ marks the load vector that is acting on the element boundaries.

$$\begin{array}{rcl} \mathbf{K}^e & = & \int\limits_{\Omega^e} \nabla \mathbf{N}^T \nabla \mathbf{N} d\Omega^e \\ \mathbf{M}^e & = & \frac{1}{c^2} \int\limits_{\Omega^e} \mathbf{N}^T \mathbf{N} d\Omega^e \\ \mathbf{F}^e & = & \int\limits_{\Gamma^e} \mathbf{N} t d\Gamma^e \end{array} \tag{3.20}$$

The element mass and stiffness matrices are symmetric, banded and positive-definite which allows very efficient computer solution of the problem (3.19).

For calculating the element stiffness matrix it is necessary to determine the partial derivatives of the shape functions in the global coordinate system. These derivatives are determined with the help of the partial derivatives in the local coordinate system. Exemplarily derivatives of the shape functions for a 2d fluid element are given:

$$\begin{bmatrix} \frac{\partial N_i}{\partial \xi} \\ \frac{\partial N_i}{\partial \eta} \end{bmatrix} = \begin{bmatrix} \frac{\partial x}{\partial \xi} & \frac{\partial y}{\partial \xi} \\ \frac{\partial x}{\partial \eta} & \frac{\partial y}{\partial \eta} \end{bmatrix} \begin{bmatrix} \frac{\partial N_i}{\partial x} \\ \frac{\partial N_i}{\partial y} \end{bmatrix} \tag{3.21}$$

The matrix of derivatives of the vector of global coordinates with respect to the vector of local coordinates is called the Jacobian matrix and is marked with $\mathbf{J}$:

$$\mathbf{J} = \frac{\partial (x, y)}{\partial (\xi, \eta)} = \begin{bmatrix} \frac{\partial x}{\partial \xi} & \frac{\partial y}{\partial \xi} \\ \frac{\partial x}{\partial \eta} & \frac{\partial y}{\partial \eta} \end{bmatrix}. \tag{3.22}$$

By inverting the Jacobian matrix the derivatives of the shape functions in the global coordinate system can be determined:

$$\begin{bmatrix} \frac{\partial N_i}{\partial x} \\ \frac{\partial N_i}{\partial y} \end{bmatrix} = \mathbf{J}^{-1} \begin{bmatrix} \frac{\partial N_i}{\partial \xi} \\ \frac{\partial N_i}{\partial \eta} \end{bmatrix}. \tag{3.23}$$

The integration that is performed in order to determine the elements matrices and vectors also requires the transformation from the local to the global coordinate system, [Rabold 2010]. For an arbitrary function $q(\xi, \eta)$ over the surface A the transformation is defined as:

$$\int_A q(x,y)dA = \int_x \int_y q(\xi,\eta)dxdy = \int_{-1}^{+1} \int_{-1}^{+1} q(\xi,\eta)\,|\mathbf{J}|\,d\xi d\eta \tag{3.24}$$

where $|\mathbf{J}|$ marks the determinant of the Jacobian matrix.

These integrals are solved numerically by applying quadrature rules. For example, the Gaussian quadrature rule approximates a definite integral with a weighted sum of the values of the function (w_i, w_j) in certain points (ξ_i, η_j) inside of the integration domain:

$$\int_{-1}^{+1} \int_{-1}^{+1} q(\xi,\eta)\,|\mathbf{J}|\,d\xi d\eta \approx \sum_{i=1}^{n_i} \sum_{j=1}^{n_j} w_i w_j q(\xi_i,\eta_j)\,|\mathbf{J}| \tag{3.25}$$

In equation (3.25) n_i and n_j mark the number of Gauss points in ξ and η directions. When the same shape functions are used in both directions $n_i = n_j$.

3.1.3 The Structure Finite Elements

In this chapter exemplary, the finite elements for a beam structures will be presented. A remark can be made that in case of plane waves in an infinitely large plate the plate can be approximated with a beam in the direction perpendicular to the wave front, see chapter 2.2.2.

The principle of virtual work gives the equilibrium condition that the sum of the virtual work of internal forces and the virtual work of the external forces equals zero:

$$\delta W_{int} + \delta W_{ext} = 0. \tag{3.26}$$

A simple supported beam is shown in figure 3.5. Continuously distributed load q and moments m as well as the concentrated force Q_0 and moment M_0 are acting on the beam.

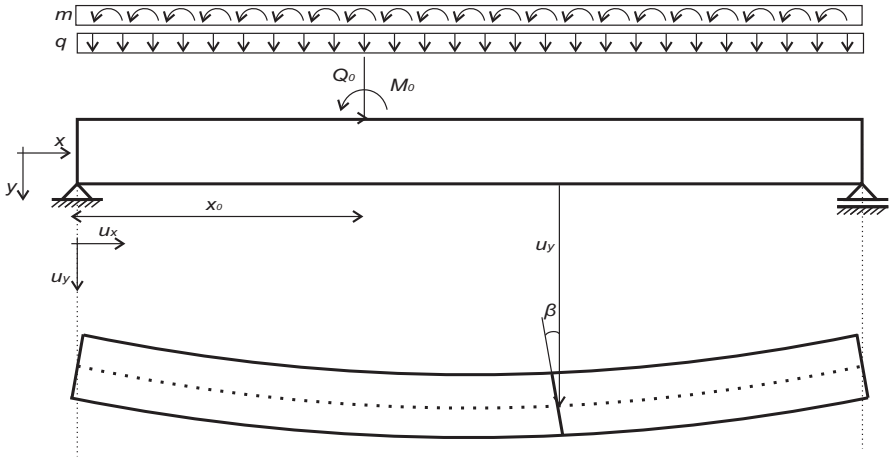

Figure 3.5: Simple beam exposed to distributed and concentrated forces and moments, compare to [Wüchner 2007]

The angle between the cross section of the beam in undeformed and deformed configuration is marked with β. This angle consist of two parts:

$$\beta = \gamma + \frac{du_y}{dx} \tag{3.27}$$

where γ marks the transverse strains.

The virtual work of the internal forces is:

$$\delta W_{int} = \int_0^L (M_z \delta\kappa + Q\delta\gamma) dx. \tag{3.28}$$

The Euler-Bernoulli beam theory assumes that $\gamma = 0$ and therefore the virtual work of internal forces equals:

$$\delta W_{int} = \int_0^L M_z \delta\kappa dx = \int_0^L EI\kappa\delta\kappa dx = \int_0^L EI \frac{\partial^2 u_y}{\partial x^2} \delta \frac{\partial^2 u_y}{\partial x^2} dx \tag{3.29}$$

where M_z marks the bending moment, κ the curvature, E the Young's modulus and I is moment of inertia of the beam.

The virtual work of the external forces, when δw and $\delta\beta$ comply with boundary conditions given in figure 3.5 is:

$$\delta W_{ext} = \int_0^L (q\delta w + m\delta\beta)dx + Q_0\delta u_0 + M_0\delta\beta_0. \tag{3.30}$$

When equations (3.29) and (3.30) are introduced in (3.26) the weak formulation of the differential equation of the beam is obtained.

The virtual work of internal forces of the beam includes second derivatives of displacement u, hence the variational index equals 2. The highest derivative of the displacement imposes the condition of the C^1 continuity, which means that the shape functions need to be continuous and have continuous first derivatives.

The shape functions in the structure

The Hermitian cubic shape functions are the simplest shape functions that can satisfy the condition of the C^1 continuity across the elements boundaries.

The structural elements require additional nodal degrees of freedom in form of displacement derivatives (nodal rotations). The nodal rotations are marked with φ. The interpolation function of the displacements along the beam element in dependence of the nodal degrees of freedom is defined as follows:

$$u^e = \begin{bmatrix} N_{ui} & N_{\varphi i} & N_{uj} & N_{\varphi j} \end{bmatrix} \begin{bmatrix} u_i \\ \varphi_i \\ u_j \\ \varphi_j \end{bmatrix} = \mathbf{Nu}. \tag{3.31}$$

The Hermitian shape functions are:

$$\begin{aligned} N^e_{ui}(x) &= \tfrac{1}{4}(1-\xi)^2(2+\xi) \\ N^e_{\varphi i}(x) &= \tfrac{1}{8}L(1-\xi)^2(1+\xi) \\ N^e_{uj}(x) &= \tfrac{1}{4}(1+\xi)^2(2-\xi) \\ N^e_{\varphi j}(x) &= -\tfrac{1}{8}L(1+\xi)^2(1-\xi) \end{aligned} \tag{3.32}$$

where ξ is the dimensionless natural coordinate $\xi = \frac{2x}{L} - 1$.

The shape functions are sketched in figure 3.6.

For the structural elements in 2d the trilateral and quadrilateral elements were used and the shape functions also needed to fulfill the C^1 continuity condition.

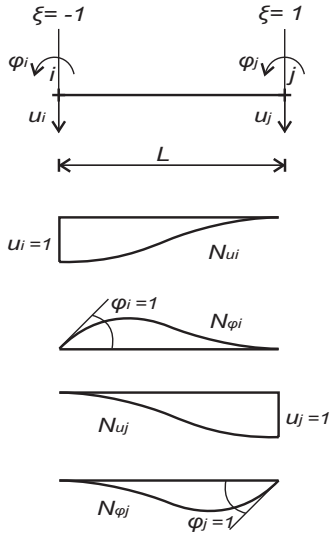

Figure 3.6: Hermitian shape functions, [Wüchner 2007]

The structure element matrices

The equation of motion of a beam (2.37) in a discretized form becomes

$$\left[\mathbf{K}^e - \omega^2 \mathbf{M}^e\right] \mathbf{u_y} = \mathbf{F}^e \tag{3.33}$$

were $\mathbf{K}^e$ and $\mathbf{M}^e$ stand for elements stiffness and mass matrix while $\mathbf{F}^e$ marks the force vector that is acting on the element and $\mathbf{u}_y$ are the displacements in y direction. These matrices are calculated similarly to the fluid element matrices (3.20):

$$\begin{aligned} \mathbf{K}^e &= \int_{\Omega^e} EI \mathbf{B}^T \mathbf{B} d\Omega^e \\ \mathbf{M}^e &= \int_{\Omega^e} \rho_s \mathbf{N}^T \mathbf{N} d\Omega^e \\ \mathbf{F}^e &= \int_{\Gamma^e} \mathbf{N}\mathbf{t} d\Gamma^e - \int_{\Omega^e} \mathbf{N}\mathbf{f} d\Omega^e. \end{aligned} \tag{3.34}$$

In equation (3.34) $\mathbf{B}$ marks the matrix that contains the second derivatives of the shape functions $\mathbf{N}$, $\mathbf{f}$ is the vector of external loading and $\mathbf{t}$ marks the vector of prescribed boundary conditions.

3.1.4 The Fluid-Structure Coupling Finite Elements

For determining the FE formulation of the system that consist of a fluid and a structure the equations of motion of both components need to be observed, see equation (3.19) and (3.33), and the boundary conditions (2.49) and (2.50) should be introduced.

The equations (3.19) and (3.33) can be rewritten as:

$$\begin{aligned} [\mathbf{K}_f - \omega^2 \mathbf{M}_f]\,\mathbf{p} &= \mathbf{F}_f + \mathbf{F}_u \\ [\mathbf{K}_s - \omega^2 \mathbf{M}_s]\,\mathbf{u}_y &= \mathbf{F}_s + \mathbf{F}_p \end{aligned} \tag{3.35}$$

The load that is acting on the fluid can be separated into the load caused by the accelerations of the structure at the fluid-structure interface $\mathbf{F}_u$ and the external load that is acting on the other fluid boundaries $\mathbf{F}_f$. Furthermore, the load that is acting on the structure can be divided into the external load applied on the structure $\mathbf{F}_s$ and the load due to the fluid pressure acting on the fluid-structure interface $\mathbf{F}_p$.

The fluid and the structure are discretized like it is given in (3.17) and (3.31). The interpolation functions in the fluid are marked with $\mathbf{N}_f$, $\mathbf{N}_s$ denote the interpolation functions in the structure.

Figure 3.7 shows the fluid-structure interface where element ij is a 1d structure element with the degrees of freedom: u_i, φ_i, u_j and φ_j , while element $ijkl$ is a 2d fluid element with the degrees of freedom: p_i and p_j at the interface ij.

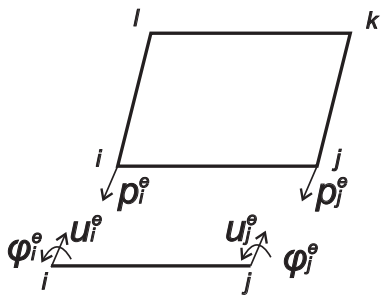

Figure 3.7: A 2d fluid FE coupled with a 1d structure element

The interface forces are calculated as follows, [Bhattacharyya and Premkumar 2003]:

$$\begin{aligned} \mathbf{F}_p &= \sum_e \int_{S_l} \mathbf{N}_s^{eT} \mathbf{n} \mathbf{p} dS = \sum_e \left(\int_{S_l} \mathbf{N}_s^{eT} \mathbf{n} \mathbf{N}_f^e dS \right) \mathbf{p}^e \\ \mathbf{F}_u &= \sum_e \int_{S_l} \mathbf{N}_f^{eT} \mathbf{n} \mathbf{p} dS = \sum_e \left(-\rho_f \int_{S_l} \mathbf{N}_f^{eT} \mathbf{n} \mathbf{N}_s^e dS \right) \ddot{\mathbf{u}}^e \end{aligned} \tag{3.36}$$

with $\mathbf{p}^e = [p_i^e \quad p_j^e]^T$ and $\ddot{\mathbf{u}}^e = [\ddot{u}_i^e \quad \ddot{u}_j^e]^T$.

In equation (3.36) $\mathbf{n}$ is the outward normal vector at the fluid-structure interface S_l.

After introducing (3.36) in (3.35) we obtain:

$$\begin{aligned} \left[\mathbf{K}_f - \omega^2 \mathbf{M}_f\right] \mathbf{p} &= \mathbf{F}_f + \sum_e \left(-\rho_f \int_{S_l} \mathbf{N}_f^{eT} \mathbf{n} \mathbf{N}_s^e dS \right) \ddot{\mathbf{u}}^e \\ \left[\mathbf{K}_s - \omega^2 \mathbf{M}_s\right] \mathbf{u}_y &= \mathbf{F}_s + \sum_e \left(\int_{S_l} \mathbf{N}_s^{eT} \mathbf{n} \mathbf{N}_f^e dS \right) \mathbf{p}^e \end{aligned} \tag{3.37}$$

The equation of motion of the coupled system can now be written as:

$$\begin{bmatrix} \mathbf{M}_s & \mathbf{0} \\ \mathbf{M}_{sf} & \mathbf{M}_f \end{bmatrix} \begin{bmatrix} \ddot{\mathbf{u}} \\ \ddot{\mathbf{p}} \end{bmatrix} + \begin{bmatrix} \mathbf{K}_s & \mathbf{K}_{sf} \\ \mathbf{0} & \mathbf{K}_f \end{bmatrix} \begin{bmatrix} \mathbf{u} \\ \mathbf{p} \end{bmatrix} = \begin{bmatrix} \mathbf{f}_s \\ \mathbf{f}_f \end{bmatrix}. \tag{3.38}$$

The asymmetric terms in the mass and the stiffness matrix of the coupled system result from the interface forces and they are determined as:

$$\begin{aligned} \mathbf{K}_{sf} &= \sum_e \left(\int_{S_l} \mathbf{N}_s^{eT} \mathbf{n} \mathbf{N}_f^e dS \right) \\ \mathbf{M}_{sf} &= \sum_e \left(-\rho_f \int_{S_l} \mathbf{N}_f^{eT} \mathbf{n} \mathbf{N}_s^e dS \right) \end{aligned} \tag{3.39}$$

3.2 Spectral Finite Element Method

The Spectral Finite Element Method (SFEM) is a class of the Finite Element Methods also known as hp-FEM. In SFEM the exponential convergence rate is achieved by refining the element mesh (h-refinement) and by increasing the polynomial degree of the shape functions (p-refinement).

SFEM are especially convenient for acoustical simulations because their shape can nicely describe smooth, wave-like patterns that correspond to e.g. pressure distribution in a room. Moreover, in order to achieve the same exactness of the solution SFEM involve less DOFs compared to h-version of FEM, [Pospiech 2010].

The shape functions in SFEM

The basis functions for the SFEM on the reference interval [-1,1] are obtained from the modal C^0 continuous expansion of the Legendre polynomials from degree 1 to P, [Pospiech et al 2009] [Buchschmid et al 2010]:

$$N_l(\xi) = \begin{cases} \frac{1-\xi}{2}, & l = 0, \\ (\frac{1-\xi}{2})(\frac{1+\xi}{2})J_{l-1}^{1,1}(\xi), & 0 < l < P, \\ \frac{1+\xi}{2}, & l = P\,. \end{cases} \tag{3.40}$$

In (3.40) $J_{l-1}^{1,1}$ marks the Jacobi polynomial of polynomial degree l and parameters $\alpha = 1$, $\beta = 1$.

The shape functions for 2- and 3-dimensional domains are obtained with the help of tensor products, e.g. for a 2d reference element shown on the left side of figure 3.3 the shape functions N_{lm} are:

$$N_{lm}(\xi, \eta) = N_l(\xi)N_m(\eta), \tag{3.41}$$

with $0 \leq l, m \leq P$ and $(\xi, \eta) \in [-1, 1]$.
For integration inside of each element the Gauss-Lobatto-Legendre quadrature is applied. The quadrature points ξ_j and the weights $w_j^{0,0}$ are defined as [Pospiech 2010]:

$$\xi_j = \begin{cases} -1, & j = 1, \\ \xi_{j-2,Q-2}^{1,1}, & j = 2, ..., Q-1, \\ 1, & j = Q, \end{cases} \tag{3.42}$$

$$w_j^{0,0} = \frac{2}{Q(Q-1)\left(J_{j-2}^{0,0}(\xi_j)\right)^2}\,, \qquad j = 1, ..., Q\,.$$

The quadrature points $\xi^{1,1}_{j-2,Q-2}$ are the zeros of the $(Q-2)$ Jacobi polynomial $J^{1,1}_{Q-2}$. The number of quadrature points Q has to be chosen so that $Q = P + 2$.

The differentiation matrix $\mathbf{B}$, with respect to the previously defined quadrature points is defined by:

$$\mathbf{B}_{ij} = \begin{cases} -\frac{Q(Q-1)}{4}, & i = j = 1, \\ \frac{J^{1,1}_{Q-1}(\xi_i)}{(\xi_i - \xi_j)\, J^{1,1}_{Q-1}(\xi_j)}, & i \neq j,\ 1 \leq i, j \leq Q, \\ 0, & 2 \leq i = j \leq Q-1, \\ \frac{Q(Q-1)}{4}, & i = j = Q\,. \end{cases} \tag{3.43}$$

4 Component Mode Synthesis

4.1 Overview

The need for analyzing complex structural systems has led to the development of the Finite Element Method (FEM). Parallel to the development of the FEM the urge for reducing the size of FE model for dynamic analysis arose in order to reduce the necessary computation time and computer storage. The FE model is usually built for the static analysis and therefore it consists from a very detailed set of grid points which is necessary for the description of internal stresses and strains. Hence, it is often infeasible to perform dynamic analysis on the FE model of the whole structure.

Section 4.2 gives an overview of the development of the Component Mode Synthesis (CMS) and the relevant literature. Furthermore, the main steps of the CMS technique as well as the advantages of this method are pointed out.

Section 4.3 gives a detailed description of the traditional Craig-Bampton method and the basic terms used in this method: component modes, transformation matrix, constraint and attachment modes. This section also introduces an improvement of the Craig-Bampton method that has been developed in this thesis. Finally, simulation results which show the advantages of this newly developed approach are given.

Section 4.4 shows the application of Craig-Bampton method in modal analysis. A possible error that can appear due to modal truncation is emphasised and a method for reducing that error is given.

The last section of this chapter (section 4.5) shows how the new approach that has been developed in 4.3 can be applied in FSI problems. Additionally, results of several simulations are presented.

4.2 Development of the Component Mode Synthesis Method

The CMS, initiated by Hurty in [Hurty 1965] quickly became a very popular model reduction technique. The basic idea is to divide the structure into a set of substructures, perform analysis on the substructure level and represent the substructures with generalized coordinates in the full system assembly.

The term component modes denotes a group of assumed modes (Ritz vectors), that are used as basis vectors for transformation from the degrees of freedom (DOFs) of a substructure to the generalized coordinates. This group of assumed vectors is arranged to form the transformation matrix.

Exemplarily in scope of the CMS an elastically supported beam can be described through normal modes Ψ_n, which are in figure 4.1 shown with rigid boundary conditions, and constraint modes Ψ_c, which introduce the elastic supports in example in figure 4.1. Therefore the displacements of the beam $u(x)$ can be calculated as:

$$u(x) = \sum_n a_n \Psi_n + \sum_c b_c \Psi_c \tag{4.1}$$

The modal coefficients a_n and b_c will be referred to as generalized coordinates.

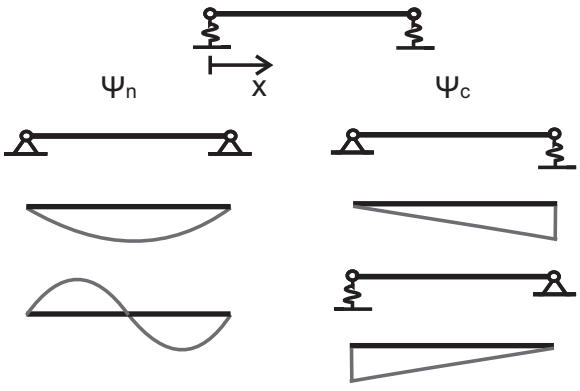

Figure 4.1: Elastically supported beam can be described with a group assumed modes (Ritz vectors)

Various types of component modes were included in the transformation matrix through the development of the CMS. Theses modes are sketched in figure 4.2. With the dashed line in figure 4.2 the interface that connects the substructure with other parts of the structure is marked. The thicker line in figure 4.2 marks the original domain and boundary conditions

and the thinner line presents a possible mode shape. In Hurty's method the transformation matrix included rigid body modes, fixed-interface normal modes and constraint modes ([Hurty 1967] and [Collins et al 1972]). Rigid body modes exist if a substructure can move without a deformation, see figure 4.2 *c*). Fixed-interfaces normal modes are obtained as a solution of the eigenvalue problem when the DOFs at the interfaces between the substructures are totally constrained, see figure 4.2 *a*). The CMS formulations that use fixed-interface normal modes are also known as fixed-interface methods.

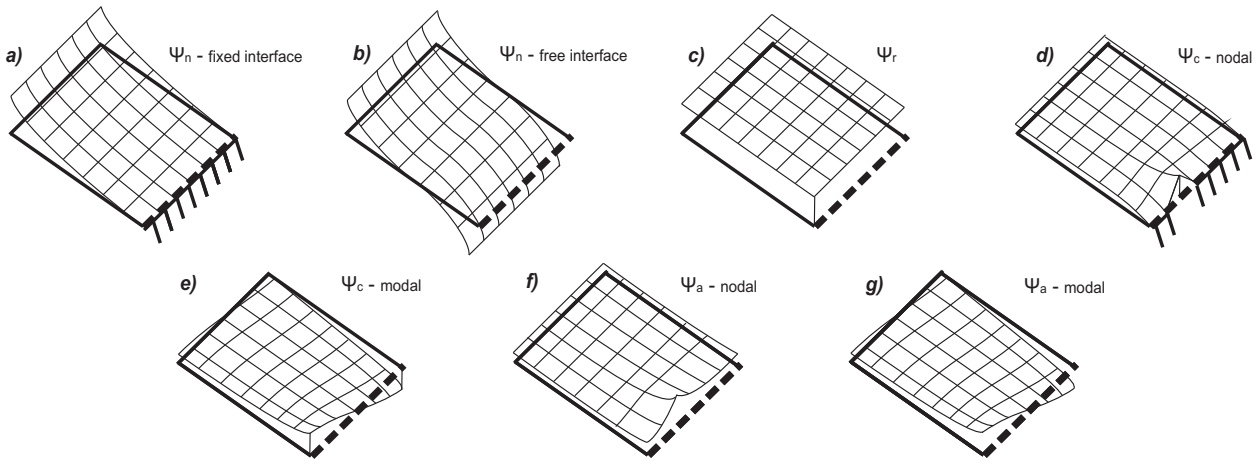

Figure 4.2: a) Interface (dashed line) with fixed DOFs, b) Interface with free DOFs, c) Rigid-body modes d) Nodal constraint modes and e) modal constraint modes f) Nodal attachment modes g) Modal attachment modes

Through different stages of development of the CMS method also a free-interface method [Shyu et al 1997] , a hybrid method (combination of fixed and free interface DOFs in normal modes) ([Jezequel 1985] and [Tran 2001]) and loaded interface method [Gladwell 1964] were used. The free-interface method introduced by Goldman [Goldman 1969] uses only rigid-body modes and free-interface normal modes. The free-interface normal modes are the solution of the eigenvalue problem when the interface DOFs are completely free, see figure 4.2 *b*). The advantage of this method is that it denies the need for calculation of constraint modes and in specific vibration cases can give satisfying results [Goldman 1969]. In general vibration problems it suffers from weak convergence and can cause significant errors. In the hybrid method the normal modes used to describe the component are calculated for a case when some nodes are free and some nodes are fixed. Statically determined deflection influence coefficients may be used to improve the accuracy of the solution. The hybrid method has improved exactness compared to the free-interface method but requires a more complex implementation than the fixed-interface method. The loaded interface method gives the most accurate results but also requires a much more complex implementation in comparison

to the fixed-interface method [Curnier 1983].

In [Craig and Bampton 1968], [Craig 1981] and [Craig 2000] Craig and Bampton slightly modified Hurty's method by using only normal and constraint modes as they considered rigid-body modes to be a special case of constraint modes. This method is the most frequently used CMS and it is known as Craig-Bampton method. In the Craig-Bampton method the constraint modes are calculated by assigning the unit displacement to the each interface DOFs, see figure 4.2 *c*). The use of attachment modes and load-dependent modes is described in [Craig 1995] and [Abdallah 1990]. The constraint and the attachment modes are the modes that allow the mobility of the interface.

An idea for reducing the number of necessary constraint and attachment modes in fixed-interface method was introduced in [Chan 2006] and [Sremcevic et al 2009a]. In these works the constraint and attachment modes were calculated by assigning a certain pattern to the whole interface simultaneously, see figure 4.2 *d*). Chan used this concept for the problem of Fluid-Structure Interaction (FSI) where the vibrating structure was placed at the boundary of the fluid. For this dissertation the method has been extended for FSI problems in which the vibrating structure is inside the fluid. It has also been broadened to tackle the problems of assembling any user-defined number of fluid substructures. Furthermore, the criteria for choosing the constraint and attachment modes are defined. The method developed in this thesis is named *MCM approach* (MCM stands for Modal Component Modes).

A short overview of CMS methods is given in figure 4.3.

	Rigid-body modes Figure 4.2 c)	Fixed-interface normal modes Figure 4.2 a)	Free-interface normal modes Figure 4.2 b)	Nodal constraint modes Figure 4.2 d)	Nodal attachment modes Figure 4.2 f)	Modal constraint or attachment modes Figure 4.2 e) & g)
Hurty's method	x	x		x		
Free-interface method	x		x			
Hybrid method			x			
Loaded interface method			x		x	
Craig-Bampton method		x		x		
MCM - approach		x				x

Figure 4.3: Modes used in different CMS methods

Additionally, according to [Yin et al 1991] and [Aoyama and Yagawa 2001], the Craig-

Bampton method has only been used for connecting several substructures where different interfaces do not have a common point, see figure 4.4 a). In this work the method has been adapted to solve problems in which several interfaces meet in a common point, or have a common edge in a 3d case, figure 4.4 b).

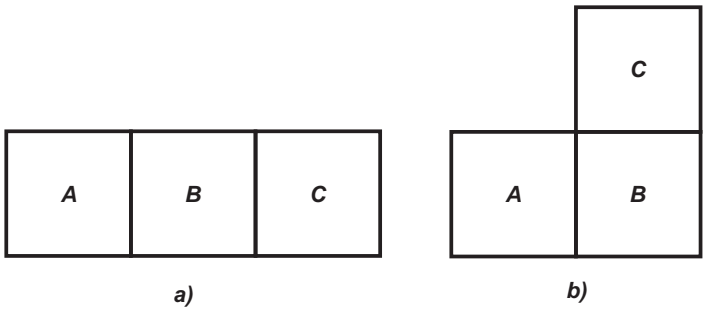

Figure 4.4: a) Typical configuration solved in [Yin et al 1991] and [Aoyama and Yagawa 2001]
b) Configuration solved in this dissertation

According to [Qu 2004] and [Suarez and Singh 1992] the CMS technique includes four major steps :

- The partition of the whole system into subsystems, see figure 4.5. It is usually led by different functions or different geometrical and dynamic characteristics of the subsystems;

- The FEM is used to form the discrete model of each subsystem. The physical DOFs of the subsystems are substituted by a reduced set of generalized coordinates. The transformation from DOF to generalized coordinates is done through a transformation matrix that consists of component modes;

- While assembling the global structure, each substructure is represented by a set of basis vectors (Ritz vectors), where the number of vectors that are taken into account is significantly smaller than the number of DOFs inside each related substructure. The assembling of the structure is based on the fulfillment of the compatibility and equilibrium conditions [Reyonso 1985];

- The resulting reduced-size model of the global system is used for all the analysis of the system. To compute the responses in physical DOFs it is necessary to use the back transformation.

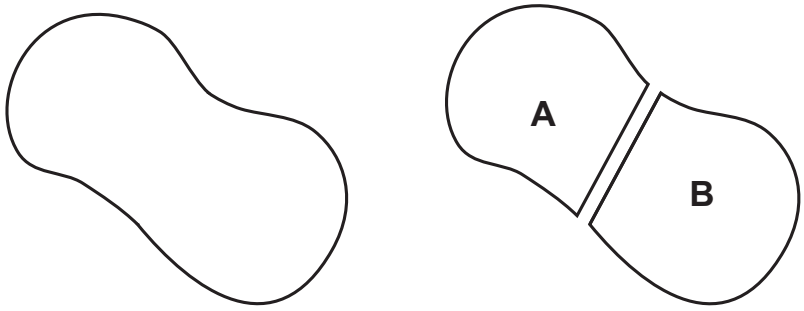

Figure 4.5: Initial structure (left) and two substructures (right)

The advantages of CMS are:

- The computational effort and computer memory usage are evidentiary saved by dividing a large dynamic problem into several smaller dynamic problems and by representing each subproblem with reduced number of DOFs;
- Independent analysis and design of different substructures. This property is very important when a structure consists of the components that are produced by different expert groups;
- The calculation effort is remarkably reduced if the structure can be divided in identical substructures;
- The characterization of the different substructures can be done in different manners, so implementation of both analytical and experimental data is possible. This property is also referred as hybrid modeling scheme;
- The changes on the structure can be easier performed while the change will be done only on the substructure level without affecting the other substructures. This property makes the optimization process much faster and cheaper.

4.3 Craig-Bampton Method

As mentioned in section 4.2 the Craig-Bampton method is nowadays one of the most often used variants of the CMS method. The method is described for a structure that is shown in figure 4.5 which consists of two substructures A and B.

The equation of motion for a single undamped component in time domain can be written in the following form:

$$\mathbf{M} \cdot \ddot{\mathbf{u}}(t) + \mathbf{K} \cdot \mathbf{u}(t) = \mathbf{f}(t). \tag{4.2}$$

In equations (4.2) $\mathbf{M}$ denotes the mass matrix of one substructure, $\mathbf{K}$ its stiffness matrix, $\mathbf{u}$ the vector of DOFs, $\mathbf{f}(t)$ is an external loading that is acting on the substructure.

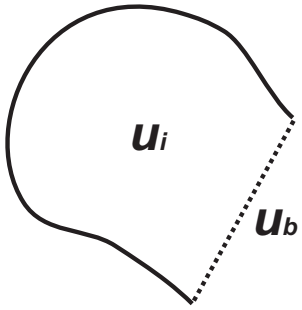

Figure 4.6: Internal $\mathbf{u_i}$ and boundary $\mathbf{u_b}$ DOFs of the substructure A

The set of all physical DOFs of one substructure can be divided into a set of boundary DOFs $\mathbf{u_b}$ and a set of internal DOFs $\mathbf{u_i}$. The boundary DOFs are at the position where the substructures are connected, the dotted line in figure 4.6. Now equation (4.2) becomes:

$$\begin{bmatrix} \mathbf{M}_{ii} & \mathbf{M}_{ib} \\ \mathbf{M}_{bi} & \mathbf{M}_{bb} \end{bmatrix} \begin{bmatrix} \ddot{\mathbf{u}}_i \\ \ddot{\mathbf{u}}_b \end{bmatrix} + \begin{bmatrix} \mathbf{K}_{ii} & \mathbf{K}_{ib} \\ \mathbf{K}_{bi} & \mathbf{K}_{bb} \end{bmatrix} \begin{bmatrix} \mathbf{u}_i \\ \mathbf{u}_b \end{bmatrix} = \begin{bmatrix} \mathbf{f}_i \\ \mathbf{f}_b \end{bmatrix} \tag{4.3}$$

The total number of DOFs of the system N is a sum of internal N_i and boundary N_b DOFs.

$$N = N_i + N_b \tag{4.4}$$

In order to reduce the number of unknowns the physical DOFs $\mathbf{u}$ will be substituted with generalized coordinates $\mathbf{g}$. The transformation is performed with the help of the transformation matrix $\mathbf{T}_{CB}$, [Sellgren 2003]:

$$\mathbf{u}(t) = \mathbf{T}_{CB} \cdot \mathbf{g}(t) \qquad \text{and} \qquad \ddot{\mathbf{u}}(t) = \mathbf{T}_{CB} \cdot \ddot{\mathbf{g}}(t). \tag{4.5}$$

The generalized coordinates are the modal coefficients of the generalized shape functions that are used for approximating the substructure. The set of generalized coordinates is truncated by neglecting the higher oscillation modes if their contribution to the total response on a low frequency excitation is small. The rule that defines the approximate cut-off frequency for modal truncation states that the eigenvalue of the last kept mode should be 1,5 times higher than the highest frequency of interest for analysis of the full structure or 1,5 times higher than the excitation frequency [Young 2000]. In the case when the kept modes do not give a

precise spatial description of the load (e.g. point loads have significant modal contributions of higher eigenmodes), additional modes need to be introduced like it will be described in the chapter 4.4.3.

By introducing equation (4.5) in (4.2) we obtain:

$$\mathbf{M} \cdot \mathbf{T}_{CB} \cdot \ddot{\mathbf{g}}(t) + \mathbf{K} \cdot \mathbf{T}_{CB} \cdot \mathbf{g}(t) = \mathbf{f}(t). \tag{4.6}$$

The influence of the other substructures $\mathbf{f_b}$ can also be introduced over the transformation matrix $\mathbf{T}_{CB}$ in the procedure that will be explained in section 4.3.1. In this work the response of the structure on a time harmonic loading is determined. If the spatial distribution of the load is time invariant we assume that the harmonic loading $\mathbf{f}(t)$ can be described as a product of spatial part $\mathbf{f}_0$ (steady-state solution) and a time varying part $f_t = e^{i\Omega t}$, where Ω marks the frequency of the harmonic excitation.

$$\mathbf{f}(x, y, z, t) = \mathbf{f}_0(x, y, z) \cdot e^{i\Omega t} \tag{4.7}$$

After multiplying the equation (4.6) with the matrix $\mathbf{T}_{CB}^T$ from the left-hand side we receive:

$$\mathbf{T}_{CB}^T \cdot \mathbf{M} \cdot \mathbf{T}_{CB} \cdot \ddot{\mathbf{g}}(t) + \mathbf{T}_{CB}^T \cdot \mathbf{K} \cdot \mathbf{T}_{CB} \cdot \mathbf{g}(t) = \mathbf{T}_{CB}^T \cdot \mathbf{f}_0 \cdot e^{i\Omega t}, \tag{4.8}$$

which can also be written as:

$$\mathbf{M}_{CB}^c \cdot \ddot{\mathbf{g}}(t) + \mathbf{K}_{CB}^c \cdot \mathbf{g}(t) = \mathbf{F}_{CB} \cdot e^{i\Omega t}, \tag{4.9}$$

where

$$\mathbf{M}_{CB}^c = \mathbf{T}_{CB}^T \cdot \mathbf{M} \cdot \mathbf{T}_{CB} \qquad \mathbf{K}_{CB}^c = \mathbf{T}_{CB}^T \cdot \mathbf{K} \cdot \mathbf{T}_{CB} \qquad \mathbf{F}_{CB} = \mathbf{T}_{CB}^T \cdot \mathbf{f_0}. \tag{4.10}$$

$\mathbf{M}_{CB}^c$ and $\mathbf{K}_{CB}^c$ denote the generalized mass and stiffness matrices of a component c while $\mathbf{F}_{CB}$ is the generalized loading.

For harmonic vibrations the equation (4.9) becomes:

$$(\mathbf{K}_{CB}^c - \Omega^2 \mathbf{M}_{CB}^c) \cdot \mathbf{g}_0 e^{i\Omega t} = \mathbf{F}_{CB} e^{i\Omega t}. \tag{4.11}$$

4.3.1 Component Modes

The transformation matrix consists of component modes of the following types: rigid-body modes, normal modes, constraint modes and attachment modes.

Normal Modes

As already mentioned in section 4.2, the normal modes used Craig-Bampton method are fixed-interface normal modes, see figure 4.2 a). Therefore, the displacements of the interface u_b equal zero. Fixed-interface normal modes represent the solution of a general eigenvalue problem of the following form:

$$\left[\mathbf{K}_{ii} - \omega_n^2 \mathbf{M}_{ii}\right] \left[\mathbf{\Psi}_{in}\right] = 0. \tag{4.12}$$

Index i denotes the internal DOFs while the index n stands for the fixed-interface normal modes and related eigenvalues.

The set of normal modes for all the DOFs of the substructure, $\mathbf{\Psi}_n$, is:

$$\mathbf{\Psi}_n = \begin{bmatrix} \mathbf{\Psi}_{in} \\ \mathbf{0}_{bn} \end{bmatrix}, \tag{4.13}$$

where zero values correspond to the boundary DOFs.

The normal modes are normalized with respect to mass matrix so:

$$\mathbf{\Psi}_{in}^T \mathbf{M}_{ii} \mathbf{\Psi}_{in} = \mathbf{I}_{nn} \quad \text{and} \quad \mathbf{\Psi}_{in}^T \mathbf{K}_{ii} \mathbf{\Psi}_{in} = \mathbf{\Lambda}_{nn} = \text{diag}(\omega_n)^2. \tag{4.14}$$

$\mathbf{I}_{nn}$ is an identity matrix and ω_n marks the eigenvalues of the substructure.

The total number of normal modes equals the number of DOFs N_i. With n the reduced set of normal modes is marked.

Constraint Modes

The constraint mode is defined as static deformation of the substructure when a unit value is assigned to one boundary DOF, while the value at the other boundary nodes equals zero,

see figure 4.2 d).

$$\begin{bmatrix} \mathbf{K}_{ii} & \mathbf{K}_{ib} \\ \mathbf{K}_{bi} & \mathbf{K}_{bb} \end{bmatrix} \begin{bmatrix} \mathbf{\Psi}_{ic} \\ \mathbf{I}_{bc} \end{bmatrix} = \begin{bmatrix} \mathbf{0} \\ \mathbf{R}_{bc} \end{bmatrix} \tag{4.15}$$

Index c marks the constraint modes and $\mathbf{I}$ is a unit matrix. In Craig-Bampton method to each interface DOFs corresponds one constraint mode and therefore $b = c$. The reactions at the interface nodes are marked with the force vector $\mathbf{R}_{bc}$.

From equation (4.15) solution for constraint modes $\mathbf{\Psi}_c$ is obtained:

$$\mathbf{\Psi}_c = \begin{bmatrix} \mathbf{\Psi}_{ic} \\ \mathbf{I}_{bc} \end{bmatrix} = \begin{bmatrix} -\mathbf{K}_{ii}^{-1}\mathbf{K}_{ib} \\ \mathbf{I}_{bc} \end{bmatrix}. \tag{4.16}$$

Rigid-body Modes

When a substructure is displaceable (i. e. There are less constraints then rigid-body DOFs.) the set of the Component Modes also includes the Rigid-body Modes, see figure 4.2 c).

Rigid-body displacements are the modes in which the component is displaced without deformation, see figure 4.2 c). Within the Craig-Bampton method they are defined as a special case of constraint modes and can be determined relative to any set of boundary coordinates that can detain the rigid-body motion of the component. In this case the number of substructure's boundary DOFs N_b is divided into DOFs that restrain the rigid-body motion N_r and other the other boundary DOFs $N_{b'}$ with $N_{b'} + N_r = N_b$.

Rigid-body modes fulfill the equation:

$$\begin{bmatrix} \mathbf{K}_{ii} & \mathbf{K}_{ib'} & \mathbf{K}_{ir} \\ \mathbf{K}_{b'i} & \mathbf{K}_{b'b'} & \mathbf{K}_{b'r} \\ \mathbf{K}_{ri} & \mathbf{K}_{rb'} & \mathbf{K}_{rr} \end{bmatrix} \begin{bmatrix} \mathbf{\Psi}_{ir} \\ \mathbf{\Psi}_{b'r} \\ \mathbf{I}_{rr} \end{bmatrix} = \begin{bmatrix} \mathbf{0} \\ \mathbf{0} \\ \mathbf{0} \end{bmatrix}. \tag{4.17}$$

$\mathbf{I}_{rr}$ stands for an identity matrix whose size corresponds to the number of possible rigid-body motions.

Solving equation (4.17), we receive the solution for the matrix of rigid-body modes $\mathbf{\Psi}_r$:

$$\mathbf{\Psi}_r = \begin{bmatrix} \mathbf{\Psi}_{ir} \\ \mathbf{\Psi}_{b'r} \\ \mathbf{I}_{rr} \end{bmatrix} = \begin{bmatrix} -\begin{bmatrix} \mathbf{K}_{ii} & \mathbf{K}_{ib'} \\ \mathbf{K}_{b'i} & \mathbf{K}_{b'b'} \end{bmatrix}^{-1} \begin{bmatrix} \mathbf{K}_{ir} \\ \mathbf{K}_{b'r} \end{bmatrix} \\ \mathbf{I}_{rr} \end{bmatrix} \tag{4.18}$$

Attachment Modes

An attachment mode is defined as a static deformation of the substructure when a unit force is applied to one boundary DOF, while the remaining boundary DOFs are force-free, see figure 4.2 f).

$$\begin{bmatrix} \mathbf{K}_{ii} & \mathbf{K}_{ib} \\ \mathbf{K}_{bi} & \mathbf{K}_{bb} \end{bmatrix} \begin{bmatrix} \mathbf{\Psi}_{ia} \\ \mathbf{\Psi}_{ba} \end{bmatrix} = \begin{bmatrix} \mathbf{0} \\ \mathbf{I}_{ba} \end{bmatrix} \tag{4.19}$$

Here, index a marks the attachment modes and in the Craig-Bampton method the number of attachment modes equals the number of boundary DOFs $a = b$. Matrix $\mathbf{I}_{ba}$ is an identity matrix whose size is defined with the number of boundary DOFs.

From equation (4.19) the matrix of attachment modes $\mathbf{\Psi}_a$ is determined:

$$\mathbf{\Psi}_a = \begin{bmatrix} \mathbf{\Psi}_{ia} \\ \mathbf{\Psi}_{ba} \end{bmatrix} = \begin{bmatrix} \mathbf{K}_{ii} & \mathbf{K}_{ib} \\ \mathbf{K}_{bi} & \mathbf{K}_{bb} \end{bmatrix}^{-1} \begin{bmatrix} \mathbf{0} \\ \mathbf{I}_{ba} \end{bmatrix} = \begin{bmatrix} \mathbf{G}_{ia} \\ \mathbf{G}_{ba} \end{bmatrix}, \tag{4.20}$$

where $\mathbf{G}$ stands for the flexibility matrix.

When a substructure has rigid-body DOFs, the stiffness matrix is singular and constraints need to be added on the stiffness matrix. The attachment modes relative to the added constraints r are defined by:

$$\left[\begin{array}{cc:c} \mathbf{K}_{ii} & \mathbf{K}_{ib'} & \mathbf{K}_{ir} \\ \mathbf{K}_{b'i} & \mathbf{K}_{b'b'} & \mathbf{K}_{b'r} \\ \hdashline \mathbf{K}_{ri} & \mathbf{K}_{rb'} & \mathbf{K}_{rr} \end{array}\right] \begin{bmatrix} \mathbf{\Psi}_{ia} \\ \mathbf{\Psi}_{b'a} \\ \mathbf{0}_{ra} \end{bmatrix} = \begin{bmatrix} \mathbf{0} \\ \mathbf{I}_{b'a} \\ \mathbf{R}_{ra} \end{bmatrix}. \tag{4.21}$$

Here $\mathbf{R}_{ra}$ marks the reaction at the the position of the added constraints r.

As already defined in equation (4.20) the attachment modes are columns of the flexibility matrix:

$$\mathbf{\Psi}_a = \begin{bmatrix} \mathbf{\Psi}_{ia} \\ \mathbf{\Psi}_{b'a} \\ \mathbf{0}_{ra} \end{bmatrix} = \begin{bmatrix} \mathbf{G}_{ia} \\ \mathbf{G}_{b'a} \\ \mathbf{0}_{ra} \end{bmatrix}. \tag{4.22}$$

$\mathbf{G}_{ia}$ and $\mathbf{G}_{ba}$ are inverse matrices of the upper left part of the matrix $\mathbf{K}$ in equation (4.21).

An alternative method for determining the attachment modes for a structure with rigid-body freedom is defining inertia relief modes. The name inertia relief refers to the procedure in which the part of the load that is causing the rigid-body motion is removed from the load. The attachment modes should be orthogonal to the rigid-body modes. In [Craig 1981] an algorithm is developed in order to remove the rigid-body force from the force vector, so the

force vector is separated into two parts, one causing rigid-body motion and other causing elastic deformation.

4.3.2 Selection of the Component Modes

For the transformation from physical to generalized DOFs it is necessary to form the transformation (or component-mode) matrix. Thereby it is necessary to decide which type of modes and how many of them need to be included in the transformation matrix. In [Craig 1995] the following criteria for selection of the modes are given:

- Linear independence and completeness;
- Low computational costs for their determination and simple selection of the number of the modes;
- High accuracy of the solution obtained by using these vectors; and
- Simplicity of obtaining the system response characteristics of interest by using these vectors.

The combination of fixed-interface normal modes and complete set of constraint modes fulfills all above mentioned criteria. In specific situations it is convenient to replace the constraint modes with attachment modes, which will be described in chapter 4.3.4. If the set of constraint modes or alternatively attachment modes is not complete, the component-mode set is not statically complete and the first criteria is violated.

In the case of two substructures A and B, as presented in figure 4.5, the Craig-Bampton transformation matrix T_{CB} can be formed in the following manner, after calculating normal Ψ_n (4.12) and constraint modes Ψ_c (4.16):

$$\mathbf{T}_{CB} = \begin{bmatrix} \mathbf{\Psi}_{in}^{A} & \mathbf{\Psi}_{ic}^{A} \\ \mathbf{0} & \mathbf{I}_{bc}^{A} \end{bmatrix} \tag{4.23}$$

When the transformation is performed, the mass and stiffness matrices of the substructure A have the following form:

$$\begin{aligned} \mathbf{M}_{CB}^{A} &= \mathbf{T}_{CB}^{T}\mathbf{M}^{A}\mathbf{T}_{CB} = \begin{bmatrix} \mathbf{I}_{nn} & \mathbf{M}_{nc} \\ \mathbf{M}_{cn} & \mathbf{M}_{cc} \end{bmatrix} \\ \mathbf{K}_{CB}^{A} &= \mathbf{T}_{CB}^{T}\mathbf{K}^{A}\mathbf{T}_{CB} = \begin{bmatrix} \mathbf{\Lambda}_{nn} & \mathbf{0} \\ \mathbf{0} & \mathbf{K}_{cc} \end{bmatrix}, \end{aligned} \tag{4.24}$$

where

$$\begin{aligned} \mathbf{M}_{nc} = \mathbf{M}_{cn}^{T} &= \mathbf{\Psi}_{in}^{T}\left(\mathbf{M}_{ii}\mathbf{\Psi}_{ic} + \mathbf{M}_{ib}\right) \\ \mathbf{M}_{cc} &= \mathbf{\Psi}_{ic}^{T}\left(\mathbf{M}_{ii}\mathbf{\Psi}_{ic} + \mathbf{M}_{ib}\right) + \mathbf{M}_{bi}\mathbf{\Psi}_{ic} + \mathbf{M}_{bb} \\ \mathbf{K}_{cc} &= \mathbf{\Psi}_{ic}^{T}\left(\mathbf{K}_{ii}\mathbf{\Psi}_{ic} + \mathbf{K}_{ib}\right) + \mathbf{K}_{bi}\mathbf{\Psi}_{ic} + \mathbf{K}_{bb} \end{aligned}$$

When using nodal constraint modes $\mathbf{K}_{cc}$ becomes:

$$\mathbf{K}_{cc} = \mathbf{K}_{bb} - \mathbf{K}_{bi}\mathbf{K}_{ii}^{-1}\mathbf{K}_{ib} \qquad \text{with} \qquad \mathbf{\Psi}_{ic} = -\mathbf{K}_{ii}^{-1}\mathbf{K}_{ib}.$$

In equation (4.24) the index n marks the normal modes while index c stands for constraint modes, $\mathbf{I}_{nn}$ is an identity matrix whose size is defined by the kept number of normal modes and $\mathbf{\Lambda}_{nn} = diag(\omega_j^2)$, where ω_j marks the eigenvalues of the kept normal modes.

The transformation matrix is similar when instead of constraint modes attachment modes $\mathbf{\Psi}_a$ (4.20) are used:

$$\mathbf{T}_{CB} = \begin{bmatrix} \mathbf{\Psi}_{in}^{A} & \mathbf{\Psi}_{ia}^{A} \\ 0 & \mathbf{\Psi}_{ba}^{A} \end{bmatrix}. \tag{4.25}$$

4.3.3 System Synthesis

For simplicity the system shown in figure 4.5, which consists of two components A and B, will again be observed. Its two components have a common interface. The physical DOFs at the interface $\mathbf{u}_b$ are constrained by the following condition:

$$\mathbf{u}_b^{A} = \mathbf{u}_b^{B} \tag{4.26}$$

If no external forces are acting on the interface the interface forces $\mathbf{f}_b$ are related by:

$$\mathbf{f}_b^{A} + \mathbf{f}_b^{B} = 0 \tag{4.27}$$

to provide the equilibrium of forces in the system.

For the derivation of the system's equation of motion, the Lagrange equation with undetermined multipliers will be used, [Craig and Chang 1976]. For that we need expressions for system's kinetic and potential energy.

When:

$$\mathbf{g} = \begin{bmatrix} \mathbf{g}^A \\ \mathbf{g}^B \end{bmatrix}, \qquad \mathbf{m} = \begin{bmatrix} \mathbf{M}^A_{CB} & \mathbf{0} \\ \mathbf{0} & \mathbf{M}^B_{CB} \end{bmatrix} \qquad \text{and} \qquad \mathbf{k} = \begin{bmatrix} \mathbf{K}^A_{CB} & \mathbf{0} \\ \mathbf{0} & \mathbf{K}^B_{CB} \end{bmatrix}, \tag{4.28}$$

the kinetic energy T of the system is expressed by:

$$T = \frac{1}{2}\dot{\mathbf{g}}^T \mathbf{m} \dot{\mathbf{g}} = \frac{1}{2}\dot{\mathbf{g}}^{A^T} \mathbf{M}^A_{CB} \dot{\mathbf{g}}^A + \frac{1}{2}\dot{\mathbf{g}}^{B^T} \mathbf{M}^B_{CB} \dot{\mathbf{g}}^B \tag{4.29}$$

Here $\mathbf{g}$ are generalized coordinates defined in (4.5) while $\mathbf{M}^A_{CB}$ and $\mathbf{M}^B_{CB}$ mark the generalized mass matrices of substructures A and B and they are defined in (4.24).

The potential energy U of the system equals:

$$U = \frac{1}{2}\mathbf{g}^T \mathbf{k} \mathbf{g} = \frac{1}{2}\mathbf{g}^{A^T} \mathbf{K}^A_{CB} \mathbf{g}^A + \frac{1}{2}\mathbf{g}^{B^T} \mathbf{K}^B_{CB} \mathbf{g}^B \tag{4.30}$$

$\mathbf{K}^A_{CB}$ and $\mathbf{K}^B_{CB}$ mark the generalized stiffness matrices of substructures A and B.

The coupling conditions (4.26) and (4.27) can also be expressed in terms of generalized coordinates:

$$\mathbf{g}^A_c = \mathbf{g}^B_c \tag{4.31}$$

$$\tilde{\mathbf{f}}^A_c + \tilde{\mathbf{f}}^B_c = 0 \tag{4.32}$$

Where $\mathbf{g}^A_c$ and $\mathbf{g}^B_c$ are interface generalized coordinates of substructures A and B that corresponds to the constraint (or attachment) c modes while $\tilde{\mathbf{f}}^A_c$ and $\tilde{\mathbf{f}}^B_c$ are interface generalized forces.

The constraint equation (4.31) can be written with respect to the set of all generalized coordinates of the system $\mathbf{g}$ and combined so that the matrix constraint equation is obtained:

$$\mathbf{C}\mathbf{g} = \begin{bmatrix} \mathbf{0} & \mathbf{I} & \mathbf{0} & -\mathbf{I} \end{bmatrix} \begin{bmatrix} \mathbf{g}^A_n \\ \mathbf{g}^A_c \\ \mathbf{g}^B_n \\ \mathbf{g}^B_c \end{bmatrix} = 0 \tag{4.33}$$

It will be shown later that the force equilibrium condition (4.32) will be automatically fulfilled by introducing the displacement compatibility condition (4.31).

The Lagrange equation of the total system can now be written as:

$$L = T - U - \boldsymbol{\sigma}^T \mathbf{C}\mathbf{g} \tag{4.34}$$

where $\boldsymbol{\sigma}$ is the vector of Lagrange multipliers.

The system equation of motion is here obtained by applying the Lagrange equation in the form:

$$\frac{d}{dt}\frac{\partial L}{\partial \dot{\zeta}} - \frac{\partial L}{\partial \zeta} = \tilde{Q} \tag{4.35}$$

In equation (4.35) ζ refers to $\mathbf{g}$ or $\boldsymbol{\sigma}$ and $\tilde{Q}$ is a generalized force. For the problem of free-vibrations the generalized force is only related to the interface forces between the sub-structures.

For the problem of free-vibrations forces are inserted only at the component interface so the virtual work of the interface forces is described as follows:

$$\delta W = (\delta \mathbf{u}_b^A)^T \mathbf{f}_b^A + (\delta \mathbf{u}_b^B)^T \mathbf{f}_b^B. \tag{4.36}$$

By introducing the condition that the virtual displacements at the interface are equal $\delta \mathbf{u}_b^A = \delta \mathbf{u}_b^B$ in (4.36):

$$\delta W = (\delta \mathbf{u}_b^A)^T (\mathbf{f}_b^A + \mathbf{f}_b^B) \tag{4.37}$$

is obtained. When the force equilibrium condition (4.27) at the interface is fulfilled :

$$\delta W = 0. \tag{4.38}$$

In the case of nonconservative forces at the interface $\delta W = 0$ and $Q = 0$: When equations (4.29), (4.30) and (4.34) are introduced into (4.35) the system equation of motion becomes:

$$\mathbf{m}\ddot{\mathbf{g}} + \mathbf{k}\mathbf{g} = \mathbf{C}^T \boldsymbol{\sigma}. \tag{4.39}$$

After introducing (4.33), equation (4.39) becomes:

$$\begin{bmatrix} \mathbf{I}_{nn}^{A} & \mathbf{M}_{nc}^{A} & 0 & 0 \\ \mathbf{M}_{cn}^{A} & \mathbf{M}_{cc}^{A} & 0 & 0 \\ 0 & 0 & \mathbf{I}_{nn}^{B} & \mathbf{M}_{nc}^{B} \\ 0 & 0 & \mathbf{M}_{cn}^{B} & \mathbf{M}_{cc}^{B} \end{bmatrix} \begin{bmatrix} \ddot{\mathbf{g}}_{n}^{A} \\ \ddot{\mathbf{g}}_{c}^{A} \\ \ddot{\mathbf{g}}_{n}^{B} \\ \ddot{\mathbf{g}}_{c}^{B} \end{bmatrix} + \begin{bmatrix} \mathbf{\Lambda}_{nn}^{A} & 0 & 0 & 0 \\ 0 & \mathbf{K}_{cc}^{A} & 0 & 0 \\ 0 & 0 & \mathbf{\Lambda}_{nn}^{B} & 0 \\ 0 & 0 & 0 & \mathbf{K}_{cc}^{B} \end{bmatrix} \begin{bmatrix} \mathbf{g}_{n}^{A} \\ \mathbf{g}_{c}^{A} \\ \mathbf{g}_{n}^{B} \\ \mathbf{g}_{c}^{B} \end{bmatrix} = \begin{bmatrix} 0 \\ \boldsymbol{\sigma} \\ 0 \\ -\boldsymbol{\sigma} \end{bmatrix} \tag{4.40}$$

In reference [Craig 1981] is shown that the set of equations (4.40) and (4.33) is usually solved by using the following transformation:

$$\mathbf{g} = \mathbf{S}\mathbf{g}_{l}. \tag{4.41}$$

This transformation needs to be performed because the generalized coordinates are not independent. They are connected with the constraint (4.31). The full set of system's generalized coordinates $\mathbf{g}$ can be divided into independent generalized coordinates $\mathbf{g}_l$ and dependent generalized coordinates $\mathbf{g}_d$. The dependent generalized coordinates are those that describe the displacement of the interface because they are influenced by all adjoint substructures. The set of independent generalized coordinates is obtained with the following coordinate transformation: The coupling matrix is in equation (4.41) denoted with $\mathbf{S}$ and it is obtained from the constraint equation (4.31):

$$\begin{aligned} \mathbf{C}\mathbf{g} &= \begin{bmatrix} \mathbf{C}_{dd} & \mathbf{C}_{dl} \end{bmatrix} \begin{bmatrix} \mathbf{g}_{d} \\ \mathbf{g}_{l} \end{bmatrix} = 0 \\ \mathbf{g} &= \begin{bmatrix} \mathbf{g}_{d} \\ \mathbf{g}_{l} \end{bmatrix} = \begin{bmatrix} -\mathbf{C}_{dd}^{-1}\mathbf{C}_{dl} \\ \mathbf{I}_{ll} \end{bmatrix} \mathbf{g}_{l} = \mathbf{S}\mathbf{g}_{l} \end{aligned} \tag{4.42}$$

The structure of the component coupling matrix $\mathbf{S}$ for assembling the system that consists of two substructures A and B can be easily recognized:

$$\mathbf{g} = \begin{bmatrix} \mathbf{g}_{n}^{A} \\ \mathbf{g}_{c}^{A} \\ \mathbf{g}_{n}^{B} \\ \mathbf{g}_{c}^{B} \end{bmatrix} = \underbrace{\begin{bmatrix} \mathbf{I} & 0 & 0 \\ 0 & 0 & \mathbf{I} \\ 0 & \mathbf{I} & 0 \\ 0 & 0 & \mathbf{I} \end{bmatrix}}_{S} \begin{bmatrix} \mathbf{g}_{n}^{A} \\ \mathbf{g}_{n}^{B} \\ \mathbf{g}_{c}^{A} \end{bmatrix}. \tag{4.43}$$

After introducing the coordinate transformation (4.41) into (4.40) and multiplying the whole equation with $\mathbf{S}^T$ from the left-hand side the equation of motion for the full system is obtained

in terms of the independent coordinates $\mathbf{g}_l$:

$$\mathbf{M}_{sys}\ddot{\mathbf{g}}_l + \mathbf{K}_{sys}\mathbf{g}_l = 0. \tag{4.44}$$

$\mathbf{M}_{sys}$ and $\mathbf{K}_{sys}$ are the mass and the stiffess matrices of the total system.

$$\mathbf{M}_{sys} = \mathbf{S}^T\mathbf{m}\mathbf{S} \qquad \text{and} \qquad \mathbf{K}_{sys} = \mathbf{S}^T\mathbf{k}\mathbf{S}$$

The resulting system's mass and stiffness matrices have the following form:

$$\begin{aligned} \mathbf{M}_{sys} &= \begin{bmatrix} \mathbf{I}^A_{nn} & \mathbf{0} & \mathbf{M}^A_{nc} \\ \mathbf{0} & \mathbf{I}^B_{nn} & \mathbf{M}^B_{nc} \\ \mathbf{M}^A_{cn} & \mathbf{M}^B_{cn} & \mathbf{M}^A_{cc} + \mathbf{M}^B_{cc} \end{bmatrix}. \\ \mathbf{K}_{sys} &= \begin{bmatrix} \mathbf{\Lambda}^A_{nn} & \mathbf{0} & \mathbf{0} \\ \mathbf{0} & \mathbf{\Lambda}^B_{nn} & \mathbf{0} \\ \mathbf{0} & \mathbf{0} & \mathbf{K}^A_{cc} + \mathbf{K}^B_{cc} \end{bmatrix}. \end{aligned} \tag{4.45}$$

Now, at the end of this section it will be shown that the interface force-equilibrium condition (4.32) is also fulfilled. The equation of motion of the substructure A expressed in generalized coordinates has the following form:

$$\begin{bmatrix} \mathbf{I}^A_{nn} & \mathbf{M}^A_{nc} \\ \mathbf{M}^A_{cn} & \mathbf{M}^A_{cc} \end{bmatrix} \begin{bmatrix} \ddot{\mathbf{g}}^A_n \\ \ddot{\mathbf{g}}^A_c \end{bmatrix} + \begin{bmatrix} \mathbf{\Lambda}^A_{nn} & \mathbf{0} \\ \mathbf{0} & \mathbf{K}^A_{cc} \end{bmatrix} \begin{bmatrix} \mathbf{g}^A_n \\ \mathbf{g}^A_c \end{bmatrix} = \begin{bmatrix} \mathbf{0} \\ \tilde{\mathbf{f}}^A_c \end{bmatrix}. \tag{4.46}$$

Generalized interface forces $\tilde{\mathbf{f}}^A_c$ equals:

$$\tilde{\mathbf{f}}^A_c = \mathbf{M}^A_{cn}\ddot{\mathbf{g}}^A_n + \mathbf{M}^A_{cc}\ddot{\mathbf{g}}^A_c + \mathbf{K}^A_{cc}\mathbf{g}^A_c. \tag{4.47}$$

Accordingly, generalized interface force $\tilde{\mathbf{f}}^B_c$ is defined as:

$$\tilde{\mathbf{f}}^B_c = \mathbf{M}^B_{cn}\ddot{\mathbf{g}}^B_n + \mathbf{M}^B_{cc}\ddot{\mathbf{g}}^B_c + \mathbf{K}^B_{cc}\mathbf{g}^B_c. \tag{4.48}$$

By introducing (4.47) and (4.48) into (4.32)

$$\mathbf{M}^A_{cn}\ddot{\mathbf{g}}^A_n + \mathbf{M}^A_{cc}\ddot{\mathbf{g}}^A_c + \mathbf{K}^A_{cc}\mathbf{g}^A_c + \mathbf{M}^B_{cn}\ddot{\mathbf{g}}^B_n + \mathbf{M}^B_{cc}\ddot{\mathbf{g}}^B_c + \mathbf{K}^B_{cc}\mathbf{g}^B_c = 0 \tag{4.49}$$

is obtained. The condition (4.31) can now be introduced into (4.49) and the force equilibrium condition receives the following form:

$$\mathbf{M}_{cn}^{A}\ddot{\mathbf{g}}_{n}^{A}+\mathbf{M}_{cn}^{B}\ddot{\mathbf{g}}_{n}^{B}+(\mathbf{M}_{cc}^{A}+\mathbf{M}_{cc}^{B})\ddot{\mathbf{g}}_{c}^{A}+(\mathbf{K}_{cc}^{A}+\mathbf{K}_{cc}^{B})\mathbf{g}_{c}^{A}=0. \tag{4.50}$$

Equation (4.50) can be found in the same form in the equation of motion of the coupled system (4.44), hence the force equilibrium condition is fulfilled.

4.3.4 Reduction of the Number of Constraint Modes

In the traditional Craig-Bampton method the number of constraint modes is firmly connected to the number of interface DOFs while each constraint mode corresponds to the unit value at each interface DOF.

In this dissertation an approach has been developed in which, instead of unit values at each interface DOF, a displacement pattern is applied along the whole interface [Sremcevic et al 2009b]. This approach reduces the number of constraint modes significantly while keeping a similar exactness of the solution. The constraint modes obtained by applying a displacement pattern at the interface will be referred to as *modal constraint modes* and the approach in which they are used will be named the *MCM approach*, while the traditional Craig-Bampton modes will be denoted as nodal constraint modes. Equation (4.15) becomes:

$$\begin{bmatrix}\mathbf{K}_{ii} & \mathbf{K}_{ib}\\ \mathbf{K}_{bi} & \mathbf{K}_{bb}\end{bmatrix}\begin{bmatrix}\mathbf{\Psi}_{ic}\\ \mathbf{\Phi}_{bc}\end{bmatrix}=\begin{bmatrix}\mathbf{0}\\ \mathbf{R}_{bc}\end{bmatrix} \tag{4.51}$$

From equation (4.51) the solution $\mathbf{\Psi}_c$ for the *MCM approach* is obtained:

$$\mathbf{\Psi}_{c}=\begin{bmatrix}\mathbf{\Psi}_{ic}\\ \mathbf{\Phi}_{bc}\end{bmatrix}=\begin{bmatrix}-\mathbf{K}_{ii}^{-1}\mathbf{K}_{ib}\mathbf{\Phi}_{bc}\\ \mathbf{\Phi}_{bc}\end{bmatrix} \tag{4.52}$$

$\mathbf{\Phi}_{bc}$ stands for the forced pattern at the interface. The indexes i and b mark, as well as in the equation (4.15), internal and boundary nodes. Index c denotes the number of constraint modes and, in contrast to the Craig-Bampton nodal approach, in *MCM approach* $c \neq b$.

In *MCM approach* the number of constraint modes depends on the frequency range of interest and therefore the expected vibration pattern at the interface.

In order to decide what kind of displacement pattern should be forced at the interface the following questions have to be considered:

- How can the displacement be introduced along the interface? The answer to this question defines if the constraint or attachment modes are needed. There are two possible answers to this question: The first possibility is to give a certain value to the physical DOFs. That can be achieved by using constraint modes. The second option is to introduce the displacement over the right-hand side (the "force" side) of the equation of motion. In this case the attachment modes are needed.
- What is the boundary condition for both substructures at the end points of the interface (points 1 and 2 in figure 4.7)? The answer to this question defines the boundary conditions for the pattern applied in the *MCM approach*.

If the substructures that meet at the interface are solid structures whose physical DOFs are displacements, the movement of the interface will be provided by using constraint modes.

The shape of the pattern that should be applied in the scope of the *MCM approach* depends on the boundary condition that the assembled structure needs to fulfill. If the assembled structure has pinned boundary conditions, the pattern should also provide a displacement equal to zero at the boundary of the interface and allow a rotation. Those conditions can be fulfilled by applying a sinusoidal pattern for the constraint modes, see figure 4.7 *a*). When the assembled structure has a clamped boundary condition then an appropriate pattern is found using the eigenmodes of a clamped beam, figure 4.7 *b*). In case of the free interface a pattern that allows maximal displacements at the boundaries should be applied, figure 4.7 *c*). Finally, a cosine pattern at the interface describes a boundary condition in which only rotational DOFs are constrained. In case of different boundary conditions in points 1 and 2 combinations of these patterns has to be applied.

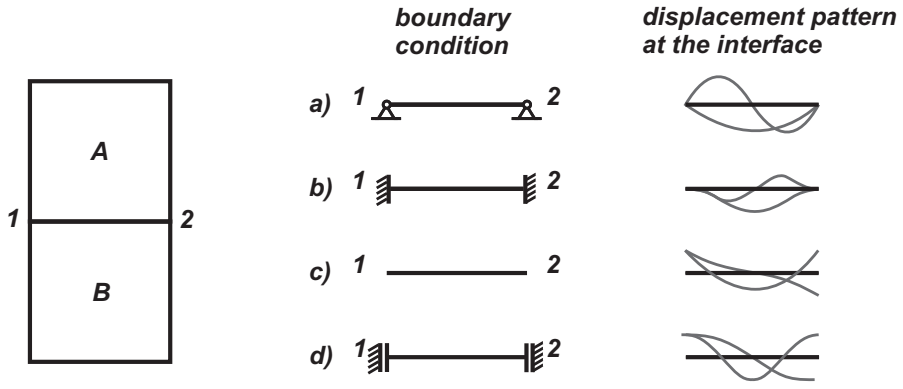

Figure 4.7: Examples for displacement patterns that can be applied on the interface depending on the boundary condition at the end points of the interface

When two fluid substructures, which are described via pressure, are coupled, the displacement of the interface is introduced via attachment modes. The attachment modes are used while the displacement in the fluid system is forced from the right-hand side (the "force" side). For the displacement pattern of the attachment modes all the variants described for the solid substructures are possible, see figure 4.7.

The choice of attachment modes for coupling a fluid and a solid structure will be explained in chapter 4.5.

In the following examples fluid substructures are coupled. Cosine pattern are defined for all attachment modes because the totally reflecting boundary condition is applied on the whole assembled structure so the pressure has its maximal value at the boundaries. For example for the interface $1-2$ in figure 4.7 the cosine pattern is defined as:

$$\mathbf{\Phi}_{bc} = cos\left(\frac{n \cdot x_m \pi}{L_x}\right) \qquad \text{for} \qquad n = 1, 2, ..., c \qquad \text{and} \qquad m = 1, 2, ..., b \tag{4.53}$$

Here c is the number of constraint modes, b barks the size of the set of boundary nodes and l is the length of the interface.

Example 1: 2d Fluid

The reduction of the number of attachment modes used for calculation and the exactness of the obtained results will be shown on the example of a 2D-fluid that is divided into two substructures.

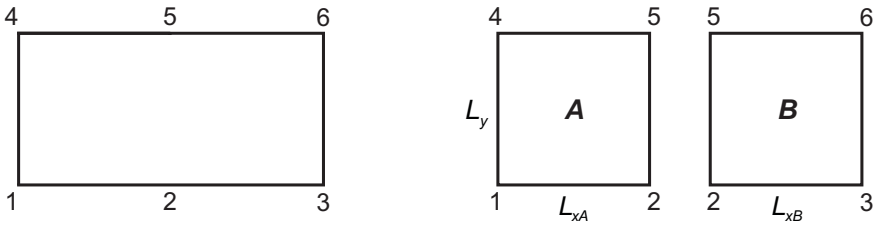

Figure 4.8: A 2d fluid (left) is divided into 2 substructures A and B (right)

In this example the goal is to calculate the first 50 eigenmodes of the fluid shown in figure 4.8 (left). The dimensions of the fluid are $(L_{xA} + L_{xB}) \times L_y$, for this example: $L_{xA} = L_{xB} = L_y$. For the calculations the fluid is divided into substructures A and B along the interface 2-5, see figure 4.8 (right). The substructures are discretized and the normal and attachment modes are computed.

This simple system is taken for the calculations because the analytic solution for such a system i known. The analytic solution for the eigenvalues of the fluid of dimensions $(L_{xA} + L_{xB}) \times L_y$ is determinated by using the following expression:

$$\omega_{ml} = \pi c_f \sqrt{\left(\frac{m}{L_{xA} + L_{xB}} + \frac{l}{L_y}\right)} \qquad \text{with} \qquad m = 0, 1, 2, ... \qquad \text{and} \qquad l = 0, 1, 2, ... \tag{4.54}$$

In figure 4.9 a selection of fixed-interface pressure normal modes of the substructures are shown. Wave numbers in x and y direction are marked with k_x and k_y.

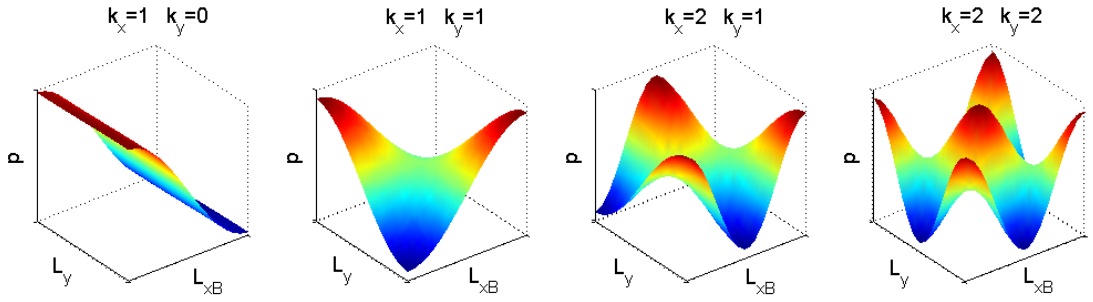

Figure 4.9: Fixed-interface pressure normal modes for the 2d fluid substructure

Figure 4.10 shows exemplarily four nodal attachment modes of the substructure B obtained by applying unit velocity in each interface node. The attachment modes are calculated as a quasi-static modes with a circular frequency $\omega = 1\frac{rad}{s}$ $(\frac{L_y}{\Lambda_f} = \frac{L_y f}{c_f} \approx 0,0005)$.

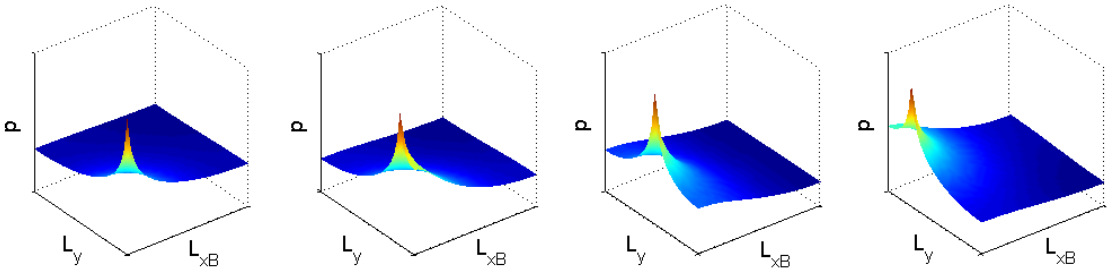

Figure 4.10: Exemplarily presented nodal attachment modes for the 2d fluid substructure B, $L_y = L_{xB}$

Figure 4.11 presents the first four modal attachment modes of the substructure B that are calculated by forcing a cosine velocity pattern $\mathbf{\Phi}_{bc} = cos\frac{\mathbf{k}_c \pi}{L_y}\mathbf{y}_b$ at the interface, where $k_c = 0, 1, 2, 3$. The circular frequency used is again $\omega = 1\frac{rad}{s}$ $(\frac{L_y}{\Lambda_f} \approx 0,0005)$.

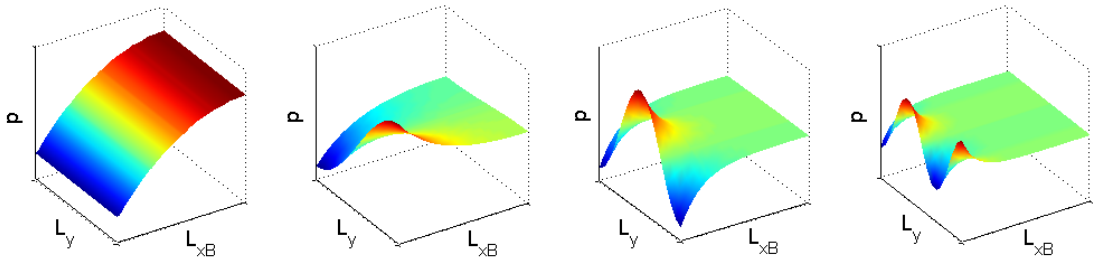

Figure 4.11: The first four modal attachment modes for the 2d fluid substructure B

Figure 4.12 shows the results obtained by using nodal attachment modes. The ordinate shows the number of eigenmode and the abscissa gives the eigenvalue ω_n normalized with respect to the first eigenvalue ω_1. The number of attachment modes is firmly connected with the discretization of the substructure and it equals to the number of interface nodes. In order to get a better approximation of the total structure, the substructures require a finer discretization which necessarily increases the number of attachment modes.

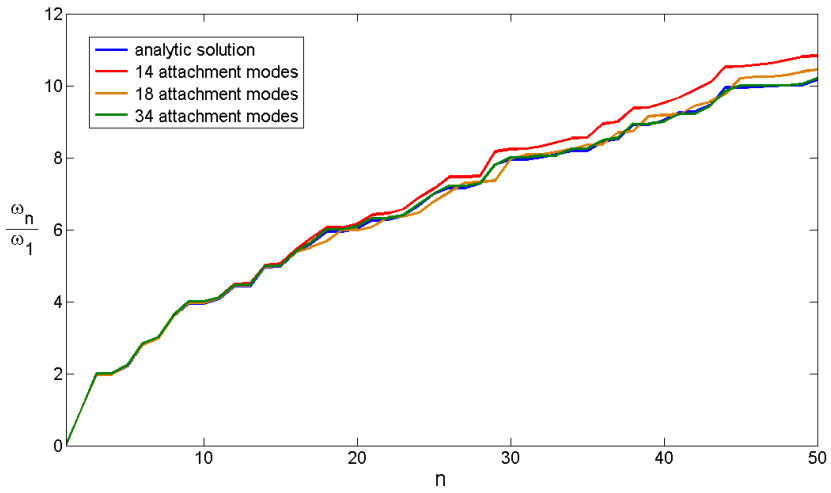

Figure 4.12: The eigenvalues ω_n for n eigenmodes of the total system obtained by coupling of two fluid substructures while using traditional Craig-Bampton method with different number of nodal attachment modes.

In the *MCM approach* the used number of attachment modes is independent from discretization. In figure 4.14 the results obtained by using the *MCM approach* are shown. Analogous to previous example the ordinate shows the number of eigenmode and the abscissa gives the eigenvalue ω_n normalized with respect to the first eigenvalue ω_1.

It can be noticed that a good convergence is achieved while using a significantly smaller number of attachment modes compared to the nodal approach. Furthermore, this example shows that the convergence of the solution in *MCM approach* is good as long as used attachment modes are able to describe the vibration pattern at the interface. In order to explain how many normal and attachment modes are necessary to take in order to achieve a good approximation of the system for certain frequency we will now look back at the wave equation (2.20). If we introduce the solution (2.25) into (2.20) we can see that the wave equation is satisfied if:

$$k_x^2 + k_y^2 + k_z^2 - \frac{1}{c_f^2}\Omega^2 = 0. \tag{4.55}$$

The wave numbers can be written as the number of the wave lengths per length: $k_x = \frac{n_x \pi}{L_x}$, $k_y = \frac{n_y \pi}{L_y}$ and $k_z = \frac{n_z \pi}{L_z}$. If we now introduce these expressions in equation (4.55) we can determine the eigenfrequecies of the 3d fluid:

$$\Omega = c_f \pi \sqrt{\left(\frac{n_x}{L_x}\right)^2 + \left(\frac{n_y}{L_y}\right)^2 + \left(\frac{n_z}{L_z}\right)^2}. \tag{4.56}$$

Equivalently, the eigenfrequencies of a 2d fluid are defined by [Cremer and Müller 1976] as:

$$\Omega = c_f \pi \sqrt{\left(\frac{n_x}{L_x}\right)^2 + \left(\frac{n_y}{L_y}\right)^2}. \tag{4.57}$$

Each curve in figure 4.13 limits the area of all possible combinations of wave numbers that

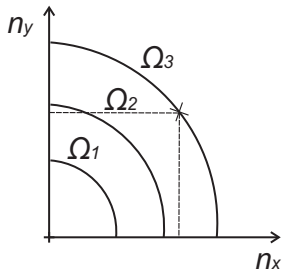

Figure 4.13: The eigenvalues ω_n of the total system obtained by coupling of two fluid substructures while using the *MCM approach* with a different number of modal attachment modes.

can appear under certain frequency (e.g. Ω_1, Ω_2 or Ω_3). With the choice of the number of normal and constraint modes that are taken into account we limit the maximal wave number in x and y direction that we can describe with the approximated model. Therefore, also the maximal frequency for which the approximated model gives good results is limited.

By chosing the number of normal and constraint modes we define the parameters n_x and n_y.

The number of modes of the coupled system that can be determined:

$$N = \pi \sqrt{\left(\frac{n_x}{L_x}\right)^2 + \left(\frac{n_y}{L_y}\right)^2} = \sqrt{k_x^2 + k_y^2} = \frac{\Omega}{c_f} \tag{4.58}$$

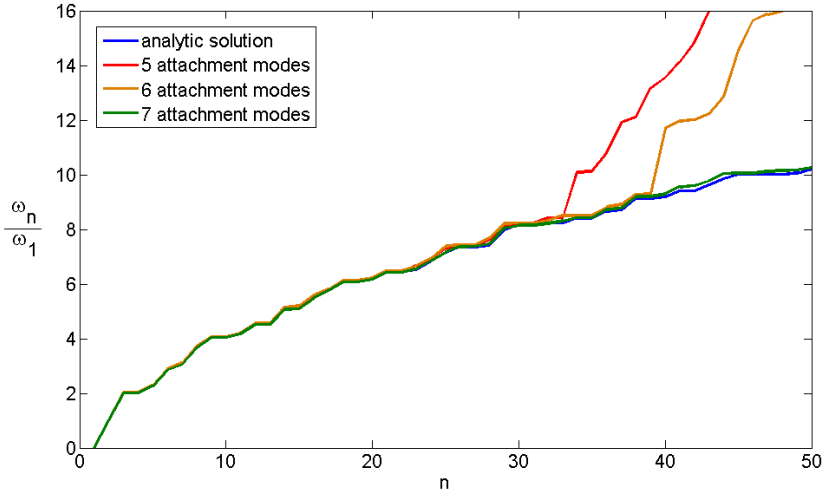

Figure 4.14: The eigenvalues ω_n of the total system obtained by coupling of two fluid substructures while using the *MCM approach* with a different number of modal attachment modes. When using 5 attachment modes N=33 ($\frac{n_x}{L_x} = 3, \frac{n_y}{L_y} = 2$) and for 6 attachment modes N=38 ($\frac{n_x}{L_x} = 3, \frac{n_y}{L_y} = 2, 5$).

Example 2: 3d Fluid

When coupling 3d substructures the number of obligatory nodal attachment modes in the Craig-Bampton method is increasing even more rapidly. Hence, using the *MCM approach* will reduce the size of the transformation matrix notably and therefore it will result in smaller generalized mass and stiffness matrices.

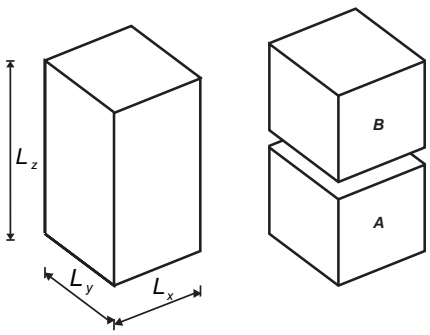

Figure 4.15: A 3d fluid (left) is divided into 2 substructures A and B (right)

Figure 4.16 shows the attachment modes for a 3d fluid substructure calculated with the help of the *MCM approach*. The pattern applied at the interface is:

$$\mathbf{\Phi}_{bc} = cos\frac{k_{cx}\pi}{L_x}\mathbf{x}_b cos\frac{k_{cy}\pi}{L_y}\mathbf{y}_b. \tag{4.59}$$

The circular frequency used for determining the attachment modes is $\omega = 1\frac{rad}{s}$ ($\frac{L_x}{\Lambda_f} = \frac{L_y}{\Lambda_f} \approx 0,0005$).

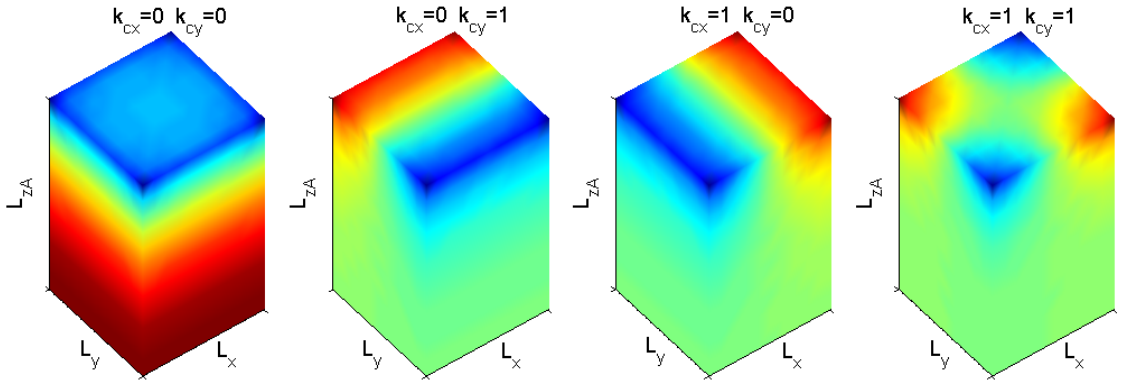

Figure 4.16: Modal attachment modes for the 3d fluid substructure A with dimensions L_x, L_y and L_{zA} ($L_x = L_y$)

In this example the first 20 eigenvalues of the 3D fluid were calculated. The fluid is divided into two substructures A and B. Each substructure is approximated with 10 normal modes and 4 modal attachment modes. Figure 4.17 shows that this approximation is giving results that are identical with analytical solution for the first 15 eigenvalues. After the $15th$ the wave lengths at the interface are smaller then L_x and L_y and more attachment modes should be used. The ordinate shows the number of eigenmode and the abscissa gives the eigenvalue ω_n normalized with respect to the first eigenvalue ω_1.

In case of using the nodal approach the number of necessary attachment modes with the same discretization that is used in the *MCM approach*, would be 121, which greatly surpasses the number of used normal modes and therefore reduces the efficiency of modal reduction.

Example 3: Complex geometry

Model reduction methods are developed for examining more complex geometries. In general, when a structure consists of several substructures, the procedure described on the example

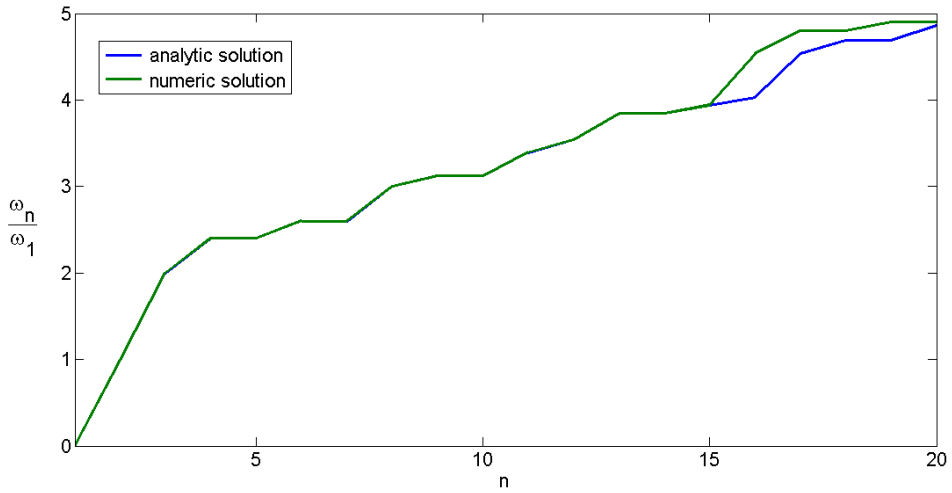

Figure 4.17: Eigenvalues ω_n of a 3d fluid; Analytic solution (blue line) and the numerical solution obtained by applying the *MCM approach* (green line), $\frac{n_x}{L_x} = \frac{n_y}{L_y} = 1$ and $\frac{n_z}{L_z} = 1,5$

of two substructures can simply be applied. The only exception is a case when more than two substructures have a common interface point. An example of such structure is given in figure 4.18, where all three substructures meet in the node number 5.

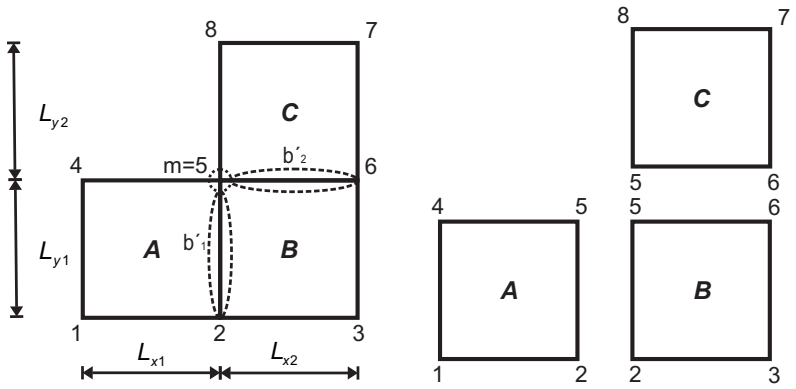

Figure 4.18: "L"-shaped fluid structure (left) divided into three substructures A, B and C (right)

In this case the boundary nodes b are divided into the middle node m (node number 5 in figure 4.18) and other boundary nodes b'. Two sets of attachment modes are used in this case. The first set of the modes include the attachment modes $\mathbf{\Psi}_a$ that are the result of a pattern $\mathbf{\Phi}_{b'a}$ applied on the set of boundary nodes b'. The second set $\mathbf{\Psi}_m$ is result of the pattern $\mathbf{\Phi}_{mm}$ applied in the set of boundary nodes m. In a 2d example presented here, the set of boundary nodes m includes only one node so $\mathbf{\Psi}_m$ will consist of only one attachment mode that will correspond to unit displacement in the central node.

The transformation matrix for one substructure when the modal constraint modes are used has the following form:

$$\mathbf{T_{CB}} = \begin{bmatrix} \mathbf{\Psi}^A_{in} & \mathbf{\Psi}^A_{ia} & \mathbf{\Psi}^A_{im} \\ 0 & \mathbf{\Phi}^A_{b'a} & \mathbf{\Psi}^A_{b'm} \\ 0 & \mathbf{\Psi}^A_{ma} & \mathbf{\Phi}^A_{mm} \end{bmatrix}. \tag{4.60}$$

Here, index i marks internal nodes, n the number of normal modes and a the number of used modal attachment modes.

When the transformation is performed, the mass and stiffness matrices of one substructure have the following form:

$$\begin{aligned} \mathbf{M}_{CB} &= \begin{bmatrix} \mathbf{I}_{nn} & \mathbf{M}_{na} & \mathbf{M}_{nm} \\ \mathbf{M}_{an} & \mathbf{M}_{aa} & \mathbf{M}_{am} \\ \mathbf{M}_{mn} & \mathbf{M}_{ma} & \mathbf{M}_{mm} \end{bmatrix} \\ \mathbf{K}_{CB} &= \begin{bmatrix} \mathbf{\Lambda}_{nn} & \mathbf{0} & \mathbf{0} \\ \mathbf{0} & \mathbf{K}_{aa} & \mathbf{K}_{am} \\ \mathbf{0} & \mathbf{K}_{ma} & \mathbf{K}_{mm} \end{bmatrix} \end{aligned} \tag{4.61}$$

In order to connect the dependent generalized coordinates the component coupling matrix S is again defined as:

$$\mathbf{g} = \begin{bmatrix} \mathbf{g}^A_n \\ \mathbf{g}^A_{a1} \\ \mathbf{g}^A_m \\ \mathbf{g}^B_n \\ \mathbf{g}^B_{a1} \\ \mathbf{g}^B_{a2} \\ \mathbf{g}^B_m \\ \mathbf{g}^C_n \\ \mathbf{g}^C_{a2} \\ \mathbf{g}^C_m \end{bmatrix} = \underbrace{\begin{bmatrix} \mathbf{I} & 0 & 0 & 0 & 0 & 0 \\ 0 & \mathbf{I} & 0 & 0 & 0 & 0 \\ 0 & 0 & \mathbf{I} & 0 & 0 & 0 \\ 0 & 0 & 0 & \mathbf{I} & 0 & 0 \\ 0 & \mathbf{I} & 0 & 0 & 0 & 0 \\ 0 & 0 & 0 & 0 & \mathbf{I} & 0 \\ 0 & 0 & \mathbf{I} & 0 & 0 & 0 \\ 0 & 0 & 0 & 0 & 0 & \mathbf{I} \\ 0 & 0 & 0 & 0 & \mathbf{I} & 0 \\ 0 & 0 & \mathbf{I} & 0 & 0 & 0 \end{bmatrix}}_{\mathbf{S}} \begin{bmatrix} \mathbf{g}^A_n \\ \mathbf{g}_{a1} \\ \mathbf{g}_m \\ \mathbf{g}^B_n \\ \mathbf{g}_{a2} \\ \mathbf{g}^C_n \end{bmatrix}, \tag{4.62}$$

where index $a1$ marks the number of attachment modes used to approximate the vibration pattern of the interface $2-5$ and $a2$ stands for the number of attachment modes used to approximate the vibration pattern of the interface $5-6$.

Finally with the help of the component coupling matrix S the mass and stiffness matrices of the system which consists of three substructures that all have a common node can be formed:

$$\mathbf{M} = \begin{bmatrix} \mathbf{I}^A_{nn} & \mathbf{M}^A_{na1} & \mathbf{M}^A_{nm} & \mathbf{0} & \mathbf{0} & \mathbf{0} \\ \mathbf{M}^A_{a1n} & \mathbf{M}^A_{a1a1} + \mathbf{M}^B_{a1a1} & \mathbf{M}^A_{a1m} + \mathbf{M}^B_{a1m} & \mathbf{M}^B_{a1n} & \mathbf{M}^B_{a1a2} & \mathbf{0} \\ \mathbf{M}^A_{mn} & \mathbf{M}^A_{ma1} + \mathbf{M}^B_{ma1} & \mathbf{M}^A_{mm} + \mathbf{M}^B_{mm} + \mathbf{M}^C_{mm} & \mathbf{M}^B_{mn} & \mathbf{M}^B_{ma2} + \mathbf{M}^C_{ma2} & \mathbf{M}^C_{mn} \\ \mathbf{0} & \mathbf{M}^B_{na1} & \mathbf{M}^B_{nm} & \mathbf{M}^B_{nn} & \mathbf{M}^B_{na2} & \mathbf{0} \\ \mathbf{0} & \mathbf{M}^B_{a2a1} & \mathbf{M}^B_{a2m} + \mathbf{M}^C_{a2m} & \mathbf{M}^B_{a2n} & \mathbf{M}^B_{a2a2} + \mathbf{M}^C_{a2a2} & \mathbf{M}^C_{a2n} \\ \mathbf{0} & \mathbf{0} & \mathbf{M}^C_{nm} & \mathbf{0} & \mathbf{M}^C_{na2} & \mathbf{M}^C_{nn} \end{bmatrix}$$

$$\mathbf{K} = \begin{bmatrix} \mathbf{\Lambda}^A_{nn} & \mathbf{0} & \mathbf{0} & \mathbf{0} & \mathbf{0} & \mathbf{0} \\ \mathbf{0} & \mathbf{K}^A_{a1a1} + \mathbf{K}^B_{a1a1} & \mathbf{K}^A_{a1m} + \mathbf{K}^B_{a1m} & \mathbf{0} & \mathbf{K}^B_{a1a2} & \mathbf{0} \\ \mathbf{0} & \mathbf{K}^A_{ma1} + \mathbf{K}^B_{ma1} & \mathbf{K}^A_{mm} + \mathbf{K}^B_{mm} + \mathbf{K}^C_{mm} & \mathbf{0} & \mathbf{K}^B_{ma2} + \mathbf{K}^C_{ma2} & \mathbf{0} \\ \mathbf{0} & \mathbf{0} & \mathbf{0} & \mathbf{\Lambda}^B_{nn} & \mathbf{0} & \mathbf{0} \\ \mathbf{0} & \mathbf{K}^B_{a2a1} & \mathbf{K}^B_{a2m} + \mathbf{K}^C_{a2m} & \mathbf{0} & \mathbf{K}^B_{a2a2} + \mathbf{K}^C_{a2a2} & \mathbf{0} \\ \mathbf{0} & \mathbf{0} & \mathbf{0} & \mathbf{0} & \mathbf{0} & \mathbf{\Lambda}^C_{nn} \end{bmatrix} \tag{4.63}$$

Figure 4.19 presents eigenvalues of the structure shown in figure 4.18 (left). The green line shows the eigenvalues obtained from the FEM solution of the full system, while the red and blue lines mark the values obtained after applying the *MCM approach* while varying the number of attachment modes used for the approximation of the substructures. For the description of interfaces $2-5$ and $5-6$ the same number of attachment modes is used because in this example interfaces have the same length.

When deciding how many normal and attachment modes will be taken into account, one should first determine which is the highest frequency of interest f_h. Hereafter it is necessary do determine which are the shortest wave lengths that can appear in substructures for that frequency (e.g. for a fluid $\lambda_{min} = \frac{c_f}{f_h}$). Finally, the normal and the attachment modes of all substructures have to be able to describe the wave lengths $\lambda \geq \lambda_{min}$ in all observed dimensions (1d, 2d or 3d). When the normal or the attachment modes are not able to describe the vibration pattern significant errors occur like in the example shown in 4.14.

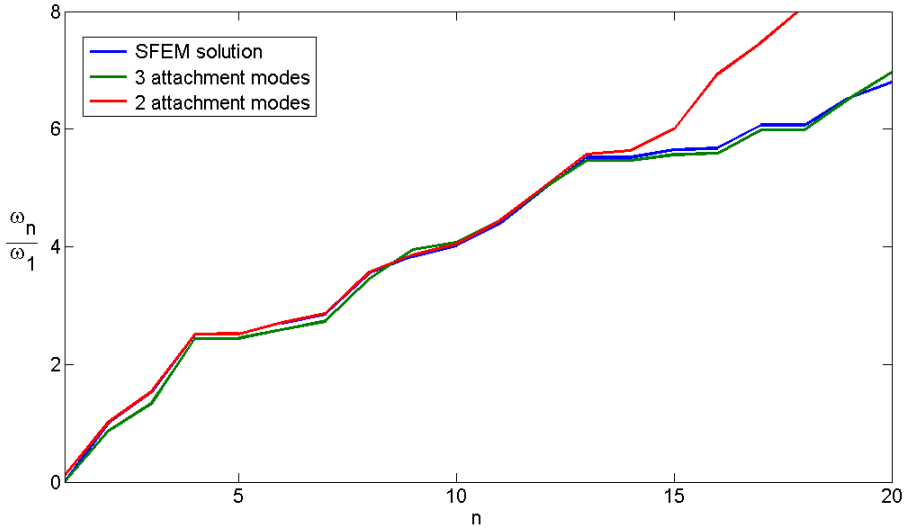

Figure 4.19: Eigenvalues ω_n of the "L-shaped" structure obtained by using the *MCM approach*

From figure 4.19 can be seen that the approximation of the substructures in which 2 attachment modes were used for description of each boundary is giving good results for the first 13 eigenvalues. For calculating 20 eigenvalues 3 attachment modes need to be used in order to properly describe the vibration of the interface.

Figure 4.20 shows four pressure modes of the structure sketched in figure 4.18 (left) obtained by the *MCM approach*. The transformation matrix for each substructure consists of 10 normal and 3 attachment modes.

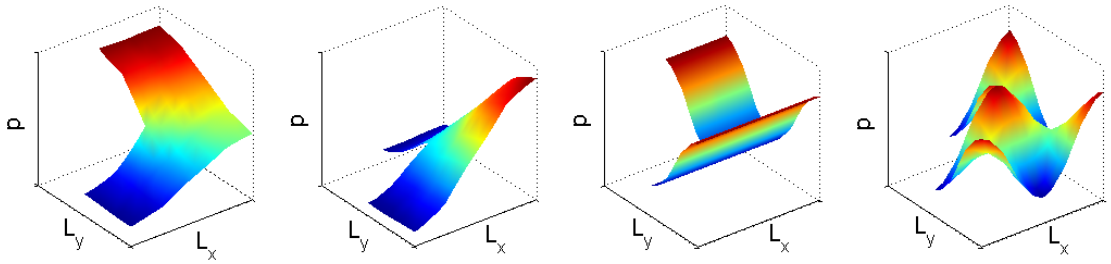

Figure 4.20: Exemplarily selected pressure normal modes of the structure sketched in figure 4.18 (left) obtained with the *MCM approach*

4.4 Steady-state Solution with the Help of Modal Analysis

In this section it will be shown how the Craig-Bampton method can be applied in the scope of the modal analysis and which problems can occur due to the modal truncation.

In the modal analysis the solution of the equation (4.11) is sought.

$$\mathbf{g}(t) = (\mathbf{K}^c_{CB} - \Omega^2 \mathbf{M}^c_{CB})^{-1} \cdot \mathbf{F}_{CB} e^{i\Omega t} = \mathbf{g}_0 e^{i\Omega t}. \tag{4.64}$$

The response in physical DOFs is obtained with the help of the back transformation:

$$\mathbf{u}_0 = \mathbf{T}_{CB} \mathbf{g}_0. \tag{4.65}$$

4.4.1 Root-point Excitation

In case of a root-point excitation of a structure or a pressure source in a fluid the following pre-processing needs to be executed before performing the Craig-Bampton transformation [Young 2000].

If we observe the equation of motion of one substructure in physical DOFs and take into account only the external load (the influence of other substructures is introduced over constraint modes) on which a harmonic root-point excitation is acting we receive:

$$\left(\begin{bmatrix} \mathbf{K}_{\bar{r}\bar{r}} & \mathbf{K}_{\bar{r}r} \\ \mathbf{K}_{r\bar{r}} & \mathbf{K}_{rr} \end{bmatrix} - \Omega^2 \begin{bmatrix} \mathbf{M}_{\bar{r}\bar{r}} & \mathbf{M}_{\bar{r}r} \\ \mathbf{M}_{r\bar{r}} & \mathbf{M}_{rr} \end{bmatrix} \right) \begin{bmatrix} \mathbf{u}_{\bar{r}} \\ \mathbf{u}_r \end{bmatrix} = \begin{bmatrix} \mathbf{0} \\ \mathbf{f}_r \end{bmatrix} \tag{4.66}$$

Index r marks the nodes in which the root-point excitation is acting while index $\bar{r}$ stands for its complement in the set of total DOFs. Forces $\mathbf{f}_r$ are usually not known initially. Only the values $\mathbf{u}_r$ are known. The forces $\mathbf{f}_r$ are the forces that are needed to produce the desired value $\mathbf{u}_r$ .They are determined in the following steps: from the first equation in (4.66) we can calculate $\mathbf{u}_{\bar{r}}$:

$$\mathbf{u}_{\bar{r}} = -\left(\mathbf{K}_{\bar{r}\bar{r}} - \Omega^2 \mathbf{M}_{\bar{r}\bar{r}}\right)^{-1} \left(\mathbf{K}_{\bar{r}r} - \Omega^2 \mathbf{M}_{\bar{r}r}\right) \mathbf{u}_r. \tag{4.67}$$

Inserting this in the second equation of (4.66), $\mathbf{f}_r$ can be determined by:

$$\mathbf{f}_r = \left(\mathbf{K}_{r\bar{r}} - \Omega^2 \mathbf{M}_{r\bar{r}}\right) \mathbf{u}_{\bar{r}} + \left(\mathbf{K}_{rr} - \Omega^2 \mathbf{M}_{rr}\right) \mathbf{u}_r. \tag{4.68}$$

With the help of the transformation matrix $\mathbf{T}_{CB}$ the generalized load can be determined:

$$\mathbf{F}_{CB} = \mathbf{T}_{CB}^{T} \cdot \mathbf{f}_r \tag{4.69}$$

and the response of the reduced system can be calculated:

$$\mathbf{g}_r = \left(\mathbf{K}_{CB} - \Omega^2 \mathbf{M}_{CB}\right)^T \cdot \mathbf{F}_{CB}. \tag{4.70}$$

The response in physical DOFs is obtained by using equation (4.65).

4.4.2 Modal Truncation

Model reduction methods exclude the higher oscillation modes in order to provide saving in calculation time and computer storage like it has already been explained at the beginning of this chapter. This reduction can change the modal representation of the loading applied on the structure and therefore it can affect the quality of the calculated response. The inaccuracy of the calculated response can appear due to inconsideration of modal truncation on the spatial representation of the applied load [Chopra 2000].

The part of the load that is not represented by the normal modes that are taken into account is named force truncation vector and it is denoted with $\mathbf{F}_t$. The force truncation vector is used to represent the contribution of the modes which have eigenvalues that are higher than the frequency content of the loading so their response should be quasi-static.

The part of the load that is described by the kept eigenvectors $\mathbf{F}_k$ can be calculated from the following expression:

$$\mathbf{F}_k = \mathbf{K}\mathbf{u}_{CB}. \tag{4.71}$$

$\mathbf{u}_{CB}$ is the response of the system on which the modal load $\mathbf{F}_{CB}$ is applied. By multiplying the generalized force with the transformation matrix $\mathbf{T}_{CB}$ the force is transformed from the domain of generalized coordinates to the domain of the natural DOFs.

The force truncation vector is determined as a difference between the spatial load vector $\mathbf{F}_0$ and the part of the load that is described by the kept eigenvectors $\mathbf{F}_k$.

$$\mathbf{F}_t = \mathbf{F}_0 - \mathbf{F}_k \tag{4.72}$$

The quality of the calculated response can be improved by reducing $\mathbf{F}_t$. This can be achieved by increasing the number of kept modes. However, the number of kept modes needed for

convergence to an exact solution is significant and it can destroy the positive effects of modal truncation because the achieved reduction of the calculation time would not be evidential, see Example 4. In [Dickens et al 1997] two most commonly used methods for reduction of modal truncation error the *Mode acceleration method* and the *Modal truncation augmentation method* are compared. The modal truncation augmentation method showed to be more exact and simpler for implementation.

4.4.3 The Modal Truncation Augmentation Method

The modal truncation augmentation method is improving the spatial representation of the loading by introducing the additional pseudo-eigenmodes also known as MT vectors [Dickens and Pool 1992]. These modes are called pseudo-eigenmodes because they are orthogonal on the set of eigenmodes that are taken into account but they are not orthogonal on the full set of eigenmodes of the system.

For determining the MT vector the effect of the force truncation vector is calculated:

$$\mathbf{X}_t = \mathbf{K}^{-1}\mathbf{F}_t. \tag{4.73}$$

Afterwards, the reduced eigenvalue problem is solved:

$$\bar{K}Q = \bar{M}Q\bar{\omega}_p^2, \tag{4.74}$$

with

$$\bar{K} = \mathbf{X}_t^T\mathbf{K}\mathbf{X}_t \qquad \text{and} \qquad \bar{M} = \mathbf{X}_t^T\mathbf{M}\mathbf{X}_t?$$

$\bar{\omega}_p$ is the pseudo-eigenfrequency of the MT vector.

Finally, the MT vector $\mathbf{\Psi}_{MT}$ is determined from:

$$\mathbf{\Psi}_{MT} = \mathbf{X}_t Q. \tag{4.75}$$

This vector is added to the transformation matrix $\mathbf{T}_{CB}$

$$\mathbf{T_{CB}} = \begin{bmatrix} \mathbf{\Psi}_{in}^A & \mathbf{\Psi}_{ic}^A & \mathbf{\Psi}_{iMT}^A \\ 0 & \mathbf{I}_{bc}^A & \mathbf{\Psi}_{bMT}^A \end{bmatrix}. \tag{4.76}$$

Equation (4.76) shows that the Modal Truncation Augmentation Method can simply be applied in the scope of the Craig-Bampton method.

Example 4: Application of the Modal Truncation Augmentation Method

The effectiveness of the modal truncation augmentation method is shown on the example of a simple beam of the length $L_x = 4m$ that is exited with a harmonic force $Fcos(\Omega t)$ applied on a distance $a = 0,24m$ from the left support of the beam, see figure 4.21.

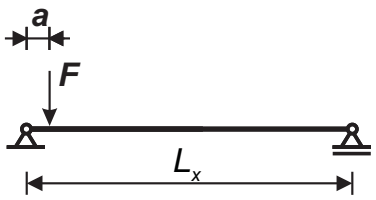

Figure 4.21: Simple beam exited with a harmonic force $Fcos(\Omega t)$

The Young's modulus of the beam is $E = 210GPa$, moment of inertia $I = 10^{-4}m^4$, density $\rho = 7850kg/m^3$. Amplitude of the force is $F = 100kN$ and the circular frequency $\Omega = 400rad/s$. According to the advice stated in chapter 4.3 which states that in the modal analysis the eigenmodes whose frequency is lower than $1,5\Omega$ should be taken into account, four eigenmodes of the beam are taken. Figure 4.22 shows how the dependency between the truncation frequency and truncated part of the load F_t. It can be seen that for 600 rad/s the truncated part of the load is about $0,05F_0$ and this part of the load will be represented with the MT vector. The truncated part of the load can be reduced by increasing the truncation frequency, but figure 4.22 shows that if we want to achieve: $F = 0,01F_0$, the truncation frequency should be 2600 rad/s which would increase the necessary number of normal modes from 4 to 14 which reduces the effectiveness of the method. In figure 4.22 the ordinate shows the ratio of the absolute values of the truncated and initial load.

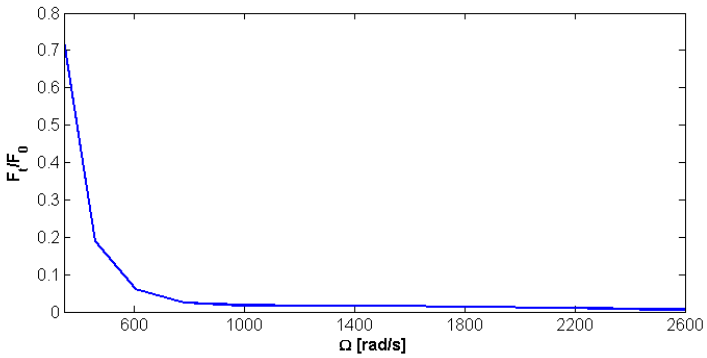

Figure 4.22: The ratio between the truncated load F_t and the original load F_0 depending on the truncation frequency

Figure 4.23 shows the spectrum of the harmonic load $Fcos\Omega t$ and generalized force $\mathbf{F}_{CB}$. The forms of the eigenmodes and the MT vectors that are included in the transformation matrix are also sketched.

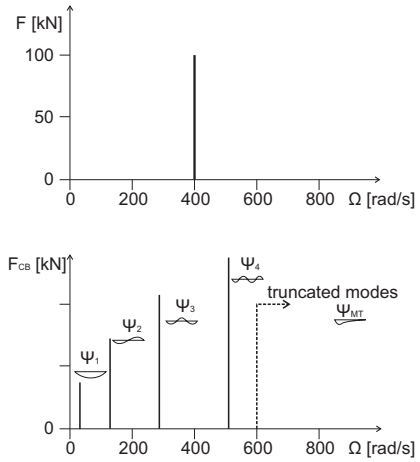

Figure 4.23: The spectrum of the harmonic load $Fcos\Omega t$ and generalized force F_{CB}

The obtained response of the beam is shown in figure 4.24 with a red line. The response of the full FE model is shown with the blue line.

The modal truncation augmentation method is applied to calculate the additional MT vector $\mathbf{\Psi}_{MT}$. After repeating the modal analysis with the additional MT vector the response shown with the dashed lite-blue line is obtained. It can be noticed that the eigenmodes can present the dynamic response of the beam but the use MT vector is necessary in order to present the missing spatial part of the load.

This simple example shows that the modal truncation augmentation method can increase the exactness of the modal analysis significantly.

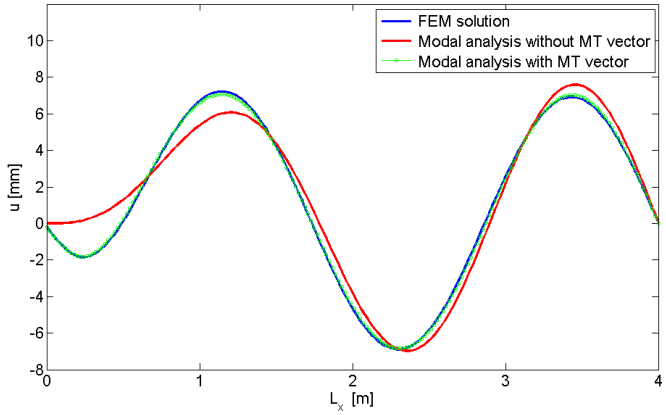

Figure 4.24: Response of the simple beam on a harmonic loading calculated by application of the modal truncation augmentation method

4.5 Application of the MCM approach in FSI problems

In this chapter the implementation of the *MCM approach* in FSI problems will be explained. The configurations in which the vibrating structure is at the boundary of the fluid (figure 4.25 *a*))as well as inside of the fluid (figure 4.25 *b*)) will be considered. In figure 4.25 the fluid is marked with F and the structure is denoted with S and its position is showed with a dashed line.

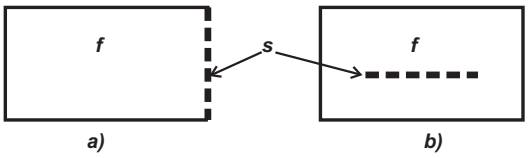

Figure 4.25: Examples of FSI problems that have been analyzed with the *MCM approach*

In chapter 3 the equation of motion for the system that consists of a fluid and a structure for the mixed pressure-displacement formulation is derived and a method for acceleration of the calculations by symmetrization of the mass and stiffness matrices is described.

In this work another method for fastening the calculations is suggested. The idea is to observe the fluid and the structure as two separate substructures. The mass and stiffness

matrices are symmetric for both substructures and normal and attachment modes can be calculated efficiently.

Example 5: FSI problem in 2d

For the coupled system shown in figure 4.25 *a*) fixed interface normal modes have the same shape like the modes shown in figure 4.9.

The 1d structure is modeled as a beam. The normal modes of the beam are calculated with clamped boundary conditions, see figure 4.26.

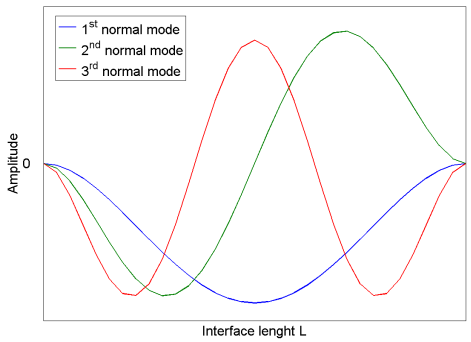

Figure 4.26: Normal modes of the clamped beam

Based on criteria for choosing constraint/attachment modes that are given in chapter 4.3.4 it can be concluded that attachment modes are needed. The attachment modes should allow the fluid to move at the interface. As a pattern the normal modes of the beam can be applied because that way the boundary conditions will automatically be fulfilled, see figure 4.27. The circular frequency used for determining the attachment modes is $\omega = 1\frac{rad}{s}$ $(\frac{L_x}{\Lambda_f} \approx 0,0005)$.

The attachment modes for the beam are calculated by applying the pressure that appears at the interface in the fluid normal modes.

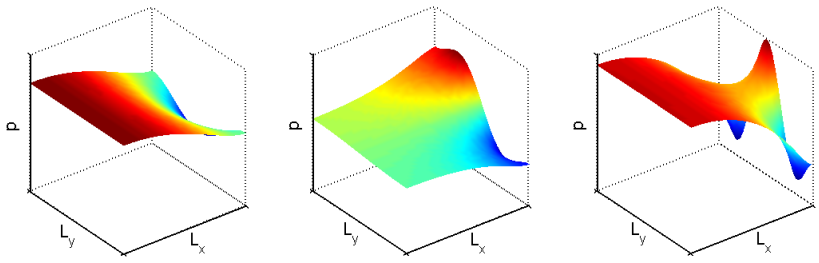

Figure 4.27: Attachment modes for the FSI interaction problem sketched in figure 4.25 a)

In contrast to the assembly of the system in which all substructures are just fluids or just structures where the reduced mass and stiffness matrices are created on the substructural level in FSI problems, the systems matrices are created for the coupled system and afterwards the system's reduced matrices are calculated.

The system's mass and stiffness matrices are defined in (3.38).

The transformation matrix T_{CB} has the following form:

$$\mathbf{T_{CB}} = \begin{bmatrix} \mathbf{\Psi}^f_{in} & \mathbf{0} & \mathbf{\Psi}^f_{ia} & \mathbf{0} \\ \mathbf{\Psi}^f_{bn} & \mathbf{0} & \mathbf{\Psi}^f_{ba} & \mathbf{0} \\ \mathbf{0} & \mathbf{\Psi}^s_{n} & \mathbf{0} & \mathbf{\Psi}^s_{a} \end{bmatrix} \tag{4.77}$$

In equation (4.60) indices n and a mark the normal and attachment modes while f and s denote the fluid and the structure. The size of the transformation matrix is $(N_f + N_s) \times (n_f + n_s + a_f + a_s)$. N_f and N_s stand for the number of physical DOFs of the fluid and structure, n_f, n_s are the kept number of fluid and structure normal modes and a_s and a_f are the number of attachment modes in the fluid and structure.

The generalized mass and stiffness matrices are calculated using equation (4.10).

Figure 4.28 shows that the approximation of the system with the *MCM approach* gives the same values for the first 28 eigenvalues as the full FEM model. For the approximation of the system the fluid is presented with 25 normal and 5 attachment modes while the structure is described with 5 normal modes. The calculation time needed for calculating the first 30 eigenvalues in the full FEM model of the coupled system is 5.17 seconds while for the reduced system the elapsed time was 3.64 seconds. For the calculations a PC with 8Gb RAM memory was used. The assembling of the system mass and stiffness matrices and the calculation of the normal and attachment modes for the *MCM approach* is included in the stated calculation time. The FEM model has 1155 physical DOFs while the reduced system has 35 generalized DOFs. The used number of normal and attachment modes was sufficient for determinating the first 28 eigenvalues of the coupled system. For determinating more eigenvalues of the coupled system more normal and attachment modes should be used in order to be able to describe the vibration pattern of the coupled system.

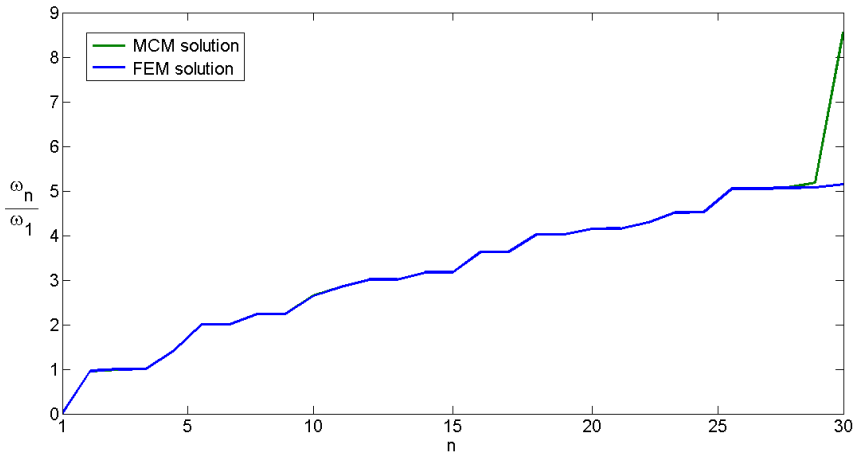

Figure 4.28: Eigenvalues ω_n of the coupled system calculated using the FEM method (blue line) and by applying the *MCM approach* (green line)

In this example also the radiation of the structure under and above the coincidence frequency is observed. The coincidence frequency was calculated by using the equation (2.64). Figure 4.29 shows the vibration pattern of the coupled system for different frequencies. Figure 4.29 left, shows an eigenmode of the coupled system for frequency $f < f_c$ and figure 4.29 right shows an eigenmode of the coupled system for frequency $f > f_c$.

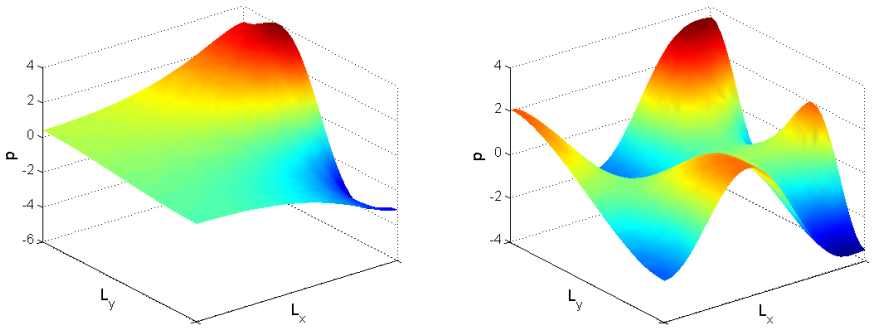

Figure 4.29: Eigenmodes of the 2d coupled system for different frequencies

For the coupled system shown in figure 4.25 *b*) the nodes in the fluid need to be defined on both sides of the structure. The fluid boundary nodes b are divided into groups $b1$ on the upper side of the structure and $b2$ on the bottom side of the structure, see figure 4.30.

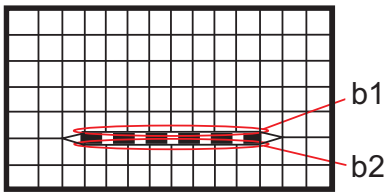

Figure 4.30: Nodes in fluid are defined on both sides of the solid structure

The attachment modes are shown in figure 4.31. They are again calculated as a quasi-static modes with a circular frequency $\omega = 1\frac{rad}{s}(\frac{L_x}{\Lambda_f} \approx 0,001)$.

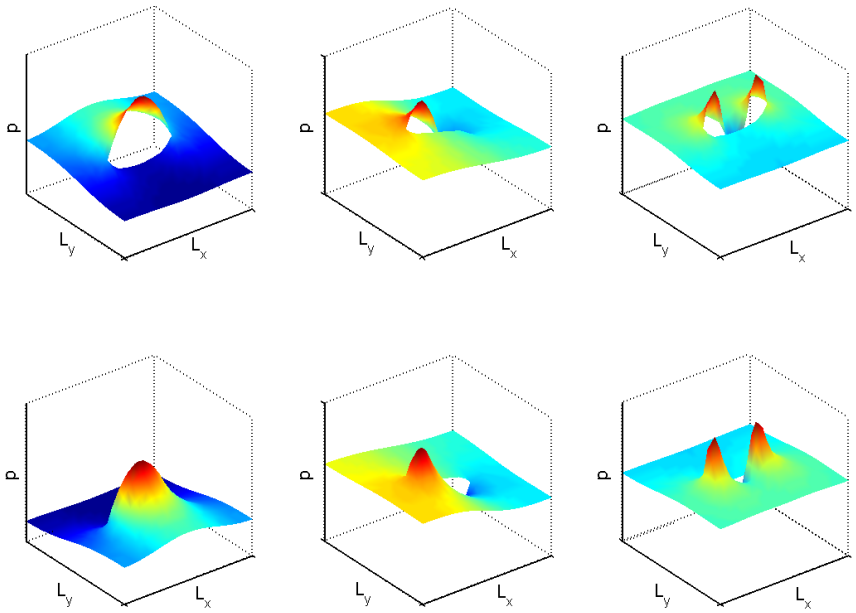

Figure 4.31: Attachment modes for the boundary nodes $b1$ (upper row) and attachment modes for boundary nodes $b2$ (lower row)

The coupling matrices for these two groups of boundary nodes will differ in sign because the outward normal vector $\mathbf{n}$ at the fluid-structure interface S_l (see equation (3.38)) has the opposite direction. Therefore, the system mass and stiffness matrices have the following

form:

$$\begin{aligned}
\mathbf{M_{sys}} &= \begin{bmatrix} \mathbf{M}^f_{ii} & \mathbf{M}^f_{ib1} & \mathbf{M}^f_{ib2} & 0 \\ \mathbf{M}^f_{b1i} & \mathbf{M}^f_{b1b1} & \mathbf{M}^f_{b1b2} & \mathbf{M}^{fs}_{b1} \\ \mathbf{M}^f_{b2i} & \mathbf{M}^f_{b2b1} & \mathbf{M}^f_{b2b2} & -\mathbf{M}^{fs}_{b2} \\ 0 & 0 & 0 & \mathbf{M}^s \end{bmatrix} \\
\mathbf{K_{sys}} &= \begin{bmatrix} \mathbf{K}^f_{ii} & \mathbf{K}^f_{ib1} & \mathbf{K}^f_{ib2} & 0 \\ \mathbf{K}^f_{b1i} & \mathbf{K}^f_{b1b1} & \mathbf{K}^f_{b1b2} & 0 \\ \mathbf{K}^f_{b2i} & \mathbf{K}^f_{b2b1} & \mathbf{K}^f_{b2b2} & 0 \\ 0 & \mathbf{K}^{fs}_{b1} & -\mathbf{K}^{fs}_{b2} & \mathbf{M}^s \end{bmatrix}
\end{aligned} \tag{4.78}$$

and the transformation matrix will be:

$$\mathbf{T_{CB}} = \begin{bmatrix} \mathbf{\Psi}^f_{in} & \mathbf{0} & \mathbf{\Psi}^f_{ia1} + \mathbf{\Psi}^f_{ia2} & \mathbf{0} \\ \mathbf{\Psi}^f_{b1n} & \mathbf{0} & \mathbf{\Psi}^f_{b1a1} + \mathbf{\Psi}^f_{b1a2} & \mathbf{0} \\ \mathbf{\Psi}^f_{b2n} & \mathbf{0} & \mathbf{\Psi}^f_{b2a1} + \mathbf{\Psi}^f_{b2a2} & \mathbf{0} \\ \mathbf{0} & \mathbf{\Psi}^s_{n} & \mathbf{0} & \mathbf{\Psi}^s_{a1} + \mathbf{\Psi}^s_{a2} \end{bmatrix}. \tag{4.79}$$

Exemplarily three normal modes of the coupled system that are obtained by applying the *MCM approach* are shown in figure 4.32. The blue arrows show the gradient of the fluid substructure and the red line presents the displacements of the solid substructure.

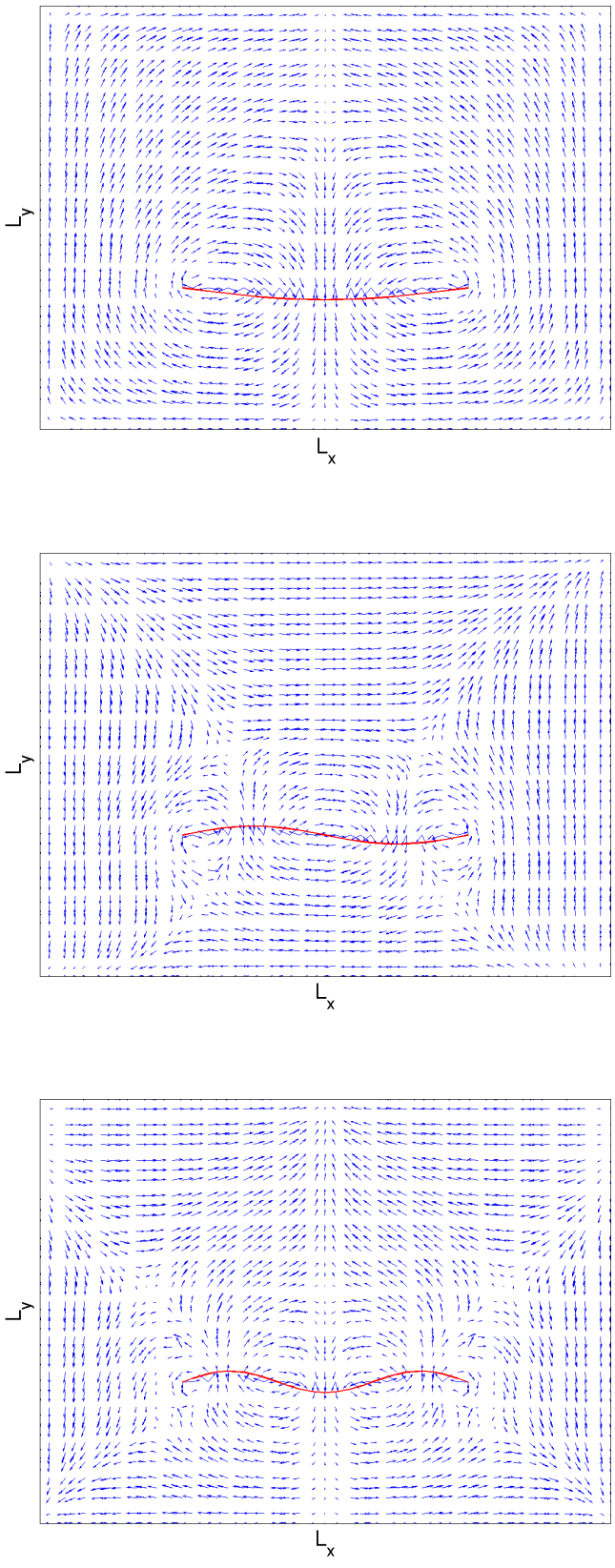

Figure 4.32: Normal modes of the coupled system

Example 6: FSI problem in 3d

The *MCM approach* was also applied for the coupling of a 3d fluid with a 2d radiating structure shown in figure 4.33. The fluid dimensions are $[0; L_x]$, $[0; L_y]$, $[0; L_z]$. The structure coordinates are $[x_s; x_s + d_s]$, $[y_s; y_s + l_s]$, $[0; h_z]$. The boundary of the structure at the position $z = 0$ is clamped.

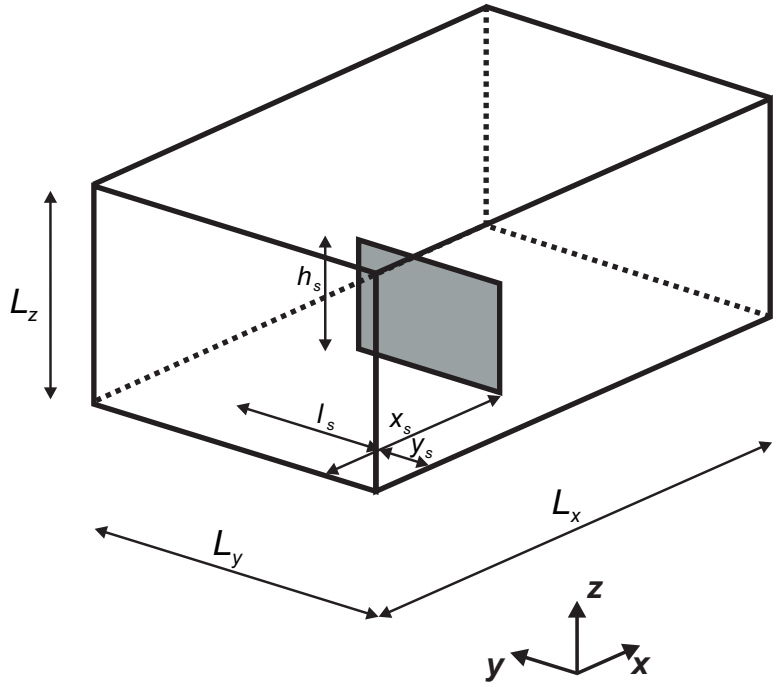

Figure 4.33: The coupling of a 3d fluid with a 2d radiating structure

The full coupled system had 7791 DOFs.

In this example the goal was to check if the *MCM approach* can also be used in 3d FSI problems for determination of the eigenvalues of the coupled system.

Figure 4.34 shows exemplarily chosen 3 attachment modes in fluid. The attachment modes were calculated by applying at the interface the vibration pattern of the structure that is clamped at the bottom. They are calculated as a quasi-static modes with a circular frequency $\omega = 1\frac{rad}{s}(\frac{L_x}{\Lambda_f} \approx 0,001)$.

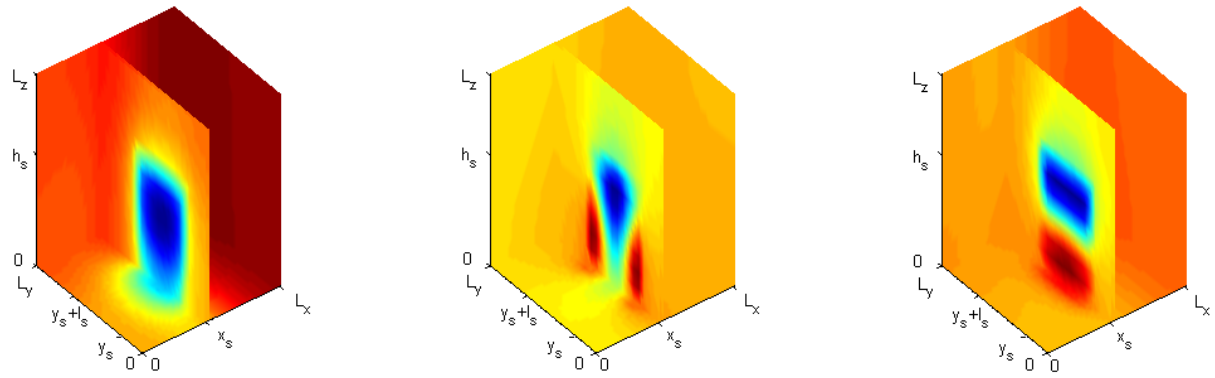

Figure 4.34: Attachment modes for the 3d FSI problem

Figure 4.35 shows that the reduced model is a good approximation of the full system for the calculation of the first 40 eigenvalues of the coupled system. It can be noticed that there is no significant deviation from the exact solution if all normal modes up to the frequency of interest are taken into account. Dashed line in the figure shows the analytical solution for the fluid cavity without the plate. For all the curves in the figure the ordinate shows the number of eigenmode and the abscissa gives the eigenvalue ω_n normalized with respect to the first eigenvalue of the coupled system ω_1. Through the application of the *MCM approach* the calculation time is significantly reduced.

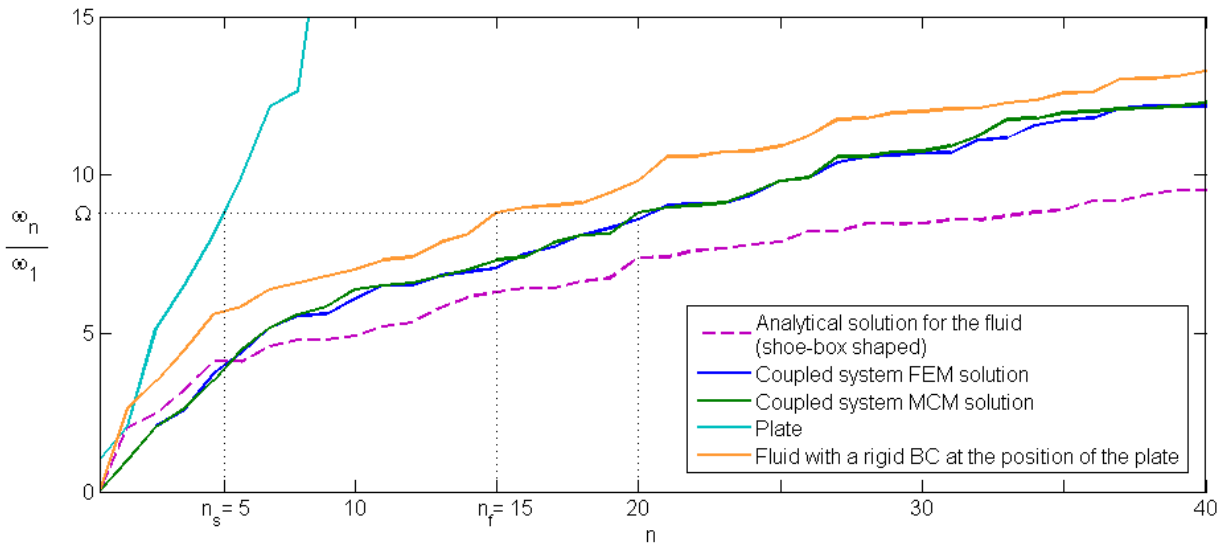

Figure 4.35: Eigenvalues ω_n of a 3d coupled and decoupled FSI system and analytical solution for the fluid cavity; The full FEM solution (blue line) and the approximated solution obtained by applying the MCM approach (green line)

The light blue and the orange curve in figure 4.35 show the eigenvalues of the structure and the fluid when the system is decoupled. It can be seen that in the coupled system for a certain frequency Ω the number of the eigenvalues equals the sum of the numbers of the eigenvalues in the fluid and in the structure $(n_f + n_s)$.

Figure 4.36 shows exemplary two pressure normal modes of the coupled system. Figure 4.36 *a*) shows the normal mode in which the vibrations of the fluid are dominating and figure 4.36 *b*) shows the normal mode of the coupled system in which the vibrations of the structures are dominant.

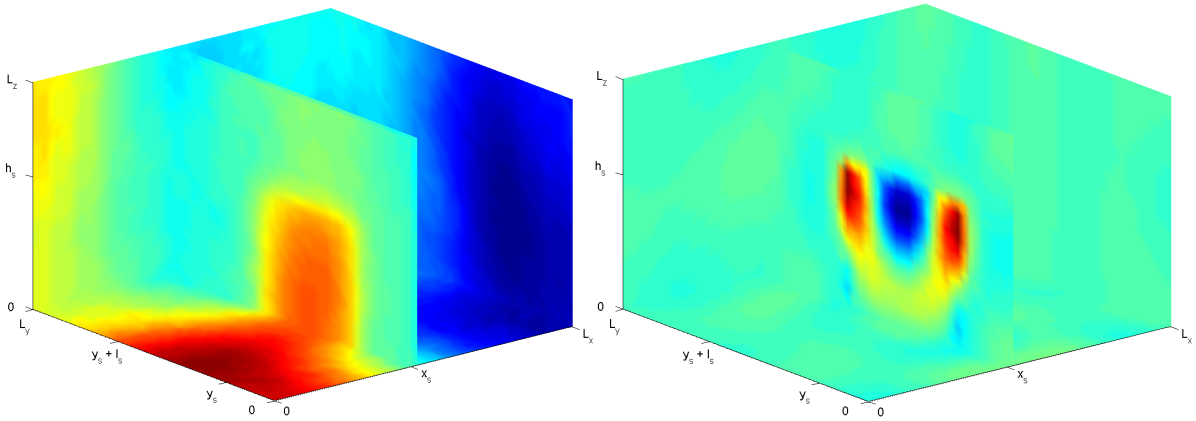

(a) **(b)**

Figure 4.36: Normal modes of the 3d coupled system

5 Acoustic Measurements

5.1 Introduction

Acoustic measurements are an inseparable part of acoustic analysis in both research and practical application. In this chapter the measurements performed in collaboration with the company Müller-BBM will be described. Afterwords, the measurement results will be compared with the simulation results obtained from the methods described in chapter 4.

5.2 Measured Variables

The most commonly measured variables in acoustics are sound pressure, velocity, acceleration, sound intensity and sound power [Müller and Möser 2004], [Kohlrausch 1955]. Those variables can be divided in two categories: field variables (pressure, velocity and acceleration) and performance variables (intensity and power). Only field variables can be measured directly while performance variables need to be determined indirectly. Additionally to the variables already mentioned, other derived values such as the absorption coefficient, impedance or reflection coefficient can also be determined.

The basic equipment for all acoustical measurements consists of a sending part (or an existing sound source) and a receiving part. A signal is generated in the emitter and registered at the receiver which can be a sound-level-meter or an analyzer depending on the characteristic we want to measure [Heckl and Müller 1994].

5.3 Measurement of Transfer Functions and Impulse Response Functions

The Impulse Response Function (IRF) is the response of a system on a Dirac impulse and is used for characterization of a linear time-invariant (LTI) system in systems theory. The response of the system on external loading is defined as:

$$u_k(t) = \int_{t_0}^{t} g_{kl}(t-\tau)p_l(\tau)d\tau \qquad \text{for} \qquad t > t_0 \tag{5.1}$$

Here $u_k(t)$ denotes the response in point k due to the loading $p(t)$ in point l. For $t < t_0$ the LTI system is in the stationary state of rest ($p_l(t) \equiv 0$), [Natke 1983].

The response in frequency domain is obtained through a Fourier transformation of equation (5.1):

$$FT\left\{u_k(t)\right\} = FT\left\{\int_{-\infty}^{\infty} g_{kl}(t-\tau)p_l(\tau)d\tau\right\}. \tag{5.2}$$

Considering that for $t < t_0 \rightarrow p_l(t) \equiv 0$ and for $t < 0 \rightarrow g_k l(t) \equiv 0$ equation (5.2) becomes:

$$FT\left\{u_k(t)\right\} = FT\left\{\int_{t_0}^{t} g_{kl}(t-\tau)p_l(\tau)d\tau\right\}. \tag{5.3}$$

If we introduce that:

$$F_{kl}(i\omega) := FT\left\{g_{kl}(t)\right\} \qquad \text{and} \qquad P_l(i\omega) := FT\left\{p_l(t)\right\} \tag{5.4}$$

and remember that convolution in time domain corresponds to multiplication in frequency domain we can rewrite equation (5.2):

$$U_k(i\omega) := FT\left\{u_k(t)\right\} = F_{kl}(i\omega)P_l(i\omega) \tag{5.5}$$

The transfer function $F_{kl}(i\omega)$ is the response in frequency domain in point k on a unit force in point l.

The IRF represents a response of a room on an infinitely short acoustical impulse (Dirac impulse). However, in practice it is not possible to produce a perfect impulse so a signal that is very short in comparison to the impulse response is used as an approximation of

an impulse. Significant problem for the application of an impulse as excitation is that it is necessary to have a strong signal in order to assure the needed signal-noise ratio over the whole frequency range. Often such a strong short signal will bring a system into a nonlinear regime and the assumption that the measured system is LTI will not be valid.

In practice the IRF is detected with a help of correlation method which allows better signal-noise ratio.

5.3.1 Signal processing - Correlation Measurement Technique

In this work sweeps were used as excitation signal for the measurements and in order to obtain transfer functions of the system the signal processing had to be applied. Basic terms of Correlation Measurement Technique will now be defined [Möser 2010], [Kiencke and Eger 2005], [Natke 1983].

The Cross Correlation Function

In signal processing, cross correlation is a measure of similarity of two different time signals $p(t)$ and $u(t)$. In this measurement those two signals are the input and the output signal. For continuous functions the cross correlation is defined as:

$$\Phi_{pu}(t) = \int_{-\infty}^{\infty} p^*(\tau)u(t+\tau)d\tau. \tag{5.6}$$

and p^* stands for complex-conjugate of p.

For discrete functions the cross correlation is calculated from:

$$\Phi_{pu}(n) = \sum_{m=-\infty}^{\infty} p^*(m)u(n+m). \tag{5.7}$$

The Auto Correlation Function

The auto correlation function is a cross correlation of a signal with itself. It describes the correlation between the values of the process at different points in time. For continuous

functions the auto correlation is defined as:

$$\Phi_{pp}(t) = \int_{-\infty}^{\infty} p^*(\tau)p(t+\tau)d\tau = \int_{-\infty}^{\infty} p^*(\tau+t)p(\tau)d\tau. \tag{5.8}$$

The discrete auto correlation at lag j is:

$$\Phi_{pp}(j) = \sum_{n=-\infty}^{+\infty} p^*(n)p(n+j). \tag{5.9}$$

The Power Spectrum

The correlation functions give information about the power of the process. In order to obtain information about the power in the frequency domain a Fourier transformation of the correlation function is needed.

The Cross power spectrum is a Fourier transformation of cross correlation function:

$$S_{pu}(\omega) = \int_{-\infty}^{\infty} \Phi_{pu}(\tau)e^{-i\omega\tau}d\tau. \tag{5.10}$$

and analogously auto power spectrum is a Fourier transformation of auto correlation function:

$$S_{pp}(\omega) = \int_{-\infty}^{\infty} \Phi_{pp}(\tau)e^{-i\omega\tau}d\tau. \tag{5.11}$$

The connection between these functions is presented in figure 5.1.

5.3.2 Measurement methods

Through decades many methods for measuring IRF and TF have been developed [Müller and Massarani 2001], [Müller and Möser 2004], [DIN 2006–08] . Common goal for all of those methods is that they should ideally have an excitation signal that contains all frequencies of interest. Moreover, the signal power should be higher than the power of the background noise. The ratio between the power of the signal and the power of the background noise is called signal-to-noise ratio (S/N ratio). There are three basic types of the excitation signals: impulse, noise and sweep.

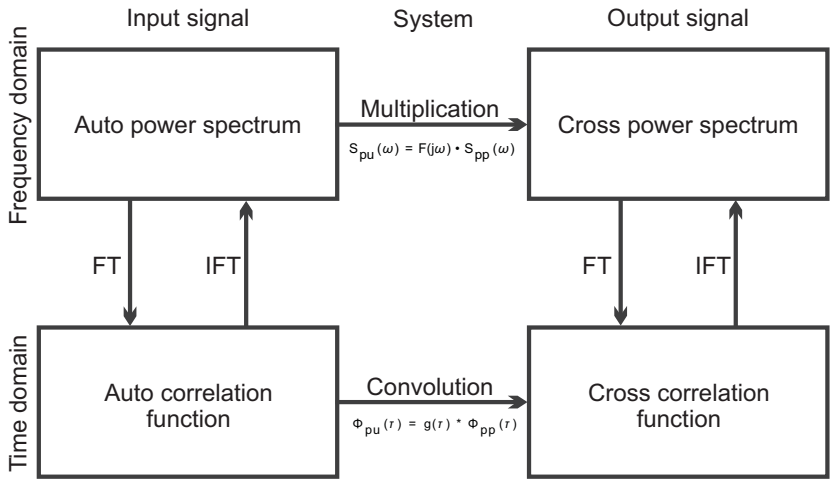

Figure 5.1: Overview diagram

The Impuse-Based Measurements

Using impulses as input signal is the most straight-forward method for measuring the IRF and the captured response is already the desired result. In order to be able to stimulate the acoustical system the impulse needs to be strong enough. By using periodically repeated impulses it is possible to improve the signal-to-noise ratio, but the period between two impulses needs to be long enough that the measured response has time to decay below the background noise level. This method can be applied only in cases when the level of background noise is low but one has to be aware of possible entering in the non-linear range of the loudspeaker due to the strength of the signal.

The Noise-Based Measurements

In measurements with noise signal usually a Dual-Channel FFT-Analysis is used. The basic principle of this method is to divide the spectrum of the output with the one from input signal. In general, any signal of the length 2^m can be used. Therefore the input signal in the dual-channel analyzers can be a non-deterministic noise signal whose spectrum is not known and therefore also needs to be captured, [Müller and Massarani 2001]. The quality of results obtained by using such signals are strongly dependent on the frequency band of the signal and the achieved signal-to-noise ratio. Usage of pink and white noise signals is also possible. Due to the fact that the loud speakers are more sensitive in the high frequency range, which

can cause distortions, the usage of pink noise can be more convenient compared to white noise.

The biggest shortage of these signals are large oscillations of the amplitudes which might occur in almost every analysis interval which can result in insufficient signal-to-noise ratio for single frequencies. Moreover, for comparison of the results one needs to be aware that the time sequence and crest factor of the noise signal can vary, [Möser 2010]. Crest factor marks the ratio between the maximal and mean amplitude of the signal.

The Maximum Length Sequences (MLS) use a periodical binary pseudo stochastic noise signal whose autocorrelation function comes very close to Dirac impulse which simplifies the determination of the IR function in the time domain. When using MLS, much more energy can be introduced into the system because the signal is stretched over a longer time-period.

The signal sequence is characterized by the order of the sequence m which is a positive whole number and it defines the number of samples $L = 2^m - 1$. The samples are members of a binary sequence and they can take the value 1 or 0. The case when all samples take the value 0 is excluded. The sequence of binary values is obtained through a deterministic process which is described in [Möser 2010].The autocorrelation function of the signal obtained in this process is periodic and the amplitude and the period equal the length of the sequence L. The IR of the system is determined through the correlation function between the signal sequence and the measured response.

In this method it is not always possible to make a clear difference between the response from the excitation signal and from background noise, especially when the background noise contains random clicks and pops because it will not be possible to separate them from the noise input signal. Even when the background noise level is low, the quality of the received IR can not be guaranteed for the following reasons: due to the fast switching from the maximal to the minimal values the loudspeaker can produce distortion and when the noise is used as excitation signal it is hard to differentiate the distortion products because they will be noise-like distributed over the whole impulse response period. Moreover, periodic noise sequences are extremely sensitive to any time variance.

The Sweep-Based Measurements

Using sweeps as excitation signal can remove a significant part of these limitations. Firstly, sweep-based measurements are less sensitive to time variance because the noise-based measurements require averaging over longer time period. Furthermore, a much more favorable

signal-to-noise ratio can be achieved while all harmonic distortions are removed and hence sweeps can be emitted with much more power, [DIN 2006–08].

Nowadays most commonly used sweep-based measurements include linear and logarithmic sweeps. The linear sweep emits the same energy in each frequency band and corresponds to white spectrum. In case of a logarithmic sweep, the energy in an octave band is staying constant and the sweep has a pink spectrum. In these measurements the logarithmic sweep has been used.

The capture period for recording the system response needs to be as much longer than the excitation signal as the response needs to decline under the background noise level. A low background noise level is a prerequisite for successful measurements. Since sweep signals start with low frequencies whose responses need the longest time to decay, there is enough time to catch all the components while sweeping through higher frequencies and therefore, the capture period is just slightly longer than the excitation signal itself.

The IR function can be obtained through the direct deconvolution or by applying the spectral division of the response spectrum and the excitation spectrum.In this work the spectral division is used and this method is presented graphically in figure 5.2.

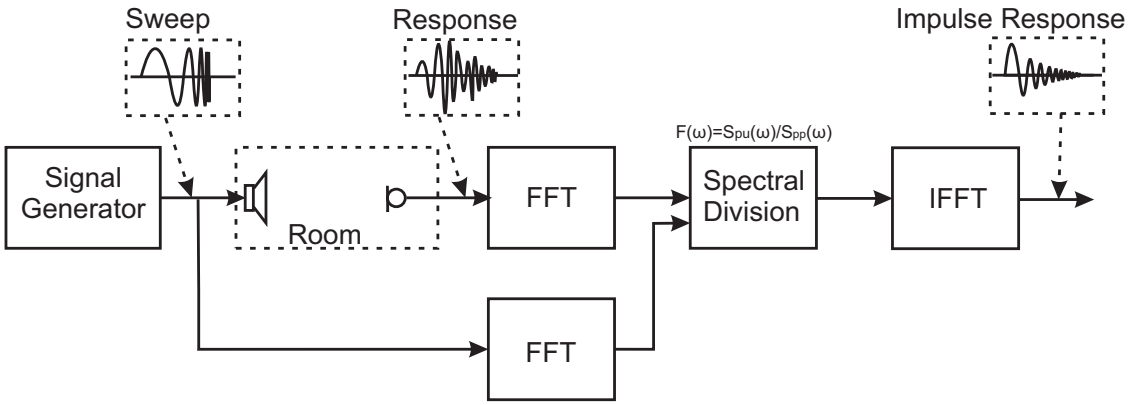

Figure 5.2: Graphical description of the method for determination of an impulse response [DIN 2006–08]

5.4 Measurement of Absorption coefficient in Kundt's tube

The determination of the impedances or absorption coefficient is possible with any method that is separating incident and reflected waves. Therefore, the method for measuring the impulse response described in 5.3 can be applied here.

For determination of absorption coefficients for perpendicular waves it is necessary to create plane waves. Plane waves can be excited in an one dimensional continuum which is created inside of Kundt's tube. One can expect the plane waves inside of the Kundt's tube as long as the cross-section dimensions are smaller than the wave length, see equation (5.21).

The Kundt's tube needs to be straight with constant cross-section and to have rigid, smooth and non-porous walls. The walls need to be rigid and thick enough so they are not excited to oscillation by the sound signal and they do not have eigenvalues in the tube's operating frequency range. The instructions for building an impedance tube are given in [DIN 2001–10].

The theoretical principle for calculation of the impedance and absorption coefficient is given in [DIN 2001–10], [Cremer and Müller 1976], [Beranek 1988] and [Möser 2007]. Figure 5.3 shows the geometry of the Kundt's tube and positions of the microphones.

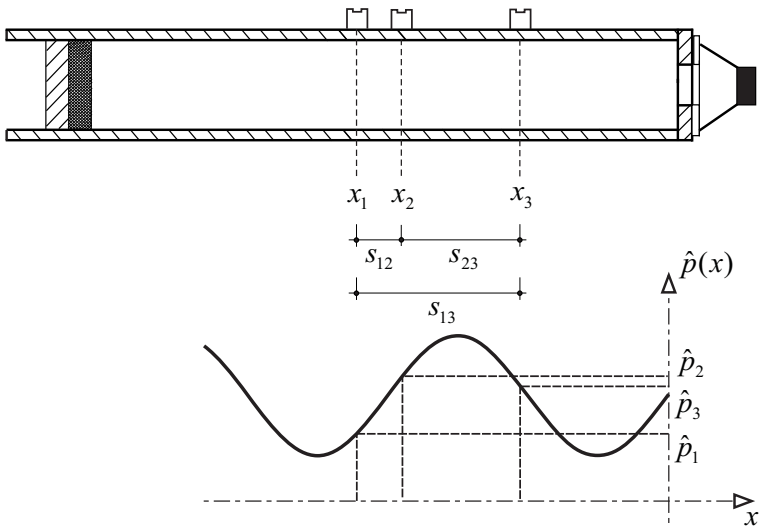

Figure 5.3: Kundt's tube geometry, compared to [DIN 2001–10]

The measurement of absorption and impedances is based on the knowledge that the reflexion coefficient can be determined from the transfer function between two microphones on the front side of the test sample.

The measured sound pressure spectra $\widehat{p}_1(f)$ and $\widehat{p}_2(f)$ at the positions 1 and 2 of the microphones is:

$$\begin{aligned} \widehat{p}_1 &= p_{1I} + p_{1R} = \widehat{p}_I e^{ikx_1} + \widehat{p}_R e^{-ikx_1} \\ \widehat{p}_2 &= p_{2I} + p_{2R} = \widehat{p}_I e^{ikx_2} + \widehat{p}_R e^{-ikx_2}, \end{aligned} \tag{5.12}$$

where p_I marks the incident wave, p_R the reflected wave and k is a wave number, $k = \frac{\omega}{c_0}$.

The transfer function between measurement positions 1 and 2 is defined as:

$$\begin{aligned} \widehat{H}_{12} = \frac{\widehat{p}_2}{\widehat{p}_1} &= \frac{e^{ikx_2} + \widehat{r}e^{-ikx_2}}{e^{ikx_1} + \widehat{r}e^{-ikx_1}} \\ &= \frac{e^{ik(x_1+s_{12})} + \widehat{r}e^{-ik(x_1+s_{12})}}{e^{ikx_1} + \widehat{r}e^{-ikx_1}}. \end{aligned} \tag{5.13}$$

Here $s_{12} = x_2 - x_1$ and marks the distance between two microphones.

The transfer function of the incident wave is:

$$\widehat{H}_I = \frac{\widehat{p}_{2I}}{\widehat{p}_{1I}} = e^{ik(x_2-x_1)} = e^{iks_{12}} \tag{5.14}$$

and the transfer function of the reflected wave is:

$$\widehat{H}_R = \frac{\widehat{p}_{2R}}{\widehat{p}_{1R}} = e^{-ik(x_2-x_1)} = e^{-iks_{12}}. \tag{5.15}$$

Solving equation (5.13) for $\widehat{r}$ gives:

$$\widehat{r} = e^{i2kx_1} \frac{e^{iks_{12}} - \widehat{H}_{12}}{\widehat{H}_{12} - e^{-iks_{12}}}, \tag{5.16}$$

and after introducing equations (5.14) and (5.15) reflection coefficient is given by:

$$\widehat{r} = e^{i2kx_1} \frac{\widehat{H}_I - \widehat{H}_{12}}{\widehat{H}_{12} - \widehat{H}_R}. \tag{5.17}$$

The absorption coefficient and impedance ratio can be calculated from reflection coefficient using:

$$\alpha = 1 - \left|\widehat{r}\right|^2, \tag{5.18}$$

$$\widehat{Z} = \frac{1 + \widehat{r}}{1 - \widehat{r}}, \tag{5.19}$$

In practice, the measurements are often done with one microphone. The measurement is typically repeated three times while the microphone is taking three different positions according to figure 5.3. The transfer functions between all three positions are calculated afterwards.

$$\widehat{H}_{12} = \frac{\widehat{p}_2}{\widehat{p}_1} \qquad \widehat{H}_{13} = \frac{\widehat{p}_3}{\widehat{p}_1} \qquad \widehat{H}_{23} = \frac{\widehat{p}_3}{\widehat{p}_2} \tag{5.20}$$

For each of those three couples the transfer functions for incident and reflected waves will be calculated as well as the corresponding reflection coefficient. At the end the absorption coefficient and the impedance are calculated using the mean reflection coefficient.

The measurement setup is presented in figure 5.4.

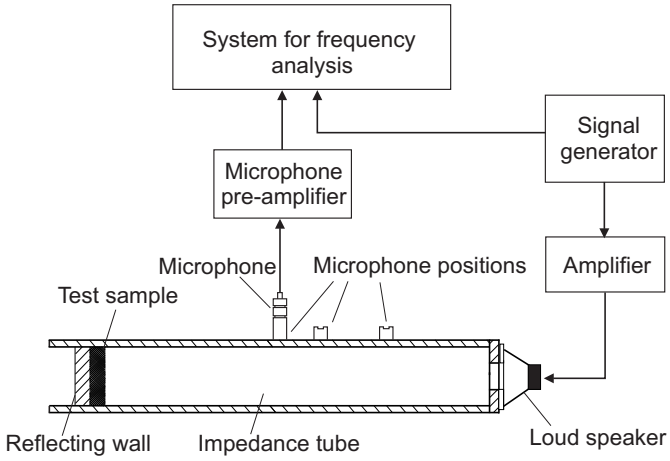

Figure 5.4: Measurement set up in Kundt's tube, compared to [DIN 2001–10]

The measurements can be carried out up to the frequency where the first transverse mode in the tube arises. That frequency, marked with f_u for the tube with square cross-section with the edge length d and the speed of sound c_0 is determined from:

$$f_u = 0,5\frac{c_0}{d}. \tag{5.21}$$

Kundt's tube was used in [Paolini 2010], where absorption coefficients and impedances of melamine foam, polyurethane foam and mineral-fibers were measured and the results were compared with analytical and numerical solutions that were obtained in [Buchschmid et al 2009a] and [Buchschmid et al 2009b].

In this work the measurements in Kundt's tube were done on the compound absorber with a slot that consists of a foam material and a plate. The position of the slot was altered from a slot in the front plate to a slot in the side frame and finally to a slot between the absorber and the back wall. This sort of absorber was not possible to simulate with an ITM-TPM based model because this method allows the changes in the absorber only in the direction

perpendicular to the cross-section plane and here the changes also appeared in cross-section itself.

The measured impedance is used to calculate the analytical solution for a 1D fluid. The length of the fluid is L, the measured impedance is applied at the position $x = 0$ and at the open end at $x = L$ the harmonic loading is acting. The reference solution for the pressure inside of the fluid in frequency domain, similar to (5.12), is given by:

$$\widehat{p} = p_I + p_R = \widehat{p}_I e^{ikx} + \widehat{p}_R e^{-ikx}. \tag{5.22}$$

The incident and the reflected wave at the boundaries have the following values:

$$\begin{array}{rclcrclcl} p_I & = & \widehat{p}_I & \text{and} & p_R & = & \widehat{p}_R & \text{for} & x = 0 \\ p_I & = & \widehat{p}_I e^{ikL} & \text{and} & p_R & = & \widehat{p}_R e^{-ikL} & \text{for} & x = L \end{array} \tag{5.23}$$

Therefore the reference pressure (5.22) at the boundaries becomes:

$$\begin{array}{rcll} \widehat{p} & = & \widehat{p}_I + \widehat{p}_R & \text{for} \quad x = 0 \\ \widehat{p} & = & \widehat{p}_I e^{ikL} + \widehat{p}_R e^{-ikL} & \text{for} \quad x = L \end{array} \tag{5.24}$$

The application of the impedance boundary condition will now be explained. If in equation (5.19) the reflection coefficient is introduced as the ratio between the amplitudes of the reflected wave and the incident wave at the position $x = 0$ ($\widehat{r} = \frac{\widehat{p}_R}{\widehat{p}_I}$), the following expression for the impedance is obtained:

$$\widehat{Z} = \frac{\widehat{p}_I + \widehat{p}_R}{\widehat{p}_I - \widehat{p}_R}. \tag{5.25}$$

From equation (5.25) the following ratio of the reflected and the incident wave is obtained:

$$\frac{\widehat{p}_R}{\widehat{p}_I} = \frac{\widehat{Z} - 1}{1 + \widehat{Z}}. \tag{5.26}$$

From equation (5.26) the impedance boundary condition is obtained:

$$(\widehat{Z} - 1)\widehat{p}_I - (1 + \widehat{Z})\widehat{p}_R = 0 \qquad \text{for} \qquad x = 0. \tag{5.27}$$

At the position $x = L$ a harmonic load $f = p_0 e^{i\omega t}$ is acting and the boundary condition for the steady-state solution is:

$$\widehat{p}_I e^{ikL} + \widehat{p}_R e^{-ikL} = p_0 \qquad \text{for} \qquad x = L. \tag{5.28}$$

Equations (5.27) and (5.28) can also be written in matrix notation:

$$\begin{bmatrix} (\widehat{Z}-1) & -(\widehat{Z}+1) \\ e^{ikL} & e^{-ikL} \end{bmatrix} \begin{bmatrix} \widehat{p}_I \\ \widehat{p}_R \end{bmatrix} = \begin{bmatrix} 0 \\ p_0 \end{bmatrix} \tag{5.29}$$

The analytical solution for a harmonically excited fluid with the totally reflective boundary condition at position $x = 0$ and for a fluid with an absorber at the position $x = 0$ is given in figure 5.5. Figure 5.6 shows the normalized absolute value of the impedance $Abs(\widehat{Z}/Z_0)$ of the absorber shown in figure 5.5 left. Here Z_0 marks the characteristic acoustic impedance of the air.

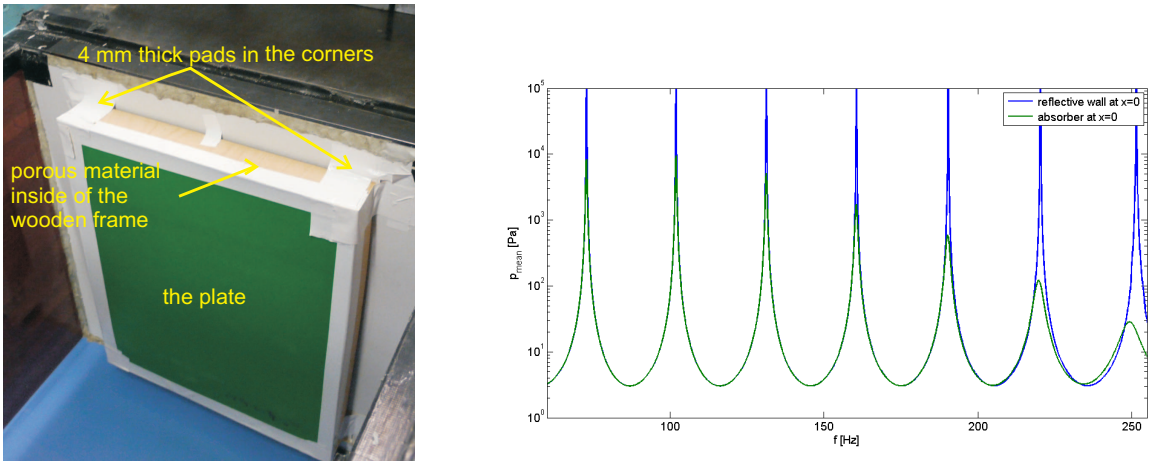

Figure 5.5: The absorber inside of Kundt's tube (left) and the analytical solution for the sound pressure level in harmonically excited fluid with totally reflective boundary condition at position $x = 0$ and for a fluid that has an absorber at position $x = 0$ (right)

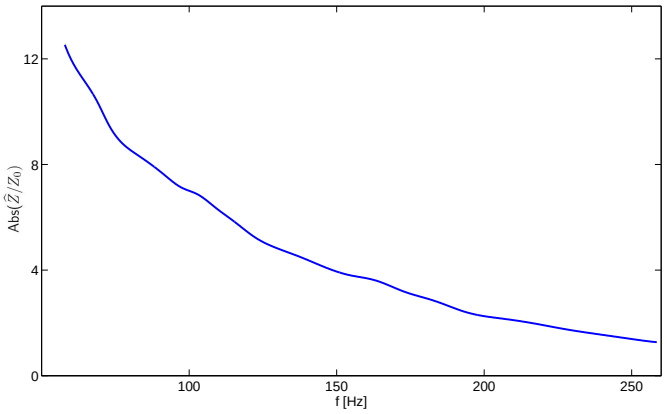

Figure 5.6: Normalized absolute value of the impedance of the absorber shown in figure 5.5 left

In the numerical method the impedance boundary condition will be introduced as additional damping and stiffness or mass matrix members. In figure 5.7 a numerical model of a 1d fluid with an impedance boundary condition on the left-hand side and a harmonic load acting on the right-hand side is shown. The node in which the impedance boundary condition is applied is marked with L, R stands for the node in which the harmonic load is acting and I mark internal nodes.

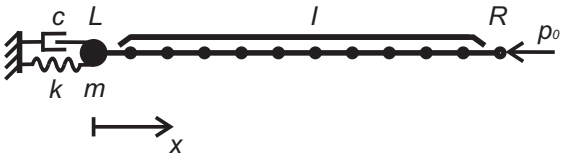

Figure 5.7: Numerical model of a 1d fluid with an impedance boundary condition on the left-hand side and a harmonic load acting on the right-hand side.

If the damping in the system is neglected, the system's dynamic stiffness matrix K^* in the frequency domain is calculated from:

$$\mathbf{K}^* = \mathbf{K} - \Omega^2 \cdot \mathbf{M} \tag{5.30}$$

where Ω marks the frequency of excitation. The damping is only introduced at the boundary.

Now, with a help of the equation (3.19) the equation of motion for the fluid shown in figure 5.7 can be written as:

$$\begin{bmatrix} \mathbf{K}^*_{LL} & \mathbf{K}^*_{LI} & \mathbf{K}^*_{LR} \\ \mathbf{K}^*_{IL} & \mathbf{K}^*_{II} & \mathbf{K}^*_{IR} \\ \mathbf{K}^*_{RL} & \mathbf{K}^*_{RI} & \mathbf{K}^*_{RR} \end{bmatrix} \begin{bmatrix} \mathbf{p}_L \\ \mathbf{p}_I \\ \mathbf{p}_R \end{bmatrix} = \begin{bmatrix} \mathbf{F}_L \\ \mathbf{0} \\ \mathbf{F}_R \end{bmatrix}. \tag{5.31}$$

The right-hand side of the equation (5.31) is defined in chapter 3.1.2 as the projection of the pressure gradient on the normal of the boundary $\mathbf{F}_L = \nabla \mathbf{p}_L$. The law of inertia gives the relationship between the pressure gradient and the fluid velocity:

$$\nabla \mathbf{p}_L = -\rho_0 \frac{\partial \mathbf{v}_L}{\partial t}. \tag{5.32}$$

The same can be written in the frequency domain:

$$\nabla \mathbf{p}_L = \rho_0 \Omega \mathbf{v}_L. \tag{5.33}$$

The boundary conditions for the numerical model are:

$$\begin{array}{rcll} \frac{\mathbf{p}_L}{\mathbf{v}_L} & = & \mathbf{Z}_L & \text{for} \quad x = 0, \\ \mathbf{p}_R & = & \mathbf{p}_0 & \text{for} \quad x = L. \end{array} \tag{5.34}$$

If the first boundary condition is introduced in equation (5.32) the value $\nabla \mathbf{p}_L$ can be determined as:

$$\nabla \mathbf{p}_L = \rho_0 \Omega \mathbf{v}_L = \rho_0 \Omega \frac{\mathbf{p}_L}{\mathbf{Z}_L}. \tag{5.35}$$

After introducing the boundary conditions into equation (5.31) we obtain:

$$\begin{bmatrix} \mathbf{K}^*_{LL} & \mathbf{K}^*_{LI} & \mathbf{K}^*_{LR} \\ \mathbf{K}^*_{IL} & \mathbf{K}^*_{II} & \mathbf{K}^*_{IR} \\ \mathbf{K}^*_{RL} & \mathbf{K}^*_{RI} & \mathbf{K}^*_{RR} \end{bmatrix} \begin{bmatrix} \mathbf{p}_L \\ \mathbf{p}_I \\ \mathbf{p}_0 \end{bmatrix} = \begin{bmatrix} \rho_0 \Omega \frac{\mathbf{p}_L}{\mathbf{Z}_L} \\ \mathbf{0} \\ \nabla \mathbf{p}_R \end{bmatrix}. \tag{5.36}$$

Using equation (5.36) the sound pressure $\mathbf{p}$ in Kundt's tube can be determined.Figure 5.8 shows the numerical and analytical solution for a 1D-fluid with the impedance boundary condition at x=0 and harmonic excitation at x=L.

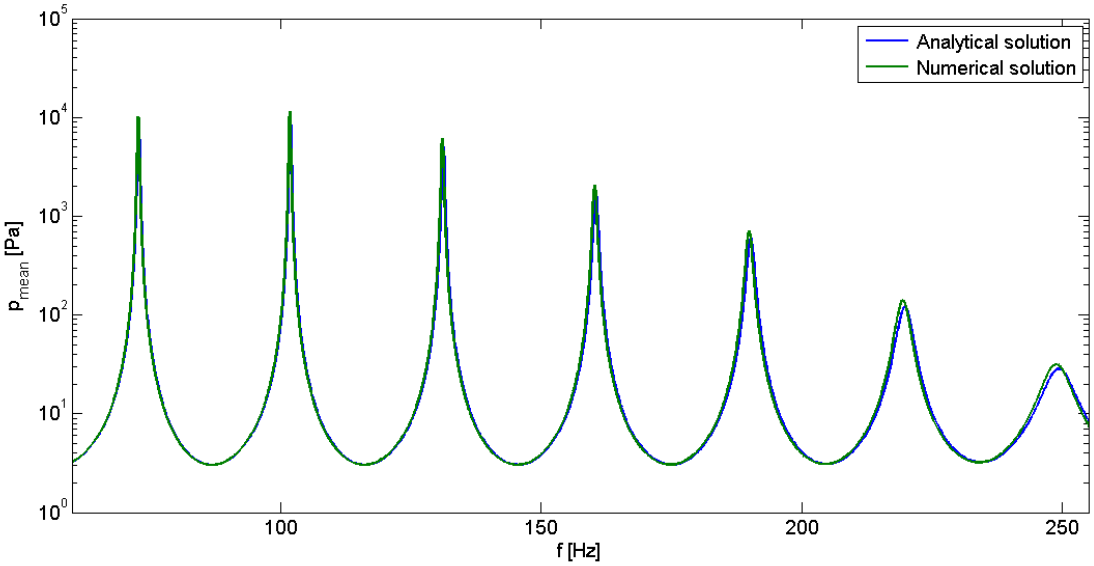

Figure 5.8: Numerical and analytical solution for 1d fluid with impedance boundary condition at x=0 and harmonic excitation at x=L

5.5 Measurement of the sound pressure distribution

The measurements of the sound pressure distribution in a room were performed with the goal to verify the simulation results for the acoustic fluid with a vibrating plate and an absorber at the boundaries. The geometry of the room is presented in figure 5.10.

For measuring the sound pressure distribution in the vertical direction a "microphone tree" (see figure 5.9 left) had been created. It consisted of 10 microphones that have been taped on the stander with a spacing of 27 cm. In the horizontal plane the points where the microphone tree was placed were 20 cm distanced from each other. Due to some additional objects in the room and the size of the stander's basis it was not possible to measure the whole area of the room. The marking of the measurement points in the room is shown on the figure 5.9 right and the position of all measured points can be seen at 5.9.

As the resolution of the measurement points in the vertical direction is smaller than in the horizontal direction, it gives the frequency limit up to which the condition of minimal number of points per wave length will be fulfilled. For a satisfying description of the wave it is recommended to have at least 7 points per one wave length. Since the distance between the microphones in vertical direction is 27 cm, the limit wave length is $\lambda = 1.62m$ and the limit frequency $f = \frac{c}{\lambda} = 212Hz$ where c is the speed of sound and for the temperature of 20°C equals 343 $\frac{m}{s}$.

Figure 5.9: Microphone tree (left) and measurement points (right)

The excitation signal is the sweep described in 5.3.2. The sweep is produced in the sweep generator and it is sent through the amplifier to the loud speaker. The signal that is emitted in the room is captured by microphones. The signal created by the generator and the signal

captured by microphone will be transformed with Fast Fourier Transformation (FFT) into the frequency domain. The sound pressure spectrum is divided by the voltage spectrum and after the Inverse Fourier Transformation (IFFT) of the result, the impulse response function is determined (see figure 5.2). The received IRF can be shortened from the point where the response to the excitation signal turns into background noise.

The impulse response represents the transfer function between the input voltage at the input of the amplifier and the sound pressure at the microphone position. The existence of a frequency-independent sound power level in the combination amplifier-sound source needs to be provided, which implies that impulse response needs to be normalized by the sound power of the sound source.
The measurement equipment consisted of:

- A measured data recording system consisting of PAK software (Müller-BBM VAS) with 10 input channels for sound pressure and one input channel for recording the reference voltage,
- A dodekaedar and power amplifier,
- A signal generator
- Software CalcTransmissionSpeaker (Müller-BBM) for calculation of the source-normalized impulse responses from the data that was recorded by PAK.

In figure 5.11 the pressure distribution in the horizontal cross-section of the room for different frequencies is shown. On the left-hand the calculated results are shown while on the right-hand side the measurement results are presented. It can be noticed that the amplitudes in measured results are lower then in the calculated results. The reason for this can be the fact that, due to the shape of the microphone-tree it was not possible to measure the pressure directly at the boundaries of the room where the sound pressure achieves its maximum.

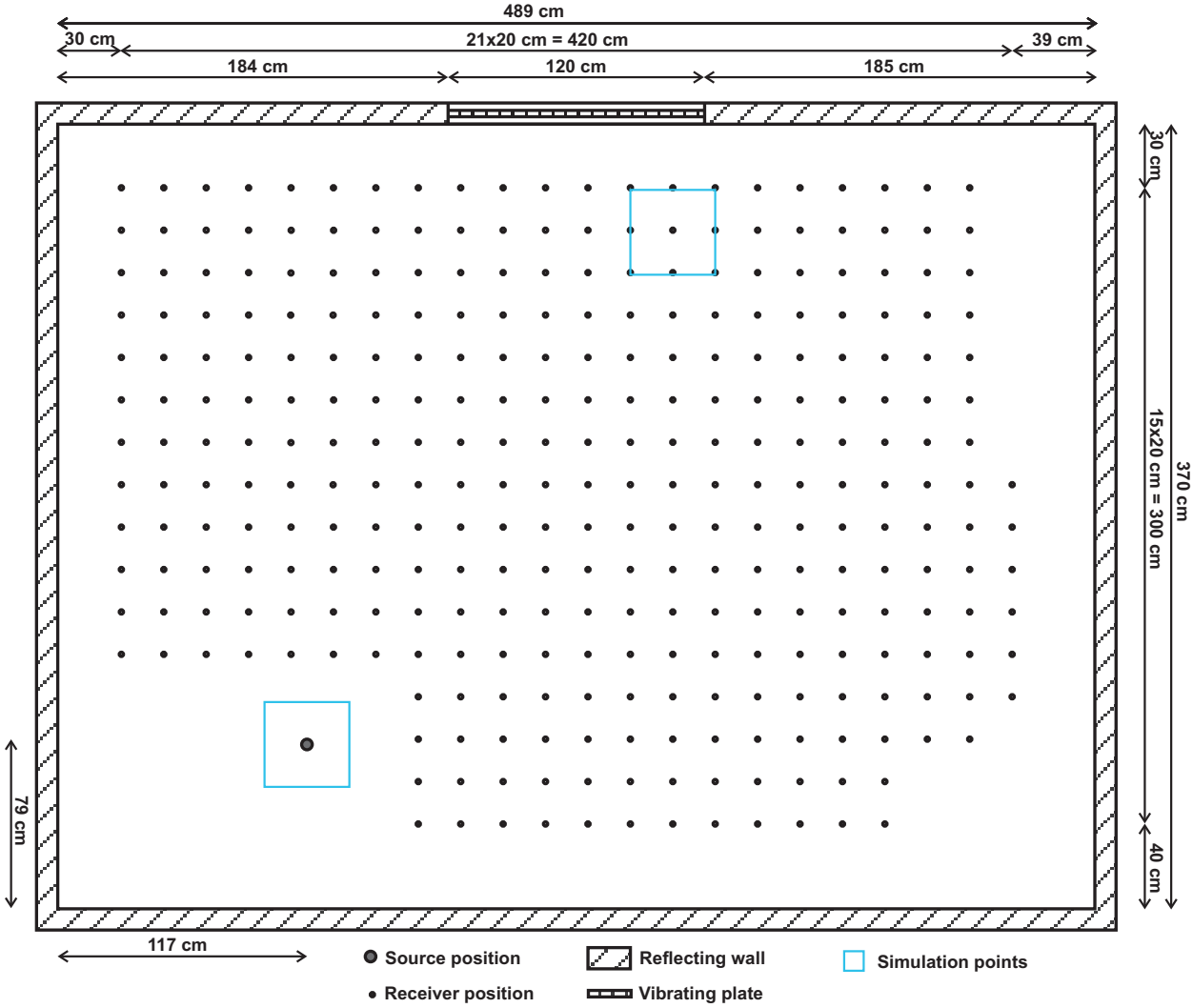

Figure 5.10: Geometry of the measurement room with positions of the sender, receivers and vibrating plate

In the numerical model pressure transfer functions were also calculated and results are compared with measured results. Here presented measured and calculated transfer functions show the pressure value in two points in the room that are close to the vibrating plate. The results are are shown in figure 5.12. It can be seen that the numerical model can be used for determination of the resonances of the coupled system for low frequencies. For higher frequencies, due to high modal density, results become very sensitive to small changes in frequencies or position of the loud speaker and microphones. In order to present the sensitivity of the results for higher frequencies the position of the source and the receiver was slightly varied as well as the frequency and the response is calculated for all combinations. The source and the receiver were taking 9 different positions each inside of the blue rectangle shown in figure 5.10. Frequencies were varied around the second and the third resonant

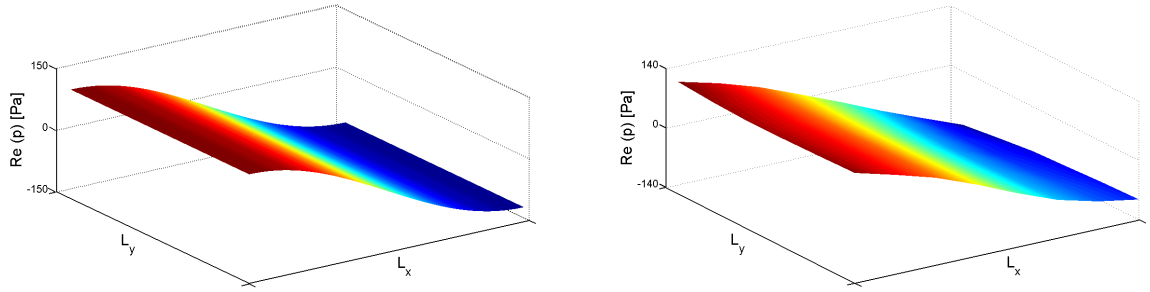

(a) f = 35,27 Hz

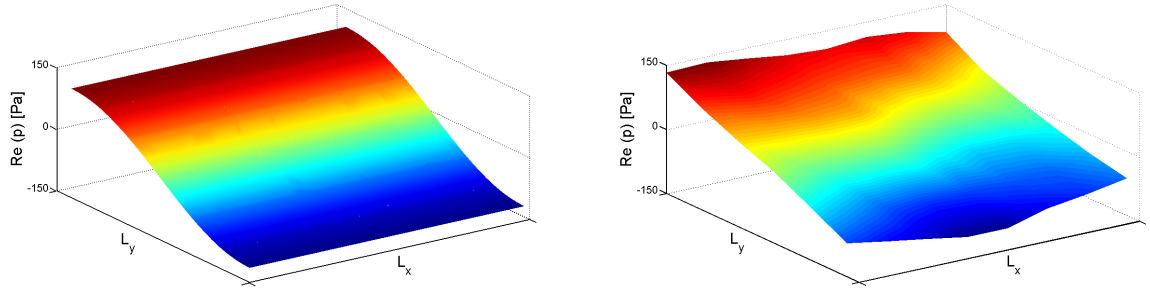

(b) f = 46,61 Hz

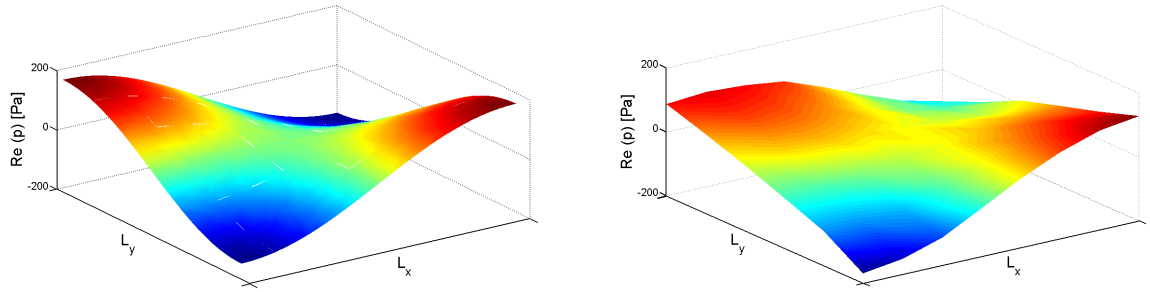

(c) f = 58,45 Hz

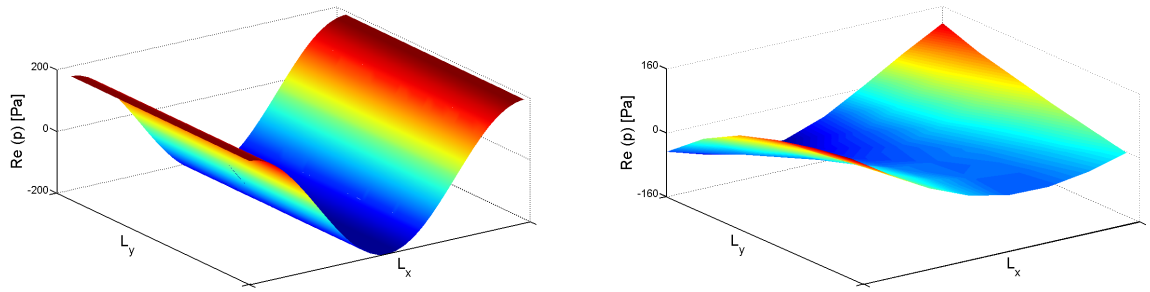

(d) f = 70,54 Hz

Figure 5.11: Calculated (left) and measured pressure (right) for different frequencies.

frequencies of the system in range $\pm 2Hz$.

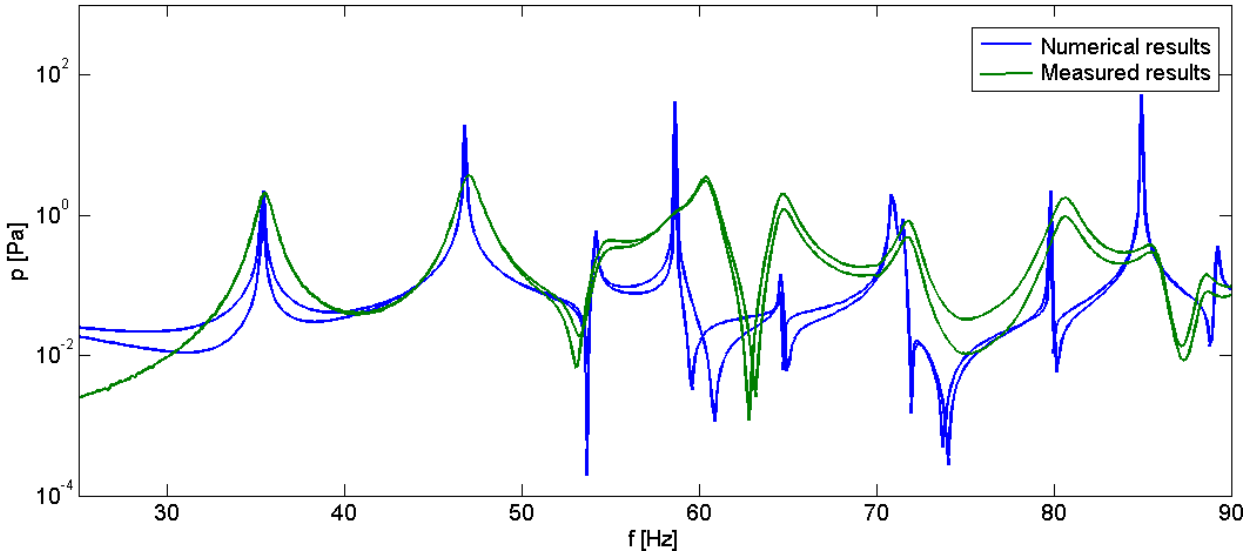

Figure 5.12: Calculated and measured pressure transfer function

Figure 5.13 shows the histograms of the results for two frequency ranges and proves the assumption that the results in higher frequency range become more sensitive. Therefore, averaging in post-processing would be necessary.

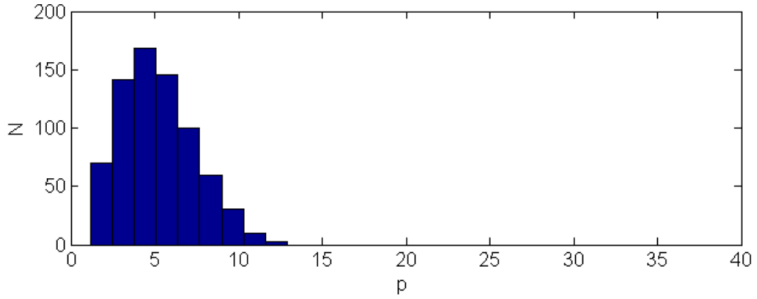

(a) f = 44 - 48 Hz

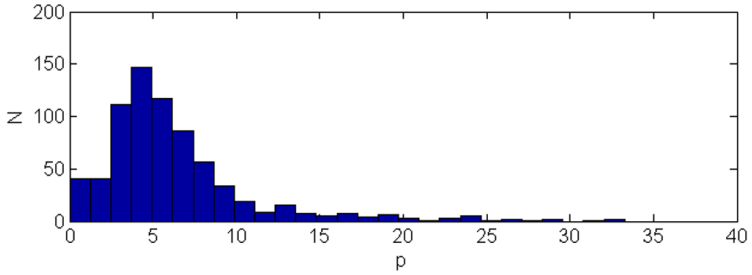

(b) f = 58 - 62 Hz

Figure 5.13: Histograms for frequency ranges 44 - 48 Hz and 58 - 62 Hz

It is assumed that the dispersion of the results in figure 5.13 a) comes from the variation of the frequency and in figure 5.13 b) from the variation of the position of excitation and receiving point. This assumption is proved in figure 5.14 where only the position of excitation and the receiving point were changing and the frequency was constant.

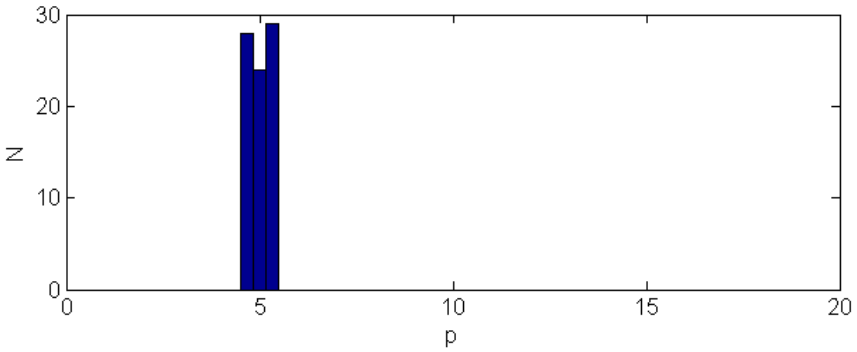

(a) f = 46 Hz

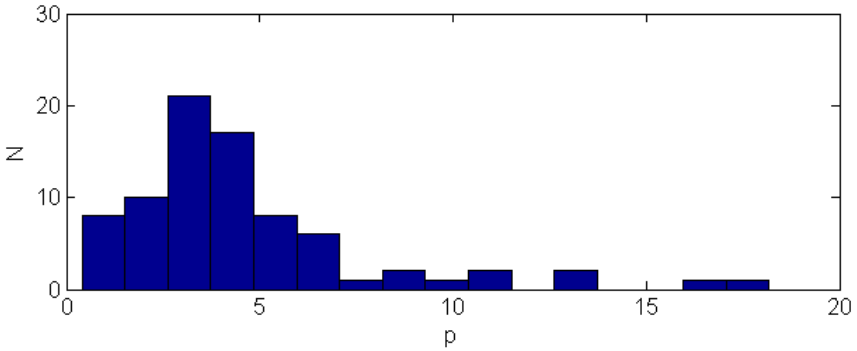

(b) f = 58 Hz

Figure 5.14: Histograms for frequencies 46 Hz and 58 Hz

6 Conclusion

The presented work describes a model reduction method for room acoustical simulations. This thesis begins with the basic equations that describe the motion of the fluid and the structure components in an acoustic cavity. Afterwards a numerical method that is used for solving these equations is given. At this point the problem of the size of the numerical model occurs.

The Craig-Bampton model reduction method based on the Component Mode Synthesis (CMS) is presented as a solution of the problem of the extensive calculations. The acoustic system is separated into its substructures. The division into substructures is performed in a manner that one substructure consists only of fluid or only of solid elements. All the analysis are performed on the substructure level. In the assembly of the model of the full system the substructures are represented by generalized coordinates instead of their natural degrees of freedom (DOFs). The number of generalized coordinates equals the number of normal and attachment modes that are taken into account for the approximation of the substructure. This number is influenced by the frequency range of interest and it is usually much smaller then the number of physical DOFs. The normal modes of all substructures are fixed-interface normal modes. The attachment modes allow the mobility of the interface nodes and they serve for the coupling of the substructures. The Craig-Bampton method is especially suitable for the processes of optimization because the changes in the system can be implemented in the substructure level without the need to change the whole system.

The main difference between the Craig-Bampton method and the *MCM approach* that is introduced in this thesis is the choice of the attachment modes. The traditional Craig-Bampton method uses the nodal attachment modes. These modes are determined by assigning a unit displacement to each interface DOF. Hence, the number of attachment modes equals the number of interface DOFs. In this work it has been shown through a couple of calculation examples that the number of nodal attachment modes can multiple surpass the number of necessary normal modes and therefore reduce the positive effects of the model reduction method. The *MCM approach* that is presented in this thesis suggests the use of so-called

modal attachment modes. These modes are gained by applying a certain displacement pattern at the interface. The shape of the pattern depends on the types of the substructures that are coupled and boundary conditions that the substructures should fulfill at the ends of the common interface. The guidelines for proper choice of the attachment modes are also given in this thesis.

The numerical examples show that the *MCM approach* has approximately the same exactness as the traditional Craig-Bampton method and therefore, it can be used for the approximation of the full FE model. The *MCM approach* has given good results in coupling of several fluid substructures as well as in coupling of fluid and solid structures. Therefore, this method can be used for substructuring of complex geometries and in FSI problems. It has also been shown that the *MCM approach* does not only give the good approximation of the FE model but it also can accelerate the calculation time significantly by reducing the number of unknowns.

A Appendix

A.1 Derivation of the 1d Wave equation

In this appendix a more detailed derivation of the 1d wave equation is given.

For the derivation of the 1d wave equation figure 2.3 will be observed. When the air inside of the tube is moving an inertia force q_i is appearing. The inertia force can be determined with the help of D'Alembert's principle:

$$\begin{array}{rcl} q_i(x,t) & = & -\rho_f \cdot a(x,t) \\ q_i(x,t) \cdot A \cdot dx & = & -\rho_f \cdot A \cdot dx \cdot a(x,t) \end{array} \tag{A.1.1}$$

where $a(x,t)$ marks the acceleration of the air and ρ_f is the density of the air.

The acceleration of the fluid is defined as:

$$a(x,t) = \frac{\partial^2 u_x(x,t)}{\partial t^2} = \frac{\partial v_x(x,t)}{\partial t}. \tag{A.1.2}$$

In (A.1.2) $v(x,t)$ marks the velocity of the fluid and $u_x(x,t)$ is the fluid displacement. For deriving the wave equation, the equilibrium of the forces that are acting on the infinitesimally small part of the fluid (see figure 2.3 b)) needs to be provided [Müller 2010]:

$$p(x,t) \cdot A - p(x+dx,t) \cdot A - q_i(x,t) \cdot dx \cdot A = 0. \tag{A.1.3}$$

After including (A.1.1), equation (A.1.3) becomes:

$$\begin{array}{rcl} p(x,t) \cdot A - p(x,t) \cdot A - \frac{\partial p(x,t)}{\partial x} dx \cdot A - \rho_f(x,t) \cdot dx \cdot A \cdot a(x,t) & = & 0 \\ -\frac{\partial p(x,t)}{\partial x} dx \cdot A - \rho_f \cdot dx \cdot A \cdot a(x,t) & = & 0. \end{array} \tag{A.1.4}$$

The pressure in the fluid is proportional to the strain in fluid ϵ:

$$p(x,t) = -\epsilon_x(x,t) \cdot E. \tag{A.1.5}$$

E stands for the Young's modulus of elasticity of the fluid. The strain in the fluid is defined as a change of length of the fluid:

$$\epsilon_x(x,t) = \frac{\partial u_x(x,t)}{\partial x}. \tag{A.1.6}$$

After inserting (A.1.6) in (A.1.5), pressure in the fluid is defined as:

$$p(x,t) = -\frac{\partial u_x(x,t)}{\partial x} \cdot E. \tag{A.1.7}$$

By using (A.1.7), equation (A.1.4) becomes:

$$\frac{\partial^2 u_x(x,t)}{\partial x^2} \cdot E \cdot dx \cdot A - \rho_f \cdot dx \cdot A \cdot a_x(x,t) = 0. \tag{A.1.8}$$

Substituting (A.1.2) in (A.1.8) gives:

$$\frac{\partial^2 u_x(x,t)}{\partial x^2} \cdot E - \rho_f \cdot \frac{\partial^2 u_x(x,t)}{\partial t^2} = 0. \tag{A.1.9}$$

After deriving equation (A.1.9) with respect to x

$$\frac{\partial^3 u_x(x,t)}{\partial x^3} \cdot E - \rho_f \cdot \frac{\partial^3 u_x(x,t)}{\partial x \partial t^2} = 0 \tag{A.1.10}$$

is received. Now, (A.1.7) can be introduced in (A.1.10):

$$\frac{\partial^2 p(x,t)}{\partial x^2} - \frac{\rho_f}{E} \cdot \frac{\partial^2 p(x,t)}{\partial t^2} = 0. \tag{A.1.11}$$

When the derivative with respect to time t is marked with $\cdot$ and the derivative with respect to the space x is marked with $'$ the equations (A.1.9) and (A.1.11) can be rewritten as:

$$\begin{array}{rcl} u_x'' - \frac{\rho_f}{E}\ddot{u_x} & = & 0 \\ p'' - \frac{\rho_f}{E}\ddot{p} & = & 0 \end{array} \tag{A.1.12}$$

When we introduce the expression for the wave velocity (2.10) in equation (A.1.12) the final for of the 1d wave equation is obtained:

$$\begin{array}{rcl} u_x'' - \frac{1}{c_f^2}\ddot{u_x} & = & 0 \\ p'' - \frac{1}{c_f^2}\ddot{p} & = & 0. \end{array} \tag{A.1.13}$$

A.2 Waves in continuum

A.2.1 Lamé equation

Lamé equation is a differential equations which can describe the displacement or stress fields in continuum for linear, small deformations [Müller 2009]. For obtaining the Lamè equation following relations need to be observed:

$$\sigma^{ij}|_j + Q^i - \rho\ddot{u}^i = 0, \tag{A.2.1}$$

$$\epsilon^{ij} = \frac{1}{2}(u^j|^i + u^i|^j), \tag{A.2.2}$$

$$\sigma^{ij} = 2\mu\epsilon^{ij} + \lambda\epsilon^m_m g^{ij}. \tag{A.2.3}$$

Equation (A.2.1) describes the equilibrium condition for the continuum where σ^{ij} stands for Cauchy stresses tensor, Q^i are volume forces and $\rho\ddot{u}^i$ is D'Alembert's inertia force.

With equation (A.2.2) the kinematic relations between strains and displacements are described. The strain tensor is marked with ϵ^{ij} and u^j marks the displacement field. The displacements are assumed to be small so the elements of higher order are omitted.

The kinematic relations between the stresses and strains for a homogeneous, isotropic and linearly-elastic material are given in equation (A.2.3). Coefficients μ and λ mark the Lamé constants and they can be determined from Young's modulus E and Poisson's ratio ν by using the following expressions:

$$\mu = \frac{E}{2(1+\nu)} \tag{A.2.4}$$

$$\lambda = \frac{E\nu}{(1+\nu)(1-2\nu)}. \tag{A.2.5}$$

The connection between the stresses and displacements is obtained by introducing the equation (A.2.3) in equation (A.2.2):

$$\sigma^{ij} = \mu(u^j|^i + u^i|^j) + \lambda u^m|_m \; g^{ij}. \tag{A.2.6}$$

After introducing (A.2.6) in the equilibrium equation (A.2.1) the Lamé equation is received:

$$\mu u^i|^j_j + (\lambda+\mu)w^j|^i_j + Q^i - \rho\ddot{u}^i = 0. \tag{A.2.7}$$

A.2.2 Solution of the Lamé equation

With a help of Helmholtz principle the Lamé equation can be transformed into wave equations. The displacements field $\mathbf{u}$ is shown as a superposition of the gradient of a scalar potential Φ and the rotation of a vector potential $\mathbf{\Psi}$:

$$u^i = \Phi|^i + \Psi_l|_k \, \epsilon^{ikl} \tag{A.2.8}$$

If we suppose that the loading is acting only at the boundaries the volume forces Q^i will vanish. After introducing the Helmholtz decomposition in Lamé equation one wave equation for the scalar potential and 3 decoupled wave equations for the vector potential are obtained [Müller 2009]:

$$\begin{aligned} \Phi|^j_j - \tfrac{1}{c_p^2}\ddot{\Phi} &= 0 \\ \Psi_i|^j_j - \tfrac{1}{c_s^2}\ddot{\Psi}_i &= 0. \end{aligned} \tag{A.2.9}$$

The wave velocities are marked with c_p and c_s and they equal:

$$c_p = \sqrt{\frac{\lambda + 2\mu}{\rho}} \qquad \text{und} \qquad c_s = \sqrt{\frac{\mu}{\rho}}. \tag{A.2.10}$$

The equation with the scalar potential Φ is the wave equation for a compressional wave which is moving with the velocity c_p and the equations with the vector potential Ψ_i describe the wave equation for shear waves which are spreading with the velocity c_s. The compressional wave is causing the change of volume and the shear waves are causing the change of shape.

List of Figures

Bibliography

[Abdallah 1990] Abdallah, A. A.: *Dynamic Substructuring by the Boundary Flexibility Vector Method of Component Mode Synthesis*, Case Western Reserve University, Ph.D. thesis, 1990

[Aoyama and Yagawa 2001] Aoyama, Y. ; Yagawa, G.: Component mode synthesis for large-scale structural eigenanalysis. In: *Computers and Structures* 79 (2001), p. 605–615

[Babuška et al 1997a] Babuška, I. ; Ihlenburg, F. ; Strouboulis, S.K.: A Posteriori Error Estimation for Finite Element Solutions of Helmholtz' Equation. Part II: Estimation of the Pollution Error. In: *International Journal for Numerical Methods in Engineering* 40 (1997), Nr. 21, p. 3883–3900

[Babuška et al 1997b] Babuška, I. ; Ihlenburg, F. ; Strouboulis, T. ; Gangaraj, S.K.: A Posteriori Error Estimation for Finite Element Solutions of Helmholtz' Equation. Part I: The Quality of local Indicators and Estimators. In: *International Journal for Numerical Methods in Engineering* 40 (1997), Nr. 18, p. 3443–3462

[Bao et al 2001] Bao, W. ; Wang, X. ; Bathe, K.J.: On the Inf-Sup Condition of Mixed Finite Element Formulations for Acoustic Fluids. In: *Mathematical Models and Methods in Applied Science* 11 (2001), Nr. 5, p. 883–901

[Bauchau and Craig 2009] Bauchau, O. A. ; Craig, J. I.: *Structural Analysis with Applications to Aerospace Structures*. Springer, 2009

[Beranek 1988] Beranek, Leo L.: *Acoustical Measurements*. American Institute of Physics, 1988

[Bhattacharyya and Premkumar 2003] Bhattacharyya, S. K. ; Premkumar, R.: Transient fluid–structure interaction of elongated bodies by finite-element method using elliptical and spheroidal absorbing boundaries. In: *Journal of Acoustical Society of America* 114 (2003), December, Nr. 6, p. 3053–3064

[Brigham 1997] Brigham, E. O.: *FFT- Anwendungen*. Oldenbourg Verlag, 1997

[Buchschmid 2011] Buchschmid, M.: *ITM-based FSI-models for rooms with absorptive boundaries (preprint)*, Technische Universität München, Ph.D. thesis, 2011

[Buchschmid and Müller 2008] Buchschmid, M. ; Müller, G.: Modeling of Wave Number Dependent Absorptive Characteristics with the Help of the Theory of Porous Media. In: *EURODYN Conference*, 2008

[Buchschmid et al 2009a] Buchschmid, M. ; Pospiech, M. ; Müller, G.: ITM-based FSI-Models for Applications in Room Acoustics. In: *COMPDYN Conference*, 2009

[Buchschmid et al 2009b] Buchschmid, M. ; Pospiech, M. ; Müller, G.: A Semi-analytical Model for Rooms with Absorptive Boundary Conditions. In: *DAGA*, 2009

[Buchschmid et al 2010] Buchschmid, M. ; Pospiech, M. ; Müller, G.: Coupling Impedance Boundary Conditions for Absorptive Structures with Spectral Finite Elements in Room Acoustical Simulations. In: *Journal of Computing and Visualization in Science-Special Issue: Hot Topics in Computational Engineering, Springer 2010* 13 (2010), p. 355–363

[Chan 2006] Chan, Yum-Ji: *Acoustics in small rooms*, Lehrstuhl für Baumechanik, TU München, Master thesis, 2006

[Chopra 2000] Chopra, A. K.: *Dynamics of Structures: Theory and Application to Earthquake Engineering*. PRENTICE-HALL, 2000

[Collins et al 1972] Collins, J. D. ; Hart, G. C. ; Hurty, W. C. ; Kennedy, B.: *Review and Development of Modal Synthesis Techniques*. J. H. Wiggins Company, 1972

[Craig and Bampton 1968] Craig, R. R. ; Bampton, M. C. C.: Coupling of Substructures for Dynamic Analyses. In: *AIAA* 6 (1968), July, Nr. 7, p. 1313–1319

[Craig and Chang 1976] Craig, R. R. ; Chang, C. J.: A Review of Substructure Coupling Methods for Dynamic Analysis. In: *NASA CP-2001* 2 (1976), p. 393–408

[Craig 1981] Craig, R. R. J.: *Structural Dynamis: An Introduction to Computer Methods*. John Wiley & Sons, Inc., New Yourk, NY, 1981

[Craig 1995] Craig, R. R. J.: Substructure Methods in Vibration. In: *ASME Transactions, Special 50th Anniversary Design Issue* 117 (1995), p. 207–213

[Craig 2000] Craig, R. R. J.: A brief tutorial on substructure analysis and testing. In: *Proceedings of the 18th IMAC Conference on Computational Challenges in Structural Dynamics* 1 (2) (2000), p. 899–908

[Cremer and Heckl 2010] Cremer, L. ; Heckl, M.: *Körperschall*. Springer, 2010

[Cremer et al 2005] Cremer, L. ; Heckl, M. ; Petersson, Björn A.: *Structure-Borne Sound*. Springer, 2005

[Cremer and Müller 1976] Cremer, L. ; Müller, H. A.: *Die wissenschaftlichen Grundlagen der Raumakustik*. S. HIrzel Verlag Stuttgart, 1976

[Curnier 1983] Curnier, A.: On Three Modal Synthesis Variants. In: *Journal of Sound and Vibration* 90 (1983), Nr. 4, p. 527–540

[Dey et al 2006] Dey, S. ; Datta, D.K. ; Shirron, J.J. ; Shephard, M.S.: p-Version FEM for structural acoustics with a posteriori error estimation. In: *Computer methods in applied mechanics and engineering* 195 (2006), p. 1946–1957

[Dickens et al 1997] Dickens, J. M. ; Nakagawa, J.M. ; Wittbrodt, M. J.: A Critique of Mode Acceleration and Modal Truncation Augmentation Methods for Modal Response Analysis. In: *Computers and Structures* 62 (1997), Nr. 6, p. 985–998

[Dickens and Pool 1992] Dickens, J. M. ; Pool, K. V.: Modal truncation vectors and periodic time domain analysis applied to a cyclic symmetry structure. In: *Computers and Structures* 45 (1992), Nr. 4, p. 685–696

[DIN 2001–10] DIN: *DIN EN ISO 10543-2: 2001-10 Akustik- Bestimmung des Schallabsorptionsgrades und der Impedanz in Impedanzrohren*. 2001-10

[DIN 2006–08] DIN: *DIN EN ISO 18233: Akustik – Anwendung und Messverfahren in der Bau- und Raumakustik. 2006-08.* 2006-08

[Düster 2001] Düster, A.: *High order finite elements for three-dimensional, thin-walled nonlinear continua*, Technische Universität München, Ph.D. thesis, 2001

[Fahy 2005] Fahy, F.: *Foundations of Engineering Acoustics.* Academic Press, 2005

[Fahy and Gardonio 2007] Fahy, F. ; Gardonio, P.: *Sound and Structural Vibration: Radiation, Transmission and Response.* Academic Press, 2007

[Ford and McCormick 1969] Ford, R.D. ; McCormick, M.A.: Panel Sound Absorbers. In: *Journal of Sound and Vibration* 10 (1969), p. 411–423

[Fuchs 2007] Fuchs, H. V.: *Schallabsorber und Schalldämpfer: Innovative akustische Konzepte und Bauteile mit praktischen Anwendungen in konkreten Beispielen.* Springer, 2007

[Gladwell 1964] Gladwell, G. M. L.: Branch Mode Analysis of Vibrating Systems. In: *Journal of Sound and Vibration* 1 (1964), January, Nr. 1, p. 41–59

[Goldman 1969] Goldman, R. L.: Vibration Analysis by Dynamic Partitioning. In: *AIAA* 7 (1969), Nr. 6, p. 1152–1154

[Graff 1991] Graff, K. F.: *Wave Motion in Elastic Solids.* DOVER PUBLICATIONS, INC., New York, 1991

[Harari 2006] Harari, I.: A survey of finite element methods for time-harmonic acoustics. In: *Computer Methods in Applied Mechanical Engineering* 195 (2006), p. 1594–1607

[Heckl and Müller 1994] Heckl, M. ; Müller, H. A.: *Taschenbuch der Technischen Akustik.* Springer, 1994

[Hughes 2000] Hughes, T. J. R.: *The Finite Element Method: Linear Static and Dynamic Finite Element Analysis.* Dover Publications, 2000

[Hurty 1965] Hurty, W. C.: Dynamic Analysis of Structural Systems Using Component Modes. In: *AIAA* 3 (1965), Nr. 4, p. 678–685

[Hurty 1967] Hurty, W. C.: A Criterion for Selecting Realistic Natural Modes of a Structure / National Aeronautics and Space Administration. 1967. – Research Report

[Jezequel 1985] Jezequel, L.: A hybrid method of modal synthesis using vibration tests. In: *Journal of Sound and Vibration* 100 (1985), May, Nr. 2, p. 155–308

[Kattan 2007] Kattan, P.: *MATLAB Guide to Finite Elements*. Springer, 2007

[Keane and Price 1997] Keane, A.J. ; Price, W.G.: *Statistical Energy Analysis: An Overview with Applications in Structural Dynamics*. Cambridge Universtiy Press, Cambridge, UK, 1997

[Kiencke and Eger 2005] Kiencke, U. ; Eger, R.: *Messtechnik - Systemtheorie für Elektrotechniker*. Springer, 2005

[Kohlrausch 1955] Kohlrausch, F.: *Praktische Physik 1*. B. G. Teubner Verlagsgesellschaft, 1955

[Kwon and Bang 2000] Kwon, Y. W. ; Bang, H.: *The Finite Element Method Using MATLAB*. CRC Press, 2000

[Langley 2008] Langley, R.S.: Recent advances and remaining challenges in the statistical energy analysis. In: *EURODYN*, 2008

[Lyon and DeJong 1995] Lyon, R.H. ; DeJong, R.G.: *Theory and Application of Statistical Energy Analysis*. 2 edition. Butterworth-Heinemann, Boston, 1995

[Müller 2009] Müller, G.: *Continuum Mechanics and Tensor Analysis - Lecture notes*. Lehrstuhl für Baumechanik, Technische Universität München, 2009

[Müller 2010] Müller, G.: *Selected Topics of Technical Acoustics - Lecture notes*. Lehrstuhl für Baumechanik, Technische Universität München, 2010

[Müller et al 2006] Müller, G. ; Buchschmid, M. ; Guggenberger, J.: Modellbildung zur Körperschallausbreitung in Tragstrukturen unter Berücksichtigung des Einflusses von Innenausbauten. In: *VDI-Berichte* 1941 (2006), p. 59–70

[Müller and Möser 2004] Müller, G. ; Möser, M.: *Taschenbuch der Technischen Akustik*. Springer, 2004

[Müller and Massarani 2001] Müller, S. ; Massarani, P.: Transfer function measurement with sweeps. In: *J. Audio Eng. Soc.* 49 (2001), p. 443–471

[Möser 2007] Möser, M.: *Technische Akustik*. Springer, 2007

[Möser 2010] Möser, M.: *Messtechnik der Akustik*. Springer, 2010

[Natke 1983] Natke, H.G.: *Einführung in Theorie und Praxis der Zeitreihen- und Modalanalyse*. Vieweg, 1983

[Paolini 2010] Paolini, A.: *Analytische Modellierung und messtechnische Untersuchung der Absorptionseigenschaften von porösen Schäumen, TU München*, Bachelor Thesis, Lehrstuhl für Baumechanik, TU München, 2010

[Pospiech 2010] Pospiech, M.: *Numerical Simulations in Room Acoustics using direct Coupling Techniques and Finite Elements*, Technische Universität München, Ph.D. thesis, 2010

[Pospiech et al 2009] Pospiech, M. ; Buchschmid, M. ; Müller, G.: Spectral Approaches for Room acoustical Simulation. In: *Proceedings ICSV16 Kraków*, 2009

[Pozrikidis 2005] Pozrikidis, C.: *Introduction to Finite and Spectral Element Method using MATLAB*. Chapman & Hall /CRC, 2005

[Qu 2004] Qu, Zu-Quing: *Model Order Reduction Techniques: with application in finite elemente analysis*. Springer-verlag Gmbh, 2004

[Rabold 2010] Rabold, A.: *Anwendung der Finite Element Methode auf die Trittschallberechnung*, Technische Universität München, Ph.D. thesis, 2010

[Rank et al 2003] Rank, E. ; Bröker, H. ; Düster, A. ; Krause, R. ; Rücker, M.: The p-version of the Finite. Element Method for Structural Problems. In: *Error-controlled Adaptive Finite Elements in Solid Mechanics* John Wiley & Sons (2003), p. 263–370

[Rao 1982] Rao, S. S.: *Finite Element Method in Engineering*. Pergamon Press, 1982

[Reyonso 1985] Reyonso, A. G.: *Structural Dynamics Model of a Cartesian Robot*, Massachusetts Institute of Technology, Ph.D. thesis, 1985

[Schilders et al 2008] Schilders, W.H. ; Vorst, H.A. van der ; Rommes, J.: *Model Order Reduction: Theory, Research Aspects and Applications (Mathematics in Industry).* Springer, 2008

[Sellgren 2003] Sellgren, U.: Component Mode Synthesis – A method for efficient dynamic simulation of complex technical systems / Department of Machine Design, KTH Sweden, Stockholm. 2003. – Research Report

[Shorter and Langley 2005] Shorter, P. ; Langley, R.: Vibro-Acoustic analysis of complex systems. In: *Journal of Sound and Vibration* 288 (2005), Nr. 3, p. 669–699

[Shyu et al 1997] Shyu, W. H. ; Ma, Z. D. ; Hulbert, G. M.: A new component mode synthesis method: Quasi-static mode compesation. In: *Finite Elements in Analysis and Design* 24 (1997), p. 271–281

[Sremcevic et al 2009a] Sremcevic, J. ; Buchschmid, M. ; Müller, G.: Modal based model reduction techniques for FSI-problems in room acoustics. In: *3rd GACM Colloquium on Computational Mechanics for Young Scientists in Hannover*, 2009

[Sremcevic et al 2009b] Sremcevic, J. ; Buchschmid, M. ; Pospiech, M. ; Müller, G.: Simulation of acoustic cavities considering realistic boundary conditions. In: *iNDiS 2009 Novi Sad, Proceedings*, 2009

[Suarez and Singh 1992] Suarez, L. E. ; Singh, M. P.: Improved Fixed Interface Method for Modal Synthesis. In: *AIAA* 30 (1992), Nr. 12, p. 2952–2958

[Thompson 2006] Thompson, L. L.: A review of finite element methods for time-harmonic acoustics. In: *Journal of Acoustical Society of America* 119 (2006), Nr. 3, p. 1315–1330

[Timoshenko 1953] Timoshenko, S. P.: *History of strength of materials.* McGraw Hill, 1953

[Tran 2001] Tran, D.-M.: Component mode synthesis methods using interface modes. Application to structures with cyclic symmetry. In: *Computers and Structures* 79 (2001), p. 209–222

[Wandinger 1994] Wandinger, J.: Analysis of Small Vibrations of Coupled FLuid-Structure Systems. In: *Zeitschrift für Angewandte Mathematik und Mechanik* 74 (1994), p. 37–42

[Wang 2008] Wang, X.: *Fundamentals of Fluid–Solid Interactions: Analytical and Computational Approaches.* Elsevier, 2008

[Wang and Bathe 1997] Wang, X. ; Bathe, K.-J.: Displacement / Pressure Based Mixed Finite Element Formulations for Acoustic Fluid-Structure Interaction Problems. In: *International Journal for Numerical Methods in Engineering* 40 (1997), p. 2001–2017

[Wüchner 2007] Wüchner, R.: *Finite Element Methods I.* Lecture Notes, Lehrstuhl für Bauinformatik, Technische Universität München, 2007

[Yin et al 1991] Yin, B. ; Wang, W. ; Jin, Y.: The Application of Component Mode Synthesis for the Dynamic Analysis of Complex Structures Using ADINA. In: *Computers and Structures* 64 (1991), p. 931–938

[Young 2000] Young, J. T.: *Primer on the Craig-Bampton Method: An Introduction to the Boundary Node Functions, Base Shake Analyses, Load Transformation Matrices, Modal Synthesis and Much More*, October 2000

[Zienkiewicz and Taylor 2006] Zienkiewicz, O. C. ; Taylor, R. L.: *The Finite Element Method for Solids and Structural Mechanics.* Elsevier, 2006

[Zienkiewicz et al 2006a] Zienkiewicz, O. C. ; Taylor, R. L. ; Zhu, J. Z.: *The Finite Element Method its Basis and Fundamentals.* Elsevier, 2006

[Zienkiewicz et al 2006b] Zienkiewicz, O. C. ; Taylor, R.l. ; Nithiarasu, P.: *The finite element method for fluid dynamics.* Elsevier, 2006